*Santo Maria Roccuzzo*

# SUPERSOLIDITY IN A DIPOLAR BOSE GAS

*PhD Thesis,*
*University of Trento*
*November 2021*

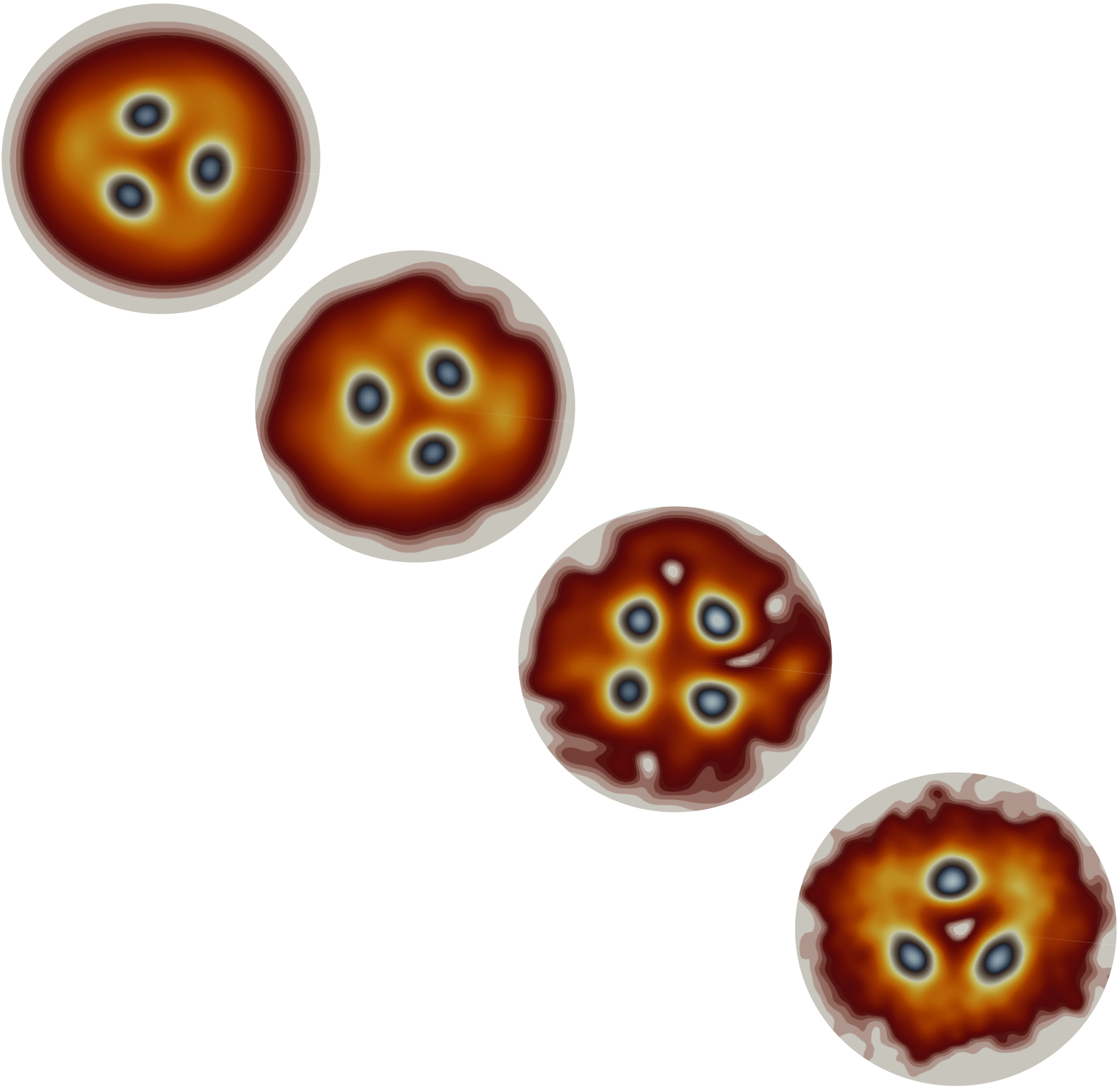


*Department of Physics,*
*University of Trento,*
*Italy*

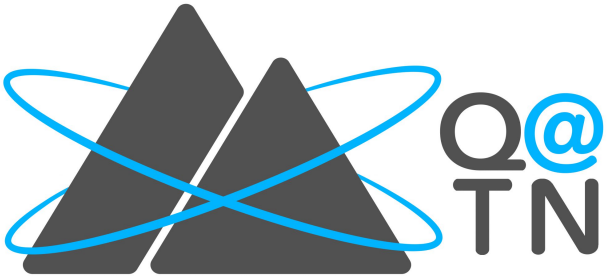


*Quantum@Trento joint laboratory*

# Supersolidity in a dipolar Bose gas

Santo Maria Roccuzzo

A dissertation submitted to the
Department of Physics
University of Trento

In fullment of the requirements for the Degree of

Doctor of Philosophy in Physics

Under the supervision of
Dr. Alessio Recati
and
Prof. Sandro Stringari

---

Dottorato di Ricerca XXXIV Ciclo
Novembre 2021

*A Carolina*
*che rende tutto possibile*

# Contents

# Abstract

Ultracold quantum gases have nowadays become an invaluable tool in the study of quantum many-body problems. The high level of experimental control available on these systems and well established theoretical tools make ultracold quantum gases ideal platforms for quantum simulations of other systems currently unaccessible in experiments as well as for studies of fundamental properties of matter in the quantum degenerate regime.
A key manifestation of quantum degeneracy in samples of ultracold bosonic neutral atoms is the formation of a Bose-Einstein condensate (BEC), a peculiar state of matter in which a macroscopic number of atoms occupy the same single-particle state. Bose-Einstein condensation occurs in extremely rarified gases of bosonic atoms at temperatures around the nanoKelvin. At such temperatures, the equilibrium state of all known elements (except for helium) in ordinary conditions of density and pressure would be the solid phase. To obtain a BEC it is thus necessary to consider very dilute samples with a density of the order of $10^{14} - 10^{15}$ atoms/cm$^3$, around eight orders of magnitude smaller then the density of ordinary matter. At such densities, the three-body recombination mechanisms responsible for the formation of molecules, that cluster to form solids, are suppressed. However, despite the extreme diluteness, two-body interatomic interactions play a prominent role in determining the physical properties of these systems.
In the temperature and density regimes typical of BECs, the theoretical description of the system can be greatly simplified by noticing that the low-energy scattering properties of the real, generally involved, interatomic potential, can be perfectly reproduced by a simpler pseudo-potential, usually of the form of an isotropic contact repulsion, and described by a single parameter, the s-wave scattering length [1]. Such parameter can even be tuned, in experiments, via the so-called *Feschbach resonances*. Despite its simplicity, this zero-range, isotropic interaction is responsible for an enormous variety of physical effects characterizing atomic BECs [2]. This fact stimulated, over the last twenty years, the research of different possible types of interactions, that can eventually lead to the formation of new and exotic phases of matter.
In this quest, the dipole-dipole interaction attracted great attention for different

reasons. First, there are several experimental techniques to efficiently trap and cool atoms (or molecules) possessing a strong dipole moment. This led, for example, to the experimental realization of BECs of $Cr$ [3], $Dy$ [4] and $Er$ [5], which have, in the hyperfine state trapped for condensation, a magnetic dipole moment around ten times larger then the one typical of the particles in a BEC of alkali atoms. Moreover, being the dipole-dipole interaction anisotropic and long-ranged, its low-energy scattering properties cannot be described by a simple short-range isotropic potential. As a consequence, dipolar BECs show unique observable properties.

The partially attractive nature of the dipole-dipole interaction can make a dipolar BEC unstable against collapse, similarly to the case of an ordinary (non-dipolar) BEC with negative scattering length. This happens, in particular, if a sample of magnetic atoms, polarized along a certain direction by some magnetic field, is not confined enough along such direction (for example via a harmonic potential). However, differently from ordinary BECs, where the collapse of the system is followed by a rapid loss of atoms and the destruction of the condensed phase, in the dipolar case such instability is followed by the formation of self-bound, (relatively) high density liquid-like droplets [6]. If the geometry of the confinement potential allows it, the droplets spontaneously arrange into a regular, periodic configuration, in a sort of "droplet crystal". Moreover, by fine-tuning the interaction parameters, it is possible to achieve global phase coherence between these droplets. The spatially modulated, phase coherent system that forms in these conditions is known as *supersolid*, and is a very peculiar state showing simultaneously properties of both crystals and superfluids.

Ordinary mean-field theory, so successful in describing the vast phenomenology of ordinary BECs, fails in predicting the existence of the exotic phases of supersolids, quantum droplets and droplet crystals in a dipolar quantum gas. The state of the art description of dipolar BECs in such conditions is instead based on quantum fluctuations, taking into account the local density approximation of the first-order beyond-mean-field correction of the ground state energy of the system [7]. This correction, known as the *Lee-Huang-Yang* correction, results in a repulsive energy term that balances the mean-field attraction at the relatively high densities that characterize the collapsing state.

Using state-of-the-art simulation techniques, in this thesis I study the behavior of a dipolar Bose gas confined in a variety of trapping configurations, considering ground-state properties, elementary excitations, and the dynamical behavior under several kinds of external perturbations, focusing in particular on the supersolid phase.

In Chapter 1, I review the basic properties of supersolids, following a historical perspective, describing the first proposals for supersolidity in solid helium, and

discussing the current implementations in cold atoms.
In Chapter 2, I review the basic theory of dipolar Bose gases. I also introduce the fundamental methods used in the thesis, and in particular the linear response theory, with a particular emphasis on the sum-rule formalism, and the numerical techniques used to solve the modelling equations.
In Chapter 3, I study the behavior of the dipolar Bose gas in an ideal situation, namely when the gas is confined in a harmonic trap along the polarization direction of the dipoles as well as one of the orthogonal directions. Along the unconfined direction, instead, periodic boundary conditions are set, in order to simulate the geometry of a ring. I study in particular the evolution of the ground state of the system from a superfluid, homogeneous along the ring, to the supersolid regime, and eventually to an array of independent droplets. These phase transitions are realized by tuning a single interaction parameter, namely the s-wave scattering length. The superfluid phase is here characterized by the occurrence of a roton minimum in the energy-momentum dispersion relation. The energy of the roton, called roton gap, decreases when the s-wave scattering length of the system is decreased and the dipole-dipole interaction becomes the dominant interaction mechanism. When the roton minimum touches the zero-energy axis, the superfluid system is not stable anymore against mechanical collapse. The system thus tend to form denser clusters of atoms, regularly arranged in an equally-spaced array of droplets, whose relative distance is fixed by the inverse of the roton momentum. Such droplets are stabilized by quantum fluctuations, which enters in the energy functional of the system via the Lee-Huang-Yang correction. I demonstrate that when the droplets show a finite overlap, the ground state of the system manifests signatures of supersolid behavior, and in particular

- The occurrence of two Goldstone modes, associated with the two symmetries spontaneously broken in the supersolid, namely the symmetry for continuous translations, which is broken in favor of a discrete one, and the U(1) symmetry associated with Bose-Einstein condensation.

- The appearance of non-classical rotational inertia, due to the partially superfluid character of the system.

In Chapter 4, I explore possible manifestations of supersolid behavior in a fully trapped configuration, namely when the system is confined in an elongated (cigar-shaped) harmonic trap, with the long axis orthogonal to the polarization direction. Part of the results obtained in the three-dimensional harmonic trap have been compared with the first available experiments. The two key signatures of supersolid behavior, namely the occurrence of two Goldstone modes and non-classical rotational inertia, can be detected, in this case, by studying the low-energy collective oscillations of the system. A behavior equivalent to the one of

the two Goldstone modes predicted in the ring trap, can be found in the axial compressional oscillations of the harmonically trapped system, which bifurcate at the superfluid-supersolid phase transition. When the system is driven through the supersolid-independent droplet transition, the lower-energy mode, associated with phase coherence, tends to disappear, while the higher energy mode, associated with lattice excitations, tends to assume a constant frequency. This behavior is specular to the one of the two Goldstone modes in the ring geometry, and is a signal of the presence of supersolidity in the trapped system. Important experimental confirmations of these predictions have already been found. Instead, a key manifestation of non-classical inertia in a trapped dipolar supersolid can be found by studying the rotational oscillation mode known as "scissors" mode, whose frequency is directly related to the value of the moment of inertia (similar to the frequency of oscillation of a torsional pendulum for a classical system). Studying the behavior of the frequency of the scissors mode across the superfluid-supersolid-independent droplets phase transitions, I demonstrate the actual occurrence of non-classical inertia in a harmonically trapped dipolar supersolid.

In Chapter 5, I study another key manifestation of superfluidity in a dipolar supersolid, namely the occurrence of quantized vortices, which I study in the case of a dipolar Bose gas trapped in a harmonic trap isotropic in the plane orthogonal to the polarization direction. I study in particular the size of the vortex core as function of the interaction parameters, showing that, in the superfluid phase, it increases as the superfluid-supersolid phase transition is approached. Then, in the supersolid phase, I show that quantized vortices settle in the interstices between the density peaks, and their size and even their shape are fixed respectively by the droplet distance and the shape of the lattice cell. I also study the critical frequency for the vortex nucleation under a rotating quadrupolar deformation of the trap, showing that it is related to the frequency of the lower-energy quadrupole mode, associated with the partial superfluid character of the system. I also study the competition between the vortex and supersolid lattices, showing that the position of the vortices is always pinned at the density minima between the density peaks of the supersolid lattice. Finally, I study the observability of the phenomena discussed in an expanding system, in which the in-plane confinement is switched off.

Finally, in Chapter 6, I study the behavior of a dipolar Bose gas confined by hard walls. In particular, I investigate the novel ground-state density distributions, with special focus on the effects of supersolidity. Differently from the case of harmonic trapping, in this case, the ground state density shows a strong depletion in the bulk region and an accumulation of atoms near the walls, well separated from the bulk, as a consequence of the competition between the attractive and the repulsive nature of the dipolar force. In a quasi two-dimensional geometry characterized by cylindrical box trapping, the consequence is that the superfluid

accumulating along the walls forms spontaneously a ring shape, showing eventually also supersolidity. For sufficiently large values of the atom density, also the bulk region can exhibit supersolidity, the resulting geometry reflecting the symmetry of the confining potential.

# Chapter 1

# What is a supersolid?

In this Chapter, I present the basic definition and fundamental properties of the supersolid phase. Following a historical perspective, I discuss the first proposals for supersolidity in solid helium, and then discuss the current implementations of supersolidity in ultracold atomic systems.

## 1.1 Long range order

A *supersolid* can be defined as a quantum state of matter showing both the *spatial periodicity* that characterizes crystalline solids, and the *phase coherence* typical of Bose-Einstein condensed systems. Supersolidity can be found in systems that spontaneously break both a continuos translational symmetry in favour of a discrete one, developing spatial periodicity, and the gauge symmetry that results in the phase coherence of a Bose-Einstein condensate. Given the link between Bose-Einstein condensation and superfluidity, a supersolid can, paradoxically, show properties of both solids and superfluids.
More rigorously, a supersolid is a system that shows both diagonal and off-diagonal long range order [8]. In particular, defining the field operators $\hat{\Psi}^\dagger(\mathbf{r})$ and $\hat{\Psi}(\mathbf{r})$ that respectively create and annihilate a particle at position $\mathbf{r}$, the diagonal one-body density matrix of a supersolid

$$n(\mathbf{r}) = \langle \hat{\Psi}^\dagger(\mathbf{r}) \hat{\Psi}(\mathbf{r}) \rangle \tag{1.1}$$

shows *discrete* spatial periodicity

$$n(\mathbf{r}) = n(\mathbf{r} + \mathbf{T}) \tag{1.2}$$

where $\mathbf{T}$ stands for a lattice vector of the crystalline structure, while the off-diagonal density matrix

$$n(\mathbf{r}, \mathbf{r}') = \langle \hat{\Psi}^\dagger(\mathbf{r}) \hat{\Psi}(\mathbf{r}') \rangle \tag{1.3}$$

approaches a finite value at infinite distances

$$n(\mathbf{r}, \mathbf{r}') \to n_0 \text{ when } |\mathbf{r} - \mathbf{r}'| \to \infty \tag{1.4}$$

While the diagonal long-range order implied by equation 1.2, characterized by the spatial periodicity of the one-body density matrix, is a typical feature of crystalline solids, the off-diagonal long-range order implied by equation 1.4 is a defining feature of Bose-Einstein condensed systems [2].

## 1.2 Supersolidity in "ordinary" quantum crystals

The possible existence of a supersolid phase of matter has been debated for decades. A seminal paper by Penrose and Onsager [9] ruled out the possibility for a perfect crystal to form a Bose-Einstein condensate, since the localization of atoms at the lattice sites of a crystal is incompatible with the off-diagonal long range order necessary for Bose-Einstein condensation.
Soon after, Andreev and Lifshitz [10] proposed that supersolidity may manifest via Bose-Einstein condensation of *defects* (such as vacancies, or impurities) in a quantum crystal. More precisely, they developed a theory according to which, at zero temperature, quantum tunneling decreases the localization of defects, which thus can travel through the crystal; their state can then be labelled via momentum $\mathbf{k}$, and their energy-momentum dispersion relation produces an additional "defecton" branch in the excitation spectrum of the solid. If the defects have bosonic nature (for example, a vacancy in a crystal of bosonic atoms), the defectons can condense into the state of zero momentum, forming a Bose-Einstein condensate embedded in the crystal structure of the system. In the words of the authors, in these conditions, the "superfluid crystal" (i.e., the supersolid) can flow without friction through a capillary under the action of an external force field.
In order to describe this system, Andreev and Lifshitz, in the spirit of Landau's theory of superfluidity, developed a two-component model, treating separately the "normal" (i.e., the crystal) and the "superfluid" part of the supersolid. A fundamental assumption of the model is that one can write the energy and momentum densities of this system as [11]

$$\begin{aligned} \mathcal{E} &= \frac{1}{2}\rho_S \mathbf{v}_S^2 + \frac{1}{2}\rho_N \dot{\mathbf{u}}^2 + \mathcal{E}_0(\rho, s, \epsilon) \\ \mathbf{j} &= \rho_S \mathbf{v}_S + \rho_N \dot{\mathbf{u}} \end{aligned} \tag{1.5}$$

where $\rho_N$ and $\rho_S$ are, respectively, the normal and superfluid densities of the system, whose sum gives the total density $\rho = \rho_N + \rho_S$, $\mathbf{v}_S$ is the superfluid velocity,

$\mathbf{u}$ is the displacement field describing the elastic deformations of the lattice, and $\mathcal{E}_0(\rho, s, \epsilon)$ is the internal energy of the system, assumed to be a function of the total density $\rho$, the entropy density $s$, and the elastic stress tensor $\epsilon_{ij} = (\partial_i u_j + \partial_j u_i)/2$. Under very general principles, assuming mass, momentum, energy and entropy conservation, and the presence of some superfluid motion in the system, Andreev and Lifshitz derived a set of macroscopic equations for the supersolid, from which they derived a description of the long wavelength excitations of the system in terms of *four* acoustic mode. The dispersion relations of these modes can be written as

$$\begin{aligned} \omega_i^N(\mathbf{k}) &= \omega_i^0(\mathbf{k}) \left(1 + \frac{\rho_S}{2\rho}\right), \text{ i=1,2,3} \\ \omega_4^S(\mathbf{k}) &= \sqrt{\rho^S \sum_{lm} \Lambda_{lm} k_l k_m} \end{aligned} \tag{1.6}$$

Here, the superscripts $N$ and $S$ stand, respectively, for the normal (i.e., the crystal) and the superfluid modes of the system; in the first equation of 1.6, $\omega_i^0$, for $i = 1, 2, 3$, are the dispersion relations of the three acoustic phonons of the crystal in absence of a superfluid component, and $\Lambda_{lm}$ is proportional to the elastic stress tensor $\epsilon_{lm}$. Results 1.6 show in particular that the sound modes of the crystal and the superfluid components are always coupled through the superfluid density $\rho^S$ and the elastic stress tensor, and that the speed of sound associated with the superfluid mode decreases with the square root of $\rho_S$.
The first attempts to prove supersolidity in samples of solid helium were based on the search of a super-flow under a pressure gradient [12, 13], but failed to detect any superfluid effect.
Another milestone in the theory of supersolidity is due to Leggett [14], who proposed that a key manifestation of the supersolid phase transition in a quantum crystal would be a sudden drop of the moment of inertia from its "classical" value (i.e., the value determined by the mass distribution). Such non-classical rotational inertia (NCRI) can in principle be measured via the frequency of the oscillations of a torsional pendulum, after properly taking into account geometrical factors. More in detail, consider a general many body system of $N$ identical particles of mass $m$ confined in an annular container in the $z = 0$ plane of a certain coordinate system, and let the many-body Hamiltonian be

$$\hat{H} = \sum_{i=1}^{N} \left( -\frac{\hbar^2}{2m} \nabla_i^2 + U(\mathbf{r}_i) \right) + \frac{1}{2} \sum_{i,j=1}^{N} V(|\mathbf{r}_i - \mathbf{r}_j|) \tag{1.7}$$

where $U(\mathbf{r}_i)$ is an external potential describing the effects of the container. If the annular container is at rest, the many-body ground-state wave function of the system is required to satisfy the "single-valuedness boundary condition", which

implies that, whenever a particle is brought once around the annulus, leaving the rest unchanged, the ground-state wave function does not change. Calling $\Psi(\theta_i, \eta_i)$, for $i = 1, \ldots, N$, the ground state wave function, depending on an angular coordinate $\theta_i$ along the ring, and a general transverse coordinate $\eta_i$, the single-valuedness boundary condition reads

$$\Psi(\eta_1, \theta_1; \eta_2, \theta_2; \ldots; \eta_i, \theta_i; \ldots; \eta_N, \theta_N) = \Psi(\eta_1, \theta_1; \eta_2, \theta_2; \ldots; \eta_i, \theta_i + 2\pi; \ldots; \eta_N, \theta_N) \tag{1.8}$$

Now, let us suppose that the ring lies in the $z = 0$ plane and is put into slow rotation with angular velocity $\omega$ around the z-axis. Once we lead a particle in a $2\pi$ circle around the z-axis, the wave function now acquires a phase $\Delta\phi$, so that the single-valuedness boundary condition shall now be written as

$$\begin{aligned} &\Psi_{\Delta\phi}(\eta_1, \theta_1; \eta_2, \theta_2; \ldots; \eta_i, \theta_i; \ldots; \eta_N, \theta_N) = \\ &\mathrm{e}^{i\Delta\phi}\Psi(\eta_1, \theta_1; \eta_2, \theta_2; \ldots; \eta_i, \theta_i + 2\pi; \ldots; \eta_N, \theta_N) \end{aligned} \tag{1.9}$$

We now define the *superfluid fraction* of the system at a certain temperature $T$ as [15]

$$f_s(T) = 1 - \lim_{\omega \to 0} \frac{\langle \hat{L}_z \rangle}{\omega} \tag{1.10}$$

where $\hat{L}_z$ is the projection of the angular momentum along the z-axis, and the expectation value is calculated in conditions of thermodynamic equilibrium, with the walls of the container rotating at angular velocity $\omega$. Intuitively, we are defining the superfluid fraction of the system as the fraction of particles which is not dragged by any (slow) rotation of the container. Calling now $\Psi_0$ the exact ground-state wave function of the system, and considering a variational ansatz of the form

$$\Psi_{trial} = \mathrm{e}^{i\sum_i \phi(\theta_i)}\Psi_0 \tag{1.11}$$

where $\phi(\theta)$ satisfies the condition $\phi(\theta + 2\pi) = \phi(\theta) + \Delta\phi$, minimizing the expectation value of the Hamiltonian 1.7 with respect to $\phi(\theta)$, Leggett found an *upper bound* for the superfluid fraction of the system at $T = 0$ which reads

$$f_s(T = 0) \leq \left\{ \int \frac{d\theta}{\rho(\theta)/\rho} \right\}^{-1} \tag{1.12}$$

where $\rho(\theta)$ is the value of the density averaged over the transverse coordinate, and $\rho$ is the density averaged over $\theta$. Finally, Leggett shows that a necessary and sufficient condition for this expression to become an equality, is that the Hamiltonian is invariant under time-reversal and continuous translation, and the ground-state of the system does not spontaneously break any of these two symmetries. This implies that, at $T = 0$, any *homogeneous* system confined in an annulus, and described by

a Hamiltonian satisfying both time-reversal and translational symmetries, is fully superfluid, since expression 1.12 becomes exactly 1. But this also implies that, if a system spontaneously breaks translational invariance along the annulus, then the upper bound on this superfluid fraction becomes rigorously smaller then 1.
As said, a consequence of a superfluid fraction smaller then 1 is that the moment of inertia, measured for example using a torsional pendulum, results to be smaller then the "classical" value, that is the value determined by the mass distribution in the system. Following this idea, in the early 2000, it seemed that supersolid evidences were found through measurements of NCRI [16, 17, 18, 19, 20], in a famous series of experiments by Kim and Chan. Unfortunately, the results of these works were proved to be non-conclusive [21], as the drop in the moment of inertia observed in the first experiments could well be explained not invoking a finite superfluid fraction, but rather by a change in the elastic properties of the material due to the lower temperature. Up to now, no final evidence of supersolidity exists in samples of solid helium, nor in any other "classical" solid.

## 1.3 Supersolidity in ultracold atomic gases

A new scenario came up more recently, in particular with the works of Pomeau and Rica [22] and of Josserand, Pomeau and Rica [23, 11], where the authors show that systems described by a Gross-Pitaevskii equation with *non-local* interactions can undergo a supersolid phase transition. More in detail, the authors consider systems described by the following equation for the condensate wave-function

$$i\hbar\frac{\partial\psi(\mathbf{r},t)}{\partial t} = \left[-\frac{\hbar^2\nabla^2}{2m} + V_{ext}(\mathbf{r}) + \int d\mathbf{r}' U(\mathbf{r}-\mathbf{r}')|\psi(\mathbf{r}',t)|^2\right]\psi(\mathbf{r},t) \qquad (1.13)$$

where $V_{ext}$ is some external potential, and $U(\mathbf{r}-\mathbf{r}')$ is the interaction potential between two particles at position $\mathbf{r}$ and $\mathbf{r}'$. For definiteness and for carrying out numerical simulations, the authors considered a model of *soft-core bosons*, i.e. an interaction potential of the form $U(r) = U_0$ for $r < a$ and $U(r) = 0$ otherwise, where $a$ is a certain length. As shown in [22], the long-wavelength fluctuations on top of a uniform ground-state are characterized by a linear spectrum at small momenta, and a *local minimum*, called "roton", at a certain finite momentum $k_0$. Moreover, as the density of the system is increased, the roton energy decreases, until the roton minimum touches the zero-energy axis. In these conditions, both in 2 and 3 spatial dimensions, the ground state of the system is not characterized by a uniform density profile, but rather by a *periodic* structure (hexagonal in 2D, and a bcc lattice in 3D), characterized by partially overlapping density peaks, each containing many atoms, sitting at the lattice sites. This system shows properties very similar to those predicted for a supersolid by Andreev and Lifshitz, as well

as by Leggett, for example the presence of an additional sound mode, related to the superfluid part of the system, beside the phonon modes of the lattice, but also non-classical rotational inertia (see also later works by the same authors, such as [24]), and even quantized vortices.
The supersolid state described by Pomeau and Rica is, in many aspects, different from the one originally predicted by Andreev and Lifshitz. In fact, in this Gross-Pitaevskii model with non-local interactions, the supersolid behavior arises in a defect-free lattice: each lattice site is occupied by several atoms, resulting in a sort of "droplet crystal", where each droplet shows a density profile that partially overlaps with the one of neighbouring droplets. Nonetheless, it manifests all the properties expected for a "classical" supersolid, namely

- non-classical rotational inertia;
- four sound modes, instead of three, in a 3-dimensional model;
- quantized vortices.

Interestingly, the authors finally found that this supersolid cannot flow without friction around an obstacle, as this motion produces a strong plastic deformation of the lattice, but also the proliferation of vortices and other excitations that finally lead to dissipation, even at very small velocities [22].
These findings stimulated the research of the supersolid phase of matter in ultracold quantum gases with exotic interactions, such as dipole-blockaded [25] or "soft-core" Rydberg atoms [26]. The properties of the supersolid phase has been thoroughly studied both using the Gross-Pitaevskii model [27, 28] and Quantum Monte Carlo simulations [25], confirming and extending the predictions of [22]. Unfortunately, technical difficulties in obtaining a Bose-Einstein condensate of Rydberg atoms have prevented, up to now, the experimental implementation of this possibility.
Supersolid properties have finally been observed in cold atomic systems with spin-orbit coupling [29], light-mediated interactions in optical cavities [30], and magnetic dipole-dipole interactions [31, 32, 33]. The last possibility is particularly appealing since, differently from the previous two, here the spontaneous breaking of the translational symmetry is not imposed by some external potential, but determined entirely by the interatomic interactions, as I will show in the rest of this thesis.

# Chapter 2

# Methods

In this Chapter, I review the models and methods used to derive the results presented in this thesis.
After an introduction on the basic properties of the dipole-dipole interaction, I review the mean-field description of dipolar Bose gases, explaining how it fails when compared with recent experiments. I thus introduce the state-of-the-art description of dipolar Bose-Einstein condensates, based on the first-order beyond-mean-field correction to the ground-state energy of the system, which for a non-homogeneous system is introduced in local density approximation.
Then, I review the basics of linear response theory, as used in this thesis, focusing in particular on the sum-rule approach, very useful for the study of the low-energy oscillations of general many-body systems.
Finally, I present the numerical methods used to obtain most of the results presented in the thesis.

## 2.1 Bose-Einstein condensates of magnetic atoms

### 2.1.1 Dipole-Dipole interaction

The general form of the interaction potential between two identical electric or magnetic dipoles at a relative position $\mathbf{r}$ is given by [34]

$$V(\mathbf{r}) = \frac{C_{dd}}{4\pi} \frac{(\mathbf{e_1} \cdot \mathbf{e_2})r^2 - 3(\mathbf{e_1} \cdot \mathbf{r})(\mathbf{e_2} \cdot \mathbf{r})}{r^5} \tag{2.1}$$

where $C_{dd} = \mu_0 \mu^2$ for two magnetic dipoles with magnetic moment $\mu$, $\mu_0$ being the permeability of the vacuum, while $C_{dd} = d^2/\varepsilon_0$ for two identical electric dipoles with electric dipole moment $d$, $\varepsilon_0$ being the vacuum permittivity. In all the cases studied in this thesis (as well as in most current theoretical and experimental works

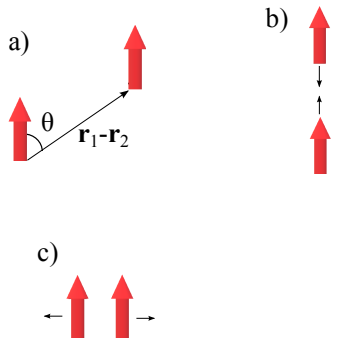


Figure 2.1: *Anisotropy of the dipole-dipole interaction.* According to 2.2, the dipole-dipole interaction potential between two identical, aligned dipoles depends on their distance $r$ and on the angle $\theta$ between the relative position vector $\mathbf{r}$ and the polarization direction z (panel a); the two aligned dipoles attract each other if in a head-to-tail configuration (panel b), and repel each other if sitting side-by-side (panel c).

on this subject), the dipoles are polarized (i.e., aligned along the same axis) by some external magnetic field; choosing the polarization direction as the z-axis of our coordinate system, the dipole-dipole interaction potential 2.1 simplifies in

$$V_{dd}(\mathbf{r}) = \frac{C_{dd}}{4\pi}\frac{1-3\cos^2\theta}{r^3} \tag{2.2}$$

where $\theta$ is the angle between the vector $\mathbf{r}$ joining the two dipoles and the polarization direction (see figure 2.1). We can see that the interaction potential is long-ranged, decaying at large distances as $r^{-3}$ (differently from the typical van der Waals interaction potential which at large distances decays as $r^{-6}$), and anisotropic, depending on the angle $\theta$ between the polarization direction and the vector $\mathbf{r}$ joining the dipoles. In particular, for increasing $\theta$ and fixed $r$, the interaction potential varies from a minimum of $-\frac{C_{dd}}{2\pi r^3}$ at $\theta = 0$ to a maximum of $\frac{C_{dd}}{4\pi r^3}$ at $\theta = \pi/2$, and it is null at $\theta_0 = \arccos(1/\sqrt{3}) \simeq 54.7°$. Taking into account the periodicity of $\cos^2(\theta)$, this implies that, for $|\theta| < \theta_0$ or $\theta_0 + \pi/2 < \theta < \theta_0 + \pi$ the interaction is attractive, otherwise it is repulsive. Hence, two dipoles in free space tend to "pile-up" in a head-to-tail configuration in order to reach the lowest energy configuration, with fundamental consequences on the stability of a dipolar BEC. A very useful parameter that allows to quantify the strength of the dipolar interaction is the *dipolar length* $a_{dd}$, defined as

$$a_{dd} = \frac{C_{dd}m}{12\pi\hbar^2} \tag{2.3}$$

This quantity allows to compare the typical strength of electric and magnetic dipole moments, and will be useful also to compare the relative strength of the dipole and the contact interaction energies. In table 2.1 (taken from [35]) we can see typical values of $a_{dd}$ for different atomic (magnetic) and molecular (electric) species. We can clearly see that the dipolar length for electric dipoles is much larger than that of magnetic dipoles, making, in principle, the former the platform of choice for studying dipolar effects. However, at the time of writing, because of technical difficulties in experiments, the quantum degenerate regime with polar molecules has been reached only with fermionic molecules [36], while Bose-Einstein condensation of magnetic atoms is nowadays a consolidated practice in many laboratories. For this reason, the rest of this thesis will be dedicated to the study of BECs of magnetic atoms. We will see that, although substantially weaker then the electric case, the magnetic dipole-dipole interaction affects crucially the physics of dipolar BECs.

| Species | Dipole moment | $a_{dd}$ |
|---|---|---|
| $^{52}$Cr | $6\mu_B$ | $15a_0$ |
| $^{164}$Dy | $9.9\mu_B$ | $130a_0$ |
| $^{166}$Er | $7\mu_B$ | $65.5a_0$ |
| KRb | $0.6D$ | $2 \times 10^3 a_0$ |

Table 2.1: Magnetic and electric dipole moments for different atomic and molecular species for which the quantum degenerate regime (BEC for $^{52}$Cr, $^{164}$Dy and $^{166}$Er, which are magnetic bosonic atoms, and a Fermi degenerate gas for KRb, which is instead fermionic molecule possessing a strong electric dipole moment) has been achieved. Here, $\mu_B$ is the Bohr magneton, while $a_0$ is the Bohr radius

### 2.1.2 Mean field theory

The Hamiltonian of a system of bosonic particles can be written, in second quantization, in terms of bosonic field operators $\hat{\Psi}$ and $\hat{\Psi}^\dagger$ as

$$\begin{aligned}\hat{H} = &\int d\mathbf{r}\hat{\Psi}^\dagger(\mathbf{r})\left[-\frac{\hbar^2\nabla^2}{2m} + V_{ext}(\mathbf{r})\right]\hat{\Psi}(\mathbf{r}) \\ &+ \int\int d\mathbf{r}d\mathbf{r}'\hat{\Psi}^\dagger(\mathbf{r})\hat{\Psi}^\dagger(\mathbf{r}')V(\mathbf{r}-\mathbf{r}')\hat{\Psi}(\mathbf{r}')\hat{\Psi}(\mathbf{r})\end{aligned} \tag{2.4}$$

where $V_{ext}(\mathbf{r})$ is an external trapping potential, and $V(\mathbf{r}-\mathbf{r}')$ is the interaction potential between two atoms. This interaction potential is in general difficult to calculate even in absence of dipole-dipole interaction, especially at small interatomic distances; however, at large distances, it is typically isotropic and decays according to the van der Waals law $r^{-6}$. A general result of scattering theory

[37] states that the low-energy scattering properties of isotropic interatomic potentials decaying, at large distances, as $r^{-n}$ with $n > 3$, can be fully described by a zero-range, isotropic pseudo-potential of the form

$$V(\mathbf{r}) = g\delta(\mathbf{r}) \tag{2.5}$$

where $g = \frac{4\pi\hbar^2 a}{m}$, $m$ is the atomic mass, and $a$ is the s-wave scattering length. This result comes from the fact that the complete scattering amplitude at low momenta in the case of fast decaying isotropic potentials becomes isotropic and energy-independent, and can be fully reproduced, at the level of the Born approximation, by the pseudo-potential 2.5. This description holds as long as the details of the interatomic interaction at short distances can be neglected, as it happens in the very dilute samples that form an ordinary BEC. It is thus customary to describe the interatomic interactions in an ordinary BEC via the contact pseudo-potential 2.5.
The same approximations are no longer valid if the atoms interact with a general isotropic potential at short distances, but also with the dipole-dipole potential 2.2 at long distances, the latter being anisotropic and decaying as $r^{-3}$. Nonetheless, it has been shown that, in these conditions, at least at the level of the Born approximation, the complete scattering amplitude is fully reproduced by the anisotropic, long-range pseudo-potential [38]

$$V(\mathbf{r}) = g\delta(\mathbf{r}) + \frac{C_{dd}}{4\pi}\frac{1-3\cos^2\theta}{r^3} \tag{2.6}$$

The use of the pseudo-potential 2.6 has become a standard practice in the description of dipolar BECs, and will be always used throughout this thesis.
Using the pseudo-potential 2.6, the Hamiltonian 2.4 can be thus rewritten as

$$\begin{aligned}\hat{H} = &\int d\mathbf{r}\hat{\Psi}^\dagger(\mathbf{r})\left[-\frac{\hbar^2\nabla^2}{2m} + V_{ext}(\mathbf{r})\right]\hat{\Psi}(\mathbf{r}) + g\int d\mathbf{r}\hat{\Psi}^\dagger(\mathbf{r})\hat{\Psi}^\dagger(\mathbf{r})\hat{\Psi}(\mathbf{r})\hat{\Psi}(\mathbf{r}) \\ &+ \frac{C_{dd}}{4\pi}\int\int d\mathbf{r}d\mathbf{r}'\hat{\Psi}^\dagger(\mathbf{r})\hat{\Psi}^\dagger(\mathbf{r}')\frac{1-3\cos^2\theta}{|\mathbf{r}-\mathbf{r}'|^3}\hat{\Psi}(\mathbf{r}')\hat{\Psi}(\mathbf{r})\end{aligned} \tag{2.7}$$

The equation of motion for the field $\hat{\Psi}$ is given, in the Heisenberg picture, by

$$\begin{aligned}i\hbar\frac{\partial\hat{\Psi}(\mathbf{r})}{\partial t} &= \left[\hat{\Psi}(\mathbf{r}), \hat{H}\right] \\ &= \left[-\frac{\hbar^2\nabla^2}{2m} + V_{ext}(\mathbf{r})\right]\hat{\Psi}(\mathbf{r}) + g\hat{\Psi}^\dagger(\mathbf{r})\hat{\Psi}(\mathbf{r})\hat{\Psi}(\mathbf{r}) \\ &\quad + \int d\mathbf{r}' V_{dd}(\mathbf{r}-\mathbf{r}')\hat{\Psi}^\dagger(\mathbf{r}')\hat{\Psi}(\mathbf{r}')\hat{\Psi}(\mathbf{r})\end{aligned} \tag{2.8}$$

where we have introduced the notation

$$V_{dd}(\mathbf{r}-\mathbf{r}') = \frac{C_{dd}}{4\pi}\frac{1-3\cos^2(\theta)}{|\mathbf{r}-\mathbf{r}'|^3} \tag{2.9}$$

Following the Bogolyubov prescription, we split the field operator $\hat{\Psi}$ in a classical field $\psi$, which describes the atoms in the lowest energy state, assumed to be macroscopically populated in the BEC phase, and a quantum field $\delta\hat{\psi}$ describing (quantum and thermal) fluctuations above the BEC

$$\hat{\Psi} = \psi + \delta\hat{\psi} \tag{2.10}$$

Inserting this expression in 2.8 and neglecting, at the lowest order of approximation, all the terms containing $\delta\hat{\psi}$, we obtain the *extended Gross-Pitaevskii equation*

$$i\hbar\frac{\partial\psi(\mathbf{r},t)}{\partial t} = \left[-\frac{\hbar^2\nabla^2}{2m} + V_{ext}(\mathbf{r}) + g|\psi(\mathbf{r},t)|^2 + \int d\mathbf{r}' V_{dd}(\mathbf{r}-\mathbf{r}')|\psi(\mathbf{r}',t)|^2\right]\psi(\mathbf{r},t) \tag{2.11}$$

which describes the dipolar BEC at the mean field level. The mean-field ground state of a dipolar BEC can be found by searching for solutions of 2.11 of the form $\psi(\mathbf{r},t) = \mathrm{e}^{-i\mu t/\hbar}\psi_0(\mathbf{r})$, and solving the eigenvalue problem

$$\begin{aligned}\mu\psi_0 &= \hat{H}_0\psi_0 \\ &= \left[-\frac{\hbar^2\nabla^2}{2m} + V_{ext}(\mathbf{r}) + g|\psi_0(\mathbf{r})|^2 + \int d\mathbf{r}' V_{dd}(\mathbf{r}-\mathbf{r}')|\psi_0(\mathbf{r}')|^2\right]\psi_0(\mathbf{r})\end{aligned} \tag{2.12}$$

for the smallest eigenvalue $\mu$. This can be interpreted as the chemical potential of the system, and fixes the total number of particles. Neglecting quantum and thermal fluctuations, we assume that *all* the atoms occupy the lowest energy state, in such a way that $\psi_0$ can be normalized according to

$$\int d\mathbf{r}|\psi_0(\mathbf{r})|^2 = N \tag{2.13}$$

where $N$ is the total number of atoms. Notice also that the ground-state condensate wave function $\psi_0$ can be also obtained in the context of a density-functional theory approach by minimizing the mean-field energy functional

$$\begin{aligned}E[\psi] = &\int d\mathbf{r}\psi^*(\mathbf{r})\left(-\frac{\hbar^2}{2m}\nabla^2 + V_{ext}(\mathbf{r})\right)\psi(\mathbf{r}) \\ &+ \frac{g}{2}\int d\mathbf{r}|\psi(\mathbf{r})|^4 \\ &+ \frac{1}{2}\int d\mathbf{r}d\mathbf{r}'|\psi(\mathbf{r})|^2 V_{dd}(\mathbf{r}-\mathbf{r}')|\psi(\mathbf{r}')|^2\end{aligned} \tag{2.14}$$

under the constraints of the normalization condition 2.13.
In order to study small fluctuations on top of a certain ground state solution $\psi_0$, satisfying equation 2.12, we follow the standard Bogolyubov-de Gennes (BdG) procedure and expand the classical field $\psi(\mathbf{r}, t)$ as

$$\psi(\mathbf{r}, t) = e^{-i\mu t/\hbar} \left\{ \psi_0(\mathbf{r}) + \sum_{n=1}^{\infty} \left[ u_n(\mathbf{r}) e^{-i\omega_n t} + v_n^*(\mathbf{r}) e^{i\omega_n t} \right] \right\} \tag{2.15}$$

Inserting this expansion in equation 2.11, assuming $\psi_0$ is real (as will be for all cases of interest for this thesis), and keeping only terms linear in the complex functions $u_n$ and $v_n$, we obtain the following BdG equations

$$\begin{pmatrix} \hat{H}_0 - \mu + \hat{X} & \hat{X}_0 \\ -\hat{X}_0 & -(\hat{H}_0 - \mu + \hat{X}_0) \end{pmatrix} \begin{pmatrix} u_n \\ v_n \end{pmatrix} = \hbar\omega_n \begin{pmatrix} u_n \\ v_n \end{pmatrix} \tag{2.16}$$

where $\hat{H}_0$ is given in 2.12, and the operator $\hat{X}_0$ is defined by its action on a general function $f$ as

$$\hat{X}_0 f(\mathbf{r}) = g|\psi_0(\mathbf{r})|^2 f(\mathbf{r}) + \psi_0(\mathbf{r}) \int d\mathbf{r}' V_{dd}(\mathbf{r} - \mathbf{r}') \psi_0(\mathbf{r}') f(\mathbf{r}') \tag{2.17}$$

Solving this eigenvalue problem allows to find the eigen-frequencies $\omega_n$ and eigen-modes $u_n$ and $v_n$ that characterize the elementary excitations of a dipolar BEC. In order to ensure that bosonic commutation relations are preserved, the quasi-particle amplitudes $u_n$ and $v_n$ are normalized according to

$$\int d\mathbf{r} \left( |u_n(\mathbf{r})|^2 - |v_n(\mathbf{r})|^2 \right) | = 1 \tag{2.18}$$

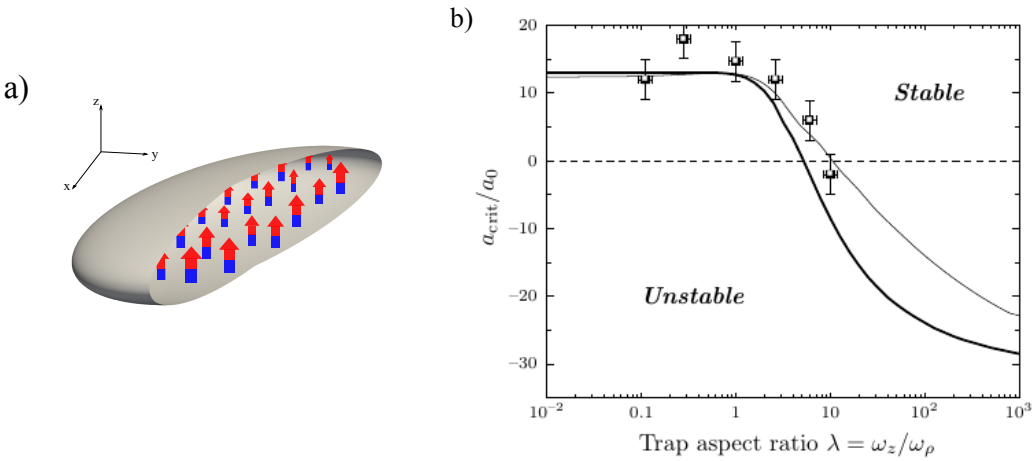


Figure 2.2: a) Schematic representation of a system of atomic dipoles, aligned along the z direction, in a pancake-shaped harmonic trap with short axis parallel to the polarization direction. b) Stability diagram, taken from [35], for a dipolar BEC of 20000 atoms of $^{52}$Cr. The experimental dots are taken from [39] and correspond to the measured values of the critical scattering length $a_{crit}(\lambda)$ at which the BEC collapses for a certain trap aspect ratio. The thin solid line correspond to the value of $a_{crit}(\lambda)$ calculated using the mean-field eGPE 2.11, while the thick solid line corresponds to a variational estimate of the value of $a_{crit}(\lambda)$ obtained from a gaussian ansatz (see [35] for details).

The mean-field model has been shown to accurately describe the phase diagram and the post-collapse expansion dynamics of a dipolar BEC of weakly magnetic $^{52}$Cr atoms, for which the dipolar length is $a_{dd} \simeq 15a_0$ 2.1[39, 40]. In particular, it has been shown that, confining the dipolar BEC in a pancake-shaped harmonic trap, with the short axis parallel to the polarization direction, it is possible to obtain a stable dipolar BEC even at very small values of the scattering length (in extreme cases, even slightly negative). The critical value of the scattering length at which the collapse is observed decreases with an increase of the trap aspect ratio (see figure 2.2 panel b). Intuitively, this can be understood to be a consequence of the confinement along the polarization direction, that prevents the dipoles from reaching the attractive head-to-tail configuration(see figure 2.2 panel a). Moreover, the post collapse expansion dynamics is characterized by a peculiar d-wave shape, that resembles the anisotropy of the dipolar potential, and is well captured by the mean-field model after taking into account the effects of three-body losses[40]. However, the mean-field model fails in describing the observed properties of dipolar

BECs of atoms with a magnetic moment much stronger then the one of $^{52}$Cr, as for example $^{164}$Dy and $^{166}$Er. In this case, in the mean-field instability region of the phase diagram, one can observe the formation of peculiar self-bound liquid-like droplets [6, 41] that can eventually arrange into a regular, periodic configuration, in a sort of droplet crystal. As will be discussed in depth later, it is possible to fine tune the system parameters in such a way to establish phase coherence between the droplets in the droplet crystal, realizing a *supersolid*, a peculiar state of matter showing both superfluidity and crystal properties. To describe these aspects, it is necessary to go beyond a mean-field description of the system, as will be discussed in the next section.

### 2.1.3 Beyond mean field: the Lee-Huang-Yang correction

The mean-field eGPE 2.11 has been shown to be accurate in describing the phase diagram and the post-collapse dynamics of a dipolar BEC of weakly magnetic atoms of $^{52}$Cr[39]. However, it fails in predicting the structures (supersolids, quantum droplets and droplet crystals) observed in the mean-field instability regions of the phase diagram of BECs of $^{164}$Dy and $^{166}$Er, which possess a stronger magnetic dipole moment. In order to account for these effects, the state-of-the-art description of dipolar BECs takes into account also the first-order beyond mean field correction to the ground state energy and chemical potential of the system [7, 41]. The fundamental idea, based on a similar one proposed for Bose-Bose mixtures [42], is that, as a dipolar BEC collapses driven by the attractive part of the dipole-dipole interaction, which produces a negative mean-field energy term, quantum fluctuations increases producing a positive energy term that eventually balances the mean-field one resulting in a final stable state. We will first consider the case of a uniform BEC, and then generalize to the non-uniform case using the local density approximation.
For a homogeneous dipolar BEC in three spatial dimensions, the first order beyond-mean-field correction to the ground state energy is given by [43, 44]

$$\frac{E_0}{V} = \frac{1}{2} g n^2 \left[ 1 + \frac{128}{15\sqrt{\pi}} \sqrt{n a^3} F(\varepsilon_{dd}) \right] \tag{2.19}$$

where

$$F(\varepsilon_{dd}) = \frac{1}{2} \int_0^\pi d\theta \sin\theta [1 + \varepsilon_{dd}(3\cos^2\theta - 1)]^{\frac{5}{2}} \tag{2.20}$$

Details of the calculations are given in Appendix A. Notice that this correction introduces a positive shift in the ground-state energy of the system via a term proportional to $n^{\frac{5}{2}}$, where $n = N/V$ is the density of the system, $N$ being the total number of atoms and $V$ the volume.

The simplest way to take into account the beyond-mean-field correction 2.19 for the description of a non-homogeneous dipolar system is to follow a density-functional-theory approach, starting from the mean-field energy functional 2.14 and adding the LHY correction in local density approximation (LDA). The energy functional becomes

$$\begin{aligned} E[\psi] = &\int d\mathbf{r}\psi^*(\mathbf{r}) \left( -\frac{\hbar^2}{2m}\nabla^2 + V_{ext}(\mathbf{r}) \right) \psi(\mathbf{r}) \\ &+ \frac{g}{2}\int d\mathbf{r}|\psi(\mathbf{r})|^4 \\ &+ \frac{1}{2}\int d\mathbf{r}d\mathbf{r}'|\psi(\mathbf{r})|^2 V_{dd}(\mathbf{r}-\mathbf{r}')|\psi(\mathbf{r}')|^2 \\ &+ \frac{2}{5}\gamma(\varepsilon_{dd})\int d\mathbf{r}|\psi(\mathbf{r})|^5 \end{aligned} \tag{2.21}$$

where we have introduced

$$\gamma(\varepsilon_{dd}) = \frac{32}{3\sqrt{\pi}} g a^{\frac{3}{2}} F(\varepsilon_{dd}) \tag{2.22}$$

Minimizing this energy functional under the constraint 2.13 leads to the new equation for the ground-state wave function

$$\begin{aligned} \mu\psi = &\Big[ -\frac{\hbar^2\nabla^2}{2m} + V_{ext}(\mathbf{r}) + g|\psi(\mathbf{r})|^2 + \gamma(\varepsilon_{dd})|\psi(\mathbf{r})|^3 \\ &+ \int d\mathbf{r}' V_{dd}(\mathbf{r}-\mathbf{r}')|\psi(\mathbf{r}')|^2 \Big] \psi(\mathbf{r}) \end{aligned} \tag{2.23}$$

Solving this eigenvalue problem for the smallest eigenvalue $\mu$ allows to study the ground state-wave function and density profiles in presence of quantum fluctuations. The dynamics can instead be studied by considering the time-dependent version of equation 2.23, which reads

$$\begin{aligned} i\hbar\frac{\partial\psi(\mathbf{r},t)}{\partial t} = &\Big[ -\frac{\hbar^2\nabla^2}{2m} + V_{ext}(\mathbf{r}) + g|\psi(\mathbf{r},t)|^2 + \gamma(\varepsilon_{dd})|\psi(\mathbf{r},t)|^3 \\ &+ \int d\mathbf{r}' V_{dd}(\mathbf{r}-\mathbf{r}')|\psi(\mathbf{r}',t)|^2 \Big] \psi(\mathbf{r},t) \end{aligned} \tag{2.24}$$

The BdG equations 2.16 are instead modified replacing $\hat{H}_0$ and $\hat{X}_0$ with the operators $\hat{H}$ and $\hat{X}$ defined as

$$\begin{aligned} \hat{H} &= \hat{H}_0 + \gamma(\varepsilon_{dd})|\psi_0|^3 \\ \hat{X} &= \hat{X}_0 + \frac{3}{2}\gamma(\varepsilon_{dd})|\psi_0|^3 \end{aligned} \tag{2.25}$$

where $\psi_0$ is the solution of 2.23.
The beyond-mean-field model, together with the local density approximation, has been shown to give results compatible with exact quantum Monte Carlo calculations in the quantum droplet regime [45, 46], but also to describe reasonably well the phenomenology observed in recent experiments. This comes from the fact that the LHY correction is dominated by fluctuations with a wavelength much smaller then the typical droplet size [7], so that the bulk of the positive energy shift due to quantum fluctuations is well described also cutting off the contribution coming from long-wavelength modes. This model will thus be used to obtain all the results presented in the thesis.

## 2.2 Linear response theory

In this thesis, I often consider the behavior of a dipolar Bose gas in response to a small external perturbation. This procedure is a fundamental tool that allows to study the structure and physical properties of general many-body systems. In fact, if the perturbation is small enough, the response of the system typically depends *linearly* on the strength of the perturbation, a fact that allows the systematic development of several useful theoretical tools and to compare theory and experiments. In this section, I will sketch the basic tools of linear response theory used in this thesis, following [2].

### 2.2.1 Response function and dynamic structure factor

Let us consider a general many-body system described by the Hamiltonian $\hat{H}$, and let us suppose that, at time $t = 0$, we switch on the perturbation

$$\hat{H}_{pert}(t) = -\lambda \hat{G} \mathrm{e}^{-i\omega t} \mathrm{e}^{\eta t} - \lambda^* \hat{G}^\dagger \mathrm{e}^{i\omega t} \mathrm{e}^{\eta t} \tag{2.26}$$

where $\lambda$ is the strength of the perturbation, supposed to be small enough to apply linear response theory, $\eta$ is a small positive parameter ensuring that the perturbation is zero at $t \to -\infty$, and $\hat{G}$ is the excitation operator. In general, we want to study the response of a certain operator $\hat{F}$ to the perturbation operator $\hat{G}$. In linear response theory, we write the fluctuation $\langle \delta \hat{F}^\dagger \rangle$ of the operator $\hat{F}$ induced by the excitation operator $\hat{G}$ as

$$\langle \delta \hat{F}^\dagger \rangle = \lambda \mathrm{e}^{-i\omega t} \mathrm{e}^{\eta t} \chi_{\hat{F}^\dagger \hat{G}}(\omega) + \lambda^* \mathrm{e}^{i\omega t} \mathrm{e}^{\eta t} \chi_{\hat{F}^\dagger \hat{G}^\dagger}(-\omega) \tag{2.27}$$

where the function $\chi$ is called *dynamic polarizability* or *response function* of the system. This function depends only on the properties of the system and, once

known, it determines its linear response to small perturbations. In equilibrium at a certain temperature $T$, the linear response function is given by

$$\chi_{\hat{F}^\dagger\hat{G}}(\omega) = -\frac{1}{\hbar}Q^{-1}\sum_{m,n} \mathrm{e}^{-\beta E_{m,n}} \left[\frac{\langle m|\hat{F}^\dagger|n\rangle\langle n|\hat{G}|m\rangle}{\omega - \omega_{n,m} + i\eta} - \frac{\langle m|\hat{G}|n\rangle\langle n|\hat{F}^\dagger|m\rangle}{\omega + \omega_{n,m} + i\eta}\right] \quad (2.28)$$

where $|n\rangle$ are the excited states of the system with energy $E_n$, $\omega_{n,m} = \frac{E_n - E_m}{\hbar}$ are the transition frequencies, and $Q = \sum_n \mathrm{e}^{-\beta E_m}$ is the canonical partition function, $\beta$ being linked to the Boltzmann constant by $\beta = 1/k_B T$.
Let us now specialize to the case $\hat{F} = \hat{G}$. It is useful to define the *dynamic structure factor* relative to the operator $\hat{F}$ as

$$S_{\hat{F}}(\omega) = Q^{-1}\sum_{m,n} \mathrm{e}^{-\beta\hbar\omega_{m,n}} |\langle n|\hat{F}|m\rangle|^2 \delta(\hbar\omega - \hbar\omega_{m,n}) \quad (2.29)$$

using which the linear response function can be written as

$$\chi_{\hat{F}}(\omega) = \int_{-\infty}^{\infty} d\omega' \left[\frac{S_{\hat{F}}(\omega')}{\omega - \omega' + i\eta} - \frac{S_{\hat{F}^\dagger}(\omega')}{\omega + \omega' + i\eta}\right] \quad (2.30)$$

Using the dynamic structure factor, the imaginary part of the response function can be written as

$$Im\chi_{\hat{F}}(\omega) = \pi(1 - \mathrm{e}^{-\beta\hbar\omega}) S_{\hat{F}}(\omega) \quad (2.31)$$

and, using second order perturbation theory, it can be related to the rate of energy exchange between the system and the perturbation as

$$\begin{aligned} \frac{dE}{dt} &= 2|\lambda|^2 \omega Im\chi_{\hat{F}}(\omega) \\ &= 2\pi|\lambda|^2\omega(S_{\hat{F}}(\omega) - S_{\hat{F}^\dagger}(-\omega)) \end{aligned} \quad (2.32)$$

This relation also shows that the energy exchange rate between the system and the perturbation is given by two terms: a positive term, proportional to $S_{\hat{F}}(\omega)$, that gives the energy absorbed by the system, and a negative one proportional to $S_{\hat{F}^\dagger}(-\omega)$ which gives the energy extracted from the system.
At $T = 0$, the expression for the dynamic structure factor becomes a little simpler. In fact, at $T = 0$ the system is supposed to be in its ground state, and hence we only need to consider matrix elements of $\hat{F}$ or $\hat{G}$ only between the ground state $|0\rangle$ and the excited states $|n\rangle$. The expression of the dynamic structure factor is thus simplified as

$$S_{\hat{F}}(\omega) = \sum_n |\langle n|\hat{F}|0\rangle|^2 \delta(\hbar\omega - \hbar\omega_n) \quad (2.33)$$

Notice that, at $T = 0$, we must have $S_{\hat{F}}(\omega < 0) = 0$, since at zero temperature the system is already in its ground state and no energy can be extracted from it.

### 2.2.2 Sum rules

In general, it is difficult to calculate either $\chi_{\hat{F}}$ or $S_{\hat{F}}(\omega)$ starting from the general many-body Hamiltonian of the system. However, interesting informations can be extracted by studying the *energy-weighted moments* of the dynamic structure factor.
The *p-th* order energy-weighted moment of the dynamic structure factor is defined as

$$m_p(\hat{F}) = \hbar^{p+1} \int_{-\infty}^{\infty} d\omega \omega^p S_{\hat{F}}(\omega) \tag{2.34}$$

Such moments are related in an interesting way to the commutators (and anti-commutators) of the operator $\hat{F}$ with the Hamiltonian $\hat{H}$ and to the energy of the elementary excitations of the system. They often provide good estimates of the excitation frequencies related to the excited states of the system, but also universal relations valid for very general systems.
Let us start with the zero energy-weighted moment of the dynamic structure factor. It is easy to see that it can be calculated as

$$\begin{aligned} m_0(\hat{F}) &= \hbar^2 Q^{-1} \sum_m \mathrm{e}^{-\beta E_m} \langle m|\hat{F}\hat{F}^\dagger|m\rangle \\ &= Tr(\hat{F}\hat{F}^\dagger) \\ &= \langle \hat{F}\hat{F}^\dagger \rangle \end{aligned} \tag{2.35}$$

from which one easily finds the following sum rules

$$\begin{aligned} m_0(\hat{F}) + m_0(\hat{F}^\dagger) &= \langle \{\hat{F}, \hat{F}^\dagger\} \rangle \\ m_0(\hat{F}) - m_0(\hat{F}^\dagger) &= \langle [\hat{F}, \hat{F}^\dagger] \rangle \end{aligned} \tag{2.36}$$

Similarly, the following sum rules are valid for the first energy-weighted moment

$$\begin{aligned} m_1(\hat{F}) + m_1(\hat{F}^\dagger) &= \langle [\hat{F}^\dagger, [\hat{H}, \hat{F}]] \rangle \\ m_1(\hat{F}) - m_1(\hat{F}^\dagger) &= \langle \{\hat{F}^\dagger, \{\hat{H}, \hat{F}\}\} \rangle \end{aligned} \tag{2.37}$$

At $T = 0$, it is possible to derive rigorous upper bounds on the energy of the modes excited by the perturbation operator $\hat{F}$. In fact, the energy-weighted moments can be written explicitly as

$$m_p = \sum_n |\langle n|\hat{F}|0\rangle|^2 \omega_n^p \tag{2.38}$$

from which one easily obtains

$$\begin{aligned} \frac{m_{p+1}}{m_p} &= \frac{\sum_n |\langle n|\hat{F}|0\rangle|^2 \omega_n^p \omega_n}{\sum_n |\langle n|\hat{F}|0\rangle|^2 \omega_n^p} \\ &\geq \omega_{min} \end{aligned} \tag{2.39}$$

where $\hbar\omega_{min}$ is the energy of the mode with smallest energy excited by $\hat{F}$. We thus have the rigorous upper bound

$$\omega_{min} \leq \frac{m_{p+1}}{m_p} \tag{2.40}$$

These inequalities become equalities in the case in which the response of the system is exhausted by a single mode only (single-mode approximation).
Similarly to 2.39, it is possible to find the following recursive relation

$$\frac{m_{p+1}}{m_p} \geq \frac{m_p}{m_{p-1}} \tag{2.41}$$

from which, for $p = 0$, one finds the useful relation

$$m_0 \leq \sqrt{m_1 m_{-1}} \tag{2.42}$$

The inverse energy-weighted moment $m_{-1}$ is related to the *static* response of the system, and allows to define the *static response function* as

$$\begin{aligned} m_{-1} &= \int_{-\infty}^{\infty} d\omega \frac{1}{\omega} S_{\hat{F}}(\omega) \\ &= \sum_n \frac{|\langle n|\hat{F}|0\rangle|^2}{\omega_n} \\ &= \frac{1}{2}\chi_{\hat{F}}(\omega = 0) \end{aligned} \tag{2.43}$$

where $\chi_{\hat{F}}(\omega = 0)$ describes the response of the system to a static perturbation.

### 2.2.3 Density response

As a concrete example, let us now consider the important case in which the operator $\hat{F}$ is the density operator in Fourier space. More specifically, the density operator can be defined as

$$\hat{n}(\mathbf{r}) = \sum_i \delta(\mathbf{r} - \mathbf{r}_i) \tag{2.44}$$

where the sum is extended to all the particles in the system. The Fourier transform of this operator is

$$\hat{\rho}_{\mathbf{k}} = \int d\mathbf{r} \mathrm{e}^{-i\mathbf{k}\cdot\mathbf{r}} \hat{n}(\mathbf{r}) \tag{2.45}$$

We now make the choice

$$\hat{F} = \hat{G} = \delta\rho_{\mathbf{k}}^\dagger = \rho_{\mathbf{k}}^\dagger - \langle\rho_{\mathbf{k}}^\dagger\rangle \tag{2.46}$$

where the average is calculated at equilibrium. The response function and the dynamic structure factor can thus be written as

$$\chi(\mathbf{k},\omega) = -\frac{1}{\hbar}Q^{-1}\sum_{m,n} \mathrm{e}^{-\beta E_{m,n}} \left[\frac{|\langle m|\delta\rho_{\mathbf{k}}|m\rangle|^2}{\omega-\omega_{n,m}+i\eta} - \frac{|\langle m|\delta\rho_{\mathbf{k}}^\dagger|m\rangle|^2}{\omega+\omega_{n,m}+i\eta}\right]$$
$$S(\mathbf{k},\omega) = \sum_n |\langle n|\delta\rho_{\mathbf{k}}^\dagger|0\rangle|^2\delta(\hbar\omega-\hbar\omega_n) \tag{2.47}$$

We now consider systems at equilibrium at $T = 0$, where the proofs are easier, although the results we will find are also valid at finite temperature. Suppose, moreover, that we have a system symmetric under parity, such that the Fourier transform of the density operator satisfies

$$\hat{\rho}_{\mathbf{k}} = \hat{\rho}_{-\mathbf{k}} = \hat{\rho}_{-\mathbf{k}}^\dagger = \hat{\rho}_{\mathbf{k}}^\dagger \tag{2.48}$$

It is easy then to show that the dynamic structure factor satisfies

$$S(\mathbf{k},\omega) = S(-\mathbf{k},\omega) \tag{2.49}$$

Using these symmetry properties and the sum rules 2.37, we easily find

$$m_1(\mathbf{k}) = \frac{1}{2}\langle\left[\delta\hat{\rho}_{\mathbf{k}}^\dagger,\left[\hat{H},\delta\hat{\rho}_{\mathbf{k}}\right]\right]\rangle \tag{2.50}$$

If the Hamiltonian can be split in a kinetic term and a velocity-independent potential as $\hat{H} = \hat{T} + \hat{V}$, then the density operator commutes with the potential, while, writing the kinetic energy operator as $\hat{T} = \sum_i \frac{\hat{p}_i^2}{2m}$, its commutator with the density operator is easily evaluated and gives

$$\left[\hat{T},\hat{\rho}_{\mathbf{k}}\right] = -\hbar\mathbf{k}\cdot\hat{\mathbf{j}} \tag{2.51}$$

where we have defined the current density operator as

$$\hat{\mathbf{j}} = \sum_i \left[\hat{\mathbf{p}}_i \mathrm{e}^{-i\mathbf{k}\cdot\mathbf{r}_i} + \mathrm{e}^{-i\mathbf{k}\cdot\mathbf{r}_i}\hat{\mathbf{p}}_i\right] \tag{2.52}$$

Using this expression to evaluate the double commutator, one finds the model independent result

$$m_1 = N\frac{\hbar^2k^2}{2m} \tag{2.53}$$

which is known as the *f-sum rule*, and is often used, also in this thesis, to check the consistency of the calculations. Using the inequality 2.40 with $p = 0$ and the f-sum rule, one finds

$$\omega_{min}(\mathbf{k}) = \frac{m_1}{m_0} = \frac{\hbar^2k^2}{2mS(\mathbf{k})} \tag{2.54}$$

where we have defined the *static structure factor* $S(\mathbf{k})$ as

$$S(\mathbf{k}) = \frac{1}{N} m_0(\mathbf{k}) = \frac{1}{N} \sum_n |\langle n|\delta\hat{\rho}_{\mathbf{k}}^\dagger|0\rangle|^2 \tag{2.55}$$

Relation 2.54 is known as the *Feynman relation*, and gives the energy-momentum dispersion relation if the single-mode approximation is fulfilled, i.e. if the density operator excites only a single mode of the system (otherwise, it provides an upper bound on such frequency).

## 2.3 Numerical methods

The results presented in this thesis are mostly based on the numerical solution of the beyond-mean-field extended Gross-Pitaevskii equation 2.24 or its static counterpart 2.23, as well as solutions of the Bogolyubov-de Gennes (BdG) equations 2.16 with the beyond-mean-field correction 2.25.
In particular, three classes of physical properties of dipolar BECs are considered

- Ground-state properties, which include, for example, density profiles or ground state expectation values of observables; both of these can be calculated from the solution $\psi$ of equation 2.23 corresponding to the lowest eigenvalue $\mu$, which represents the chemical potential of the system for a fixed set of system parameters;
- elementary excitations, including excitations spectra or the static and dynamic structure factor, which can be studied from solutions of the BdG equations;
- dynamical properties, including the behavior of the system following realistic experimental protocols, or under the action of some external perturbation; these can be studied from solutions of 2.24 for suitable initial conditions.

Analytical solutions of such complex, non-linear integral-differential problems are extremely difficult to find and can be studied only in very specific cases (see, e.g., [47]). Instead, numerical solutions can be found (almost) always with very good accuracy, and allow in particular to compare predictions of our models with results of experiments.
Let us take a loser lok at the numerical algorithms used in these thesis.

### 2.3.1 Ground-state properties

Studying (theoretically, or numerically) ground state properties of a dipolar BEC means solving equation 2.23 to obtain the solution $\psi$, which is physically interpreted as the condensate ground-state wave function. Knowing $\psi$, one can evaluate

observables of interest, such as ground state density profiles $\rho(\mathbf{r}) = |\psi(\mathbf{r})|^2$, momentum distributions $|\tilde{\psi}_{\mathbf{k}}|^2$ (where $\tilde{\psi}_{\mathbf{k}}$ is the Fourier transform of $\psi$), or equilibrium expectation values of any operator $\hat{O}$

$$\langle \hat{O} \rangle = \frac{\langle \psi | \hat{O} | \psi \rangle}{\langle \psi | \psi \rangle} \tag{2.56}$$

Since we cannot access the exact functional form of $\psi(\mathbf{r})$, we must be content with calculating numerically its values at the points of a mesh in either real or momentum space. From now on, it will always be assumed implicitly that $\psi(\mathbf{r})$ is evaluated at the points of a regular cartesian mesh in real space, while its Fourier transform $\tilde{\psi}_{\mathbf{k}}$ is evaluated at the points $\mathbf{k}$ of the corresponding reciprocal mesh in momentum space.
The problem of calculating the solution $\psi$ of equation 2.23 can be formulated as a constrained minimization problem, exploiting the fact that the ground-state condensate wave function can be defined as the exact minimizer of the energy functional 2.21, under the normalization constraint 2.13 that fixes the total number of atoms (i.e., the $L^2$ norm of $\psi$). We implement such minimization procedure iteratively, using a line search method known as *gradient descent* [48]. The idea is to start from a guess solution $\psi_0$ and generate a sequence of iterates $\{\psi_n\}_{n=0,\dots\infty}$ that terminates when we are sufficiently confident to have reached a (hopefully global) minimizer of the functional 2.21 with good accuracy. In particular, a good stopping criterion consists in fixing a tolerance threshold $\varepsilon$ for the norm of the residual, i.e.

$$||\hat{H}\psi_n - \mu_n \psi_n||^2 \leq \varepsilon \tag{2.57}$$

where $\hat{H}$ is given by 2.25 and the estimate $\mu_n$ of the chemical potential $\mu$ at iteration $n$ can be calculated from equation 2.23 as

$$\mu_n = \frac{\langle \psi_n | \hat{H} | \psi_n \rangle}{\langle \psi_n | \psi_n \rangle} \tag{2.58}$$

For the results presented in this thesis, we typically choose a tolerance $\varepsilon \leq 10^{-6}$.
In deciding how to move from one iterate $\psi_n$ to the next $\psi_{n+1}$, line search algorithms use information about the functional $E[\psi]$ at $\psi_n$, and possibly also from earlier iterates $\psi_0$, $\psi_1$, $\dots$ $\psi_{n-1}$. The update criterion should be that the energy functional is smaller in $\psi_{n+1}$ then in $\psi_n$. One thus generates a sequence

$$\psi_{n+1} = \psi_n + \alpha \chi_n \tag{2.59}$$

such that $E[\psi_{n+1}] < E[\psi_n] < \cdots < E[\psi_0]$ until the stopping criterion 2.57 is satisfied. The update "direction" $\chi_n$ must thus be chosen to be a *descent direction*, i.e. a direction along which the functional $E[\psi]$ decreases. The step-length $\alpha$

should instead be (ideally) chosen in such a way that the decrease in the energy functional $E[\psi]$ from $\psi_n$ to $\psi_{n+1}$ is, at each iteration step, the maximum possible. Since this is not an easy task, we instead accepted the compromise to choose the step length $\alpha$ empirically at the beginning of the iteration procedure.
The gradient descent method consists in choosing the descent direction $\chi_n$ as the opposite of the gradient of the functional $E[\psi]$ calculated in $\psi_n$. In particular, in our case, the descent direction is (minus) the functional derivative of the energy functional with respect to $\psi^*$ evaluated at $\psi_n$, i.e.

$$\chi_n = -\frac{\delta E[\psi_n]}{\delta \psi^*} = \tag{2.60}$$

$$-\Big[-\frac{\hbar^2\nabla^2}{2m} + V_{ext}(\mathbf{r}) + g|\psi_n(\mathbf{r})|^2 + \gamma(\varepsilon_{dd})|\psi_n(\mathbf{r})|^3$$

$$+\int d\mathbf{r}' V_{dd}(\mathbf{r}-\mathbf{r}')|\psi_n(\mathbf{r}')|^2\Big]\psi_n(\mathbf{r}) \tag{2.61}$$

The normalization condition 2.13 fixing the $L^2$ norm of $\psi$ should be included in the iteration procedure by introducing a Lagrange multiplier and minimizing the corresponding lagrangian functional[48]. In practice, we find much cheaper to normalize "by hand" each $\psi_n$ obtained via the iterative procedure just described, by fixing

$$\begin{aligned}\psi_{n+1}^{(1)} &= \psi_n + \alpha\chi_n \\ \psi_{n+1} &= \sqrt{\frac{N}{\int d\mathbf{r}|\psi_{n+1}^{(1)}|^2(\mathbf{r})}}\psi_{n+1}^{(1)}\end{aligned} \tag{2.62}$$

Finally, we employ an acceleration algorithm, known as the *heavy ball method* [49, 50], in order to speed up the convergence of the sequence $\{\psi_n\}_{n=0,\dots\infty}$. The method consists in adding a "momentum" term into the iterations 2.59, in order to make larger steps if the descent direction doesn't change very much, and smaller steps if it changes a lot. In practice, what one does is just to modify expression 2.59 in

$$\psi_{n+1} = \psi_n + \alpha\chi_n + \beta(\psi_n - \psi_{n-1}) \tag{2.63}$$

where, again, $\beta$ is a parameter chosen empirically. We have found that this small trick can decrease the number of iterations needed to reach convergence even by orders of magnitude.

### 2.3.2 Elementary excitations

The elementary excitations of a dipolar BEC on top of a certain ground-state solution can be studied by solving the Bogolyubov-de Gennes equations 2.16, taking

also into account the beyond-mean-field correction 2.25. The numerical solution of these equations is computationally demanding in three spatial dimensions (as will always be the case in this thesis), especially due to the presence of the integral terms that arise from the non-local character of the dipole-dipole interaction potential. However, several tricks can be used to make the problem tractable.
We set periodic boundary conditions, since the use of Fourier transforms simplifies the problem of evaluating non-local terms due to the presence of the dipole-dipole interaction, and allows to easily jump from a real to a momentum space description of the problem whenever needed.
Having fixed periodic boundary conditions, momentum $\mathbf{k}$ is a good quantum number labelling the elementary excitations of the system, and the Bogolyubov quasiparticle amplitudes can be factorized, using Bloch theorem [51], as

$$\begin{aligned} u_n(\mathbf{r}) &= \mathrm{e}^{i\mathbf{k}\cdot\mathbf{r}} u_{n,\mathbf{k}}(\mathbf{r}) \\ v_n(\mathbf{r}) &= \mathrm{e}^{i\mathbf{k}\cdot\mathbf{r}} v_{n,\mathbf{k}}(\mathbf{r}) \end{aligned} \tag{2.64}$$

where $u_{n,\mathbf{k}}(\mathbf{r})$ and $v_{n,\mathbf{k}}(\mathbf{r})$ have now the same periodicity of the simulation cell. We can expand these two functions in plane waves as

$$\begin{aligned} u_{n,\mathbf{k}}(\mathbf{r}) &= \sum_{n,\mathbf{G}} u_{\mathbf{G}} e^{i\mathbf{G}\cdot\mathbf{r}} \\ v_{n,\mathbf{k}}(\mathbf{r}) &= \sum_{n,\mathbf{G}} v_{\mathbf{G}} e^{i\mathbf{G}\cdot\mathbf{r}} \end{aligned} \tag{2.65}$$

where the vectors $\mathbf{G}$ are the reciprocal lattice vectors associated with the mesh in real space.
The same expansion can clearly be done also for the condensate wave function

$$\psi(\mathbf{r}) = \sum_{\mathbf{G}} \psi_{\mathbf{G}} e^{i\mathbf{G}\cdot\mathbf{r}} \tag{2.66}$$

Inserting these expressions in the BdG equations 2.16, taking also into account the correction 2.25, we obtain the eigenvalue problem

$$\begin{bmatrix} \mathbf{A}+\mathbf{B} & \mathbf{B} \\ -\mathbf{B} & -\mathbf{A}-\mathbf{B} \end{bmatrix} \begin{bmatrix} u_{n,\mathbf{k}} \\ v_{n,\mathbf{k}} \end{bmatrix} = \hbar\omega_{n,\mathbf{k}} \begin{bmatrix} u_{,n\mathbf{k}} \\ v_{n,\mathbf{k}} \end{bmatrix} \tag{2.67}$$

where the matrices $\mathbf{A}$ and $\mathbf{B}$ are defined as

$$\begin{aligned} \mathbf{A}_{\mathbf{G},\mathbf{G}'} &= \left[ \frac{\hbar^2(\mathbf{k}+\mathbf{G})^2}{2m} - \mu \right] \delta_{\mathbf{G},\mathbf{G}'} + \tilde{U}_{\mathbf{G}-\mathbf{G}'} \\ \mathbf{B}_{\mathbf{G},\mathbf{G}'} &= \sum_{\mathbf{G}''} \psi_{\mathbf{G}-\mathbf{G}''} \tilde{V}_{\mathbf{k}+\mathbf{G}''} \psi_{\mathbf{G}''-\mathbf{G}'} + \tilde{C}_{\mathbf{G},\mathbf{G}'} \end{aligned} \tag{2.68}$$

where we have also defined

$$\sum_{\mathbf{G}} \tilde{U}_{\mathbf{G}} \mathrm{e}^{i\mathbf{G}\cdot\mathbf{r}} = V_{ext}(\mathbf{r}) + \int d\mathbf{r}' V_{dd}(\mathbf{r}-\mathbf{r}')|\psi(\mathbf{r}')^2| + \gamma(\varepsilon_{dd})|\psi(\mathbf{r})|^3$$
$$\sum_{\mathbf{G}} \tilde{C}_{\mathbf{G}} \mathrm{e}^{i\mathbf{G}\cdot\mathbf{r}} = \frac{3}{2}\gamma(\varepsilon_{dd})|\psi(\mathbf{r})|^3 \tag{2.69}$$

Solving this non-symmetric eigenvalue problem may be computationally very expensive. Important simplifications may however be obtained with some trick. In fact, the eigenvalue problem can easily be rewritten as

$$\begin{cases} \mathbf{A}(\mathbf{A}+2\mathbf{B})(u_{n,\mathbf{k}}+v_{n,\mathbf{k}}) = (\hbar\omega_{n,\mathbf{k}})^2(u_{n,\mathbf{k}}+v_{n,\mathbf{k}}) \\ \mathbf{A}(u_{n,\mathbf{k}}-v_{n,\mathbf{k}}) = (\hbar\omega_{n,\mathbf{k}})(u_{n,\mathbf{k}}+v_{n,\mathbf{k}}) \end{cases} \tag{2.70}$$

Notice that the first equation in 2.70 defines a (still non-symmetric) eigenvalue problem of *half* the size of the original one 2.67, from which the spectrum of the elementary excitations can be readily calculated. The eigenvectors in this case correspond to the sum $(u_{n,\mathbf{k}}+v_{n,\mathbf{k}})$, which can be then be inserted in the second equation of 2.70. One can finally calculate $(u_{n,\mathbf{k}}-v_{n,\mathbf{k}})$ by solving a (numerically simple) linear system, and finally obtain $u_{n,\mathbf{k}}$ and $v_{n,\mathbf{k}}$ by sums and differences. A final simplification comes from noticing that, if we consider (like we often do) configurations in which the chemical potential is positive (e.g., because the system is not self-bound, or if the external potential lifts its value), the matrix $\mathbf{A}$ is symmetric and positive definite, so that we can take its Cholesky factorization [52]

$$\mathbf{A} = \mathbf{L}\mathbf{L}^T \tag{2.71}$$

where $\mathbf{L}$ is a lower triangular matrix and $\mathbf{L}^T$ is its transpose. Then, the system 2.70 can be rewritten as

$$\begin{cases} \mathbf{S} z_{n,\mathbf{k}} = (\hbar\omega_{n,\mathbf{k}})^2 z_{n,\mathbf{k}} \\ \mathbf{L}^T(u_{n,\mathbf{k}}-v_{n,\mathbf{k}}) = (\hbar\omega_{n,\mathbf{k}}) z_{n,\mathbf{k}} \end{cases} \tag{2.72}$$

where $\mathbf{S} = \mathbf{L}^T(\mathbf{A}+2\mathbf{B})\mathbf{L}$ is now a symmetric matrix, and $z_{n,\mathbf{k}} = \mathbf{L}^{-\mathbf{1}}(u_{n,\mathbf{k}}+v_{n,\mathbf{k}})$. So, the eigenvalue problem defined in the first equation of 2.72 can be solved using some iterative, high-performance method, such as the Lanczos method [52], while the successive linear system can be solved by simple substitution. Noticing that inverting a lower triangular matrix is a computationally cheap task, and so the real bottleneck of the algorithm becomes the formation of the matrix $\mathbf{S}$ by matrix multiplications (which is, anyway, an operation that can be parallelized). For the results presented in this thesis, the system of equations 2.72 is solved using LAPACK routines [53].

### 2.3.3 Dynamics

Dynamical properties of the dipolar BEC, as for example the behavior of the system following realistic experimental protocols, or the response of the system to various kinds of linear or non-linear perturbations, can be studied by solving equation 2.24 in time for suitable initial conditions. The approach we use to solve this non-linear partial integral-differential equation is a simple fourth-order Runge-Kutta algorithm (RK4) [54].
In order to solve a general first order differential equation in time

$$\begin{aligned} \frac{dy}{dt} &= f(y,t) \\ y(0) &= y_0, t \in [0,T] \end{aligned} \tag{2.73}$$

where $f$ is some function of $y$ and time $t$, the general idea it so split the time interval $[0,T]$ into $N$ sub-intervals of length $dt = T/N$, and propagate equation 2.73 one step forward at a time starting from the initial condition $y_0$. The RK4 algorithm evaluates the value of $y$ at time $t_{n+1}$ into different steps starting from the previous solution $y(t_n)$. In particular, the algorithm is implemented as follows

$$\begin{aligned} k_1 &= dt \times f(t_n, y(t_n)); \\ k_2 &= dt \times f(t_n + \frac{1}{2}dt, y(t_n) + \frac{1}{2}k_1); \\ k_3 &= dt \times f(t_n + \frac{1}{2}dt, y(t_n) + \frac{1}{2}k_2); \\ k_4 &= dt \times f(t_n + dt, y_n + k_3); \\ y(t_{n+1}) &= y(t_n) + \frac{1}{6}(k_1 + 2k_2 + 2k_3 + k_4) \end{aligned} \tag{2.74}$$

The local error of this algorithm is $o(dt^5)$, such that the global error is $o(dt^4)$. The method can be applied to the solution of equation 2.24, by rewriting it as

$$\frac{\partial \psi}{\partial t} = -\frac{i}{\hbar}\hat{H}\psi \tag{2.75}$$

where $\hat{H}$ is given in 2.25, and setting $f = -\frac{i}{\hbar}\hat{H}$.
Notice that RK4 is an explicit method, and hence it may become numerically unstable if the time step is not small enough. In all the simulations that lead to the results presented in this thesis, we have always checked that the simulation is stable by ensuring the conservation of the $L^2$ norm of the wave function as well as the energy of the system.

### 2.3.4 Non-local integrals and periodic boundary conditions

Solutions of the extended Gross-Pitaevskii equations 2.24 and 2.23 are complicated by the presence of the non-local integral term

$$\Phi_{dd}(\mathbf{r}) = \int d\mathbf{r}' V_{dd}(\mathbf{r}-\mathbf{r}')|\psi(\mathbf{r}')|^2 \tag{2.76}$$

Especially in three-dimensional calculations, evaluating this integral by numerical quadrature can be really expensive. However, taking the Fourier transform on both sides of equation 2.76, we find

$$\tilde{\Phi}_{dd}(\mathbf{k}) = \tilde{V}_{dd}(\mathbf{k})\tilde{\rho}(\mathbf{k}) \tag{2.77}$$

where $\rho(\mathbf{r}) = |\psi(\mathbf{r})|^2$ and the tilde denotes Fourier transform. We can see that, in Fourier space, the convolution integral $\Phi_{dd}$ is given by a simple multiplication. Moreover, the Fourier transform of the dipole-dipole interaction can be calculated analytically, and gives [35] (see also Appendix B)

$$V_{dd}(\mathbf{k}) = \frac{C_{dd}}{3}(3\cos^2\alpha - 1) \tag{2.78}$$

where $\alpha$ is the angle between $\mathbf{k}$ and the polarization axis $z$. We use this result to evaluate $\Phi_{dd}$ easily in three steps as

1. calculate the Fourier transform $\tilde{\rho}(\mathbf{k})$ of the density distribution $\rho(\mathbf{r}) = |\psi(\mathbf{r})|^2$;
2. calculate $\tilde{\Phi}_{dd}(\mathbf{k}) = \tilde{V}_{dd}(\mathbf{k})\tilde{\rho}(\mathbf{k})$;
3. calculate the inverse Fourier transform of $\tilde{\Phi}_{dd}(\mathbf{k})$, obtaining finally $\Phi_{dd}(\mathbf{r})$.

A similar procedure can be used to evaluate the action of the Laplace operator $\nabla^2$ on $\psi$, using the fact that the Fourier transform of $\nabla^2\psi(\mathbf{r})$ is equal to $-k^2\tilde{\psi}(\mathbf{k})$. Numerical evaluation of Fourier transforms can be done very efficiently both on multi-core CPUs using the FFTW3 package [55], and on GPUs using cuFFT [56]. Although it simplifies the evaluation of non-local integrals and derivatives, the use of Fourier transforms comes with a price. In fact, the use of Fourier transform imposes implicitly periodic boundary conditions, that may be un-physical, especially for a fully trapped system. Moreover, using a long-range potential, periodic boundary conditions introduce spurious interactions between the simulation cell and its periodic copies. These difficulties can be solved by employing a simulation cell large enough not only to accommodate the full spatial region in which the wave function $\psi$ is significantly different from zero, but also large enough so that the interaction between the simulation cell and its periodic copies is negligible. To ensure that these conditions are satisfied, different runs are always performed, using a larger and larger simulation cell, until we find that a further enlargement of the simulation cell (for fixed space-step) does not result in an appreciable change in either density profiles or energies.

# Chapter 3

# Supersolidity of a dipolar Bose gas confined in a ring

In this Chapter, we will use the methods described in the previous chapter to study the properties of a dipolar Bose gas confined in a "tubular" geometry, with the main axis orthogonal to the polarization direction of the dipoles, with periodic boundary conditions at the edges of the confinement, resembling the geometry of a ring. We will see that, under these conditions, the system can show supersolid behavior, and in particular a non-classical rotational inertia and an additional acoustic mode in the excitation spectrum. We will also study the density response of the system to external probes, applying the concepts of linear response theory presented in Chapter 2.

## 3.1 A roton in the excitation spectrum

The concept of a *roton* was introduced by Landau [57] in order to explain the thermodynamic properties of superfluid $^4$He. In particular, Landau postulated the existence of two kinds of low energy excitations in superfluid helium, which show in the energy-momentum dispersion relation $\hbar\omega(k)$: *phonons*, i.e. gapless excitations characterized by a linear dispersion relation in the limit $k \to 0$, and *rotons* (originally associated with elementary vortices), i.e. gapped excitations characterized by a parabolic dispersion relation with a local minimum at a finite momentum. This intuition was later confirmed in neutron scattering experiments [58]. The presence of a roton in the excitation spectrum has been associated with the tendency of the system to self-organize in a crystalline structure [59, 60, 22]. A roton minimum can also be found in the excitation spectrum of Bose-Einstein condensed systems interacting via long-range potentials, for example in the case of magnetic dipole-dipole interaction [61] or in BECs irradiated by off-resonant laser

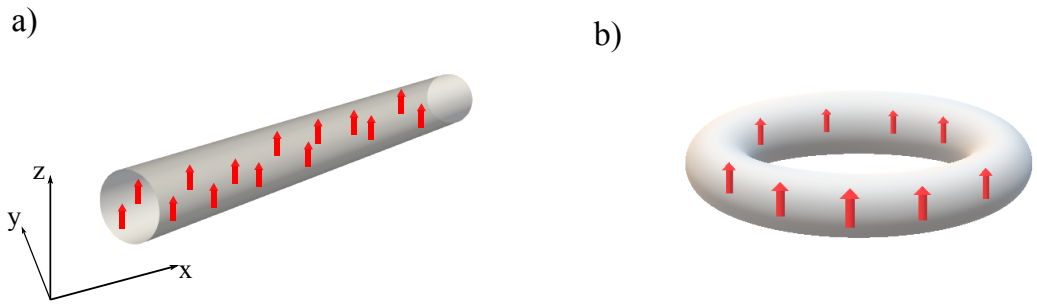


Figure 3.1: Schematic representation of the confining geometry. a) The dipoles are confined in a "tubular" confinement orthogonal to the polarization direction (z-axis), obtained with a harmonic trap in the y-z plane. b) Once periodic boundary conditions are set along x, the geometry resembles the one of a ring.

light [62]. The existence of the roton in such systems has been confirmed in recent experiments [63, 64].
As said, we now consider a dipolar BEC confined in a quasi-one-dimensional "tubular" geometry, obtained by confining the atoms in the y-z plane through a harmonic potential, but letting them free in the x direction. The dipoles are supposed to be aligned along the z axis by some external magnetic field. We consider the case in which periodic boundary conditions are imposed along the unconfined direction, in such a way that the resulting geometry is similar to the one of a ring (see figure 3.1). As shown in [65], the spectrum of the elementary excitations $\omega(k_x)$ of a homogeneous dipolar BEC confined in this geometry, and obtained by solving the Bogolyubov-de Gennes equations 2.16 with the quantum correction 2.25 for excitations propagating along the x axis, shows in fact a roton minimum at a finite value of the momentum. The typical shape of $\omega(k_x)$ is plotted in figure 3.2 panel (a). We can see that, for each value of $\varepsilon_{dd}$, the spectrum is linear and gapless for $k_x \to 0$, implying that long-wavelength fluctuations of the system are acoustic phonons. Moreover, for increasing $k_x$, the excitation spectrum continuously evolves from linear to parabolic, forming first a local maximum (called *maxon*) and then a roton minimum, with a roton gap that decreases as the strength of the dipolar interaction is further increased. For a certain critical value of $\varepsilon_{dd}$, the roton minimum touches the $k_x$ axis at the point $k_{rot}$, implying that the homogeneous BEC becomes unstable.

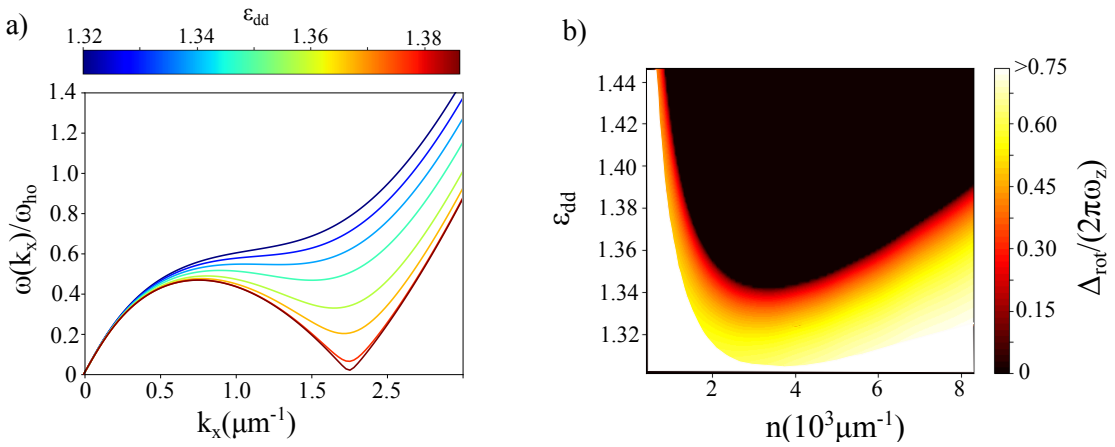


Figure 3.2: a) Excitation spectra of a homogeneous dipolar BEC of $N = 40000$ atoms of $^{164}$Dy, confined in a harmonic trap of frequencies $\omega_y = \omega_z = 2\pi(100)Hz$; along x, the system is unconfined, but subject to periodic boundary conditions at $x = \pm L$ with $L = 12\mu m$. b) For the same trapping geometry, energy of the roton as function of $\varepsilon_{dd}$ and of the linear density $n = N/L$. The black region corresponds to configurations in which a homogeneous superfluid is not stable, and the ground-state of the system is either a supersolid, or an array of independent droplets.

The value of the roton energy depends in a non-monotonic way on both the linear density $n = N/L$, where $N$ is the total number of atoms and $L$ the length of the tube, and $\varepsilon_{dd}$. For a fixed external trapping in the y-z plane, the stability region of the roton acquires a characteristic, asymmetric, inverse-bell shape. This implies that, for a fixed value of $\varepsilon_{dd}$, increasing the density starting from small values, the system first enters the instability region of the roton mode (black region of figure 3.2 panel (b) ), to come back to the stable region, characterized again by the occurrence of a roton with a finite excitation energy, at larger values of the density.

## 3.2 Spontaneous breaking of translational invariance

In the instability region of the roton mode, mean-field theory predicts that the system collapses. More specifically, numerical solutions of equation 2.12 are characterized by an un-physical density profile, with all the atoms settling at the same point of the simulation mesh. However, as previously discussed, in order to properly describe the dipolar BEC in the mean-field instability region, we need to take into account also beyond-mean-field effects. In particular, in order to study the

new ground state of the system, we need to consider numerical solutions of equation 2.23. As shown in figure 3.3, panels (c)-(d), when the roton mode makes the homogeneous superfluid unstable, the new ground state of the system is characterized by partially overlapping density peaks, whose relative distance is fixed by the critical value $k_{rot}$ of the momentum at which the roton minimum touches the $k_x$ axis via $\lambda = 2\pi/k_{rot}$. The system thus undergoes an equilibrium phase transition from a homogeneous superfluid to a state in which the density profile is periodically modulated. This state is called *supersolid*, and, as we will show in the next sections, shows properties of both a superfluid and a crystalline system. Moving away from the superfluid-supersolid phase transition by further increasing the value of $\varepsilon_{dd}$, the overlap between the density peaks becomes smaller and smaller, until each of them becomes an independent droplet (see figure 3.3 panels (e)-(f)). This state is also called *independent droplet crystal*. Notice that the density peaks in the supersolid and droplet crystal states are strongly elongated in the polarization direction (z-axis), as a consequence of the partially attractive nature of the dipole-dipole interaction.

For the choice of the physical parameters made in this chapter, the superfluid-supersolid phase transition is observed to be continuous, as expected for a system breaking translational invariance in one space dimension only [24]. In particular, the system develops the density modulation smoothly as the transition is crossed by increasing $\varepsilon_{dd}$. This was, however, not completely obvious, since a dipolar BEC in a ring-like geometry, despite the strong elongation along the x-axis, is not a purely one dimensional system, as transverse degrees of freedom are not frozen out due to the long range and anisotropic nature of the dipolar force. The consequence is that the superfluid-supersolid phase transition may be, in this configuration, either continuous or discontinuous (for example, in the case studied in [65], the transition was observed to be discontinuous), depending on the linear density $n = N/L$, where $N$ is the total number of atoms and $L$ the length of the simulation cell. In particular, Blakie et al. [66], using a simplified variational model in reduced dimensions, have found numerical evidences that a continuos transition characterizes a range of "intermidiate" densities between two critical values $n_{low}$ and $n_{high}$, which depend on the details of the trapping parameters and the atomic species used, while a discontinuous transition characterizes values of the density outside this range.

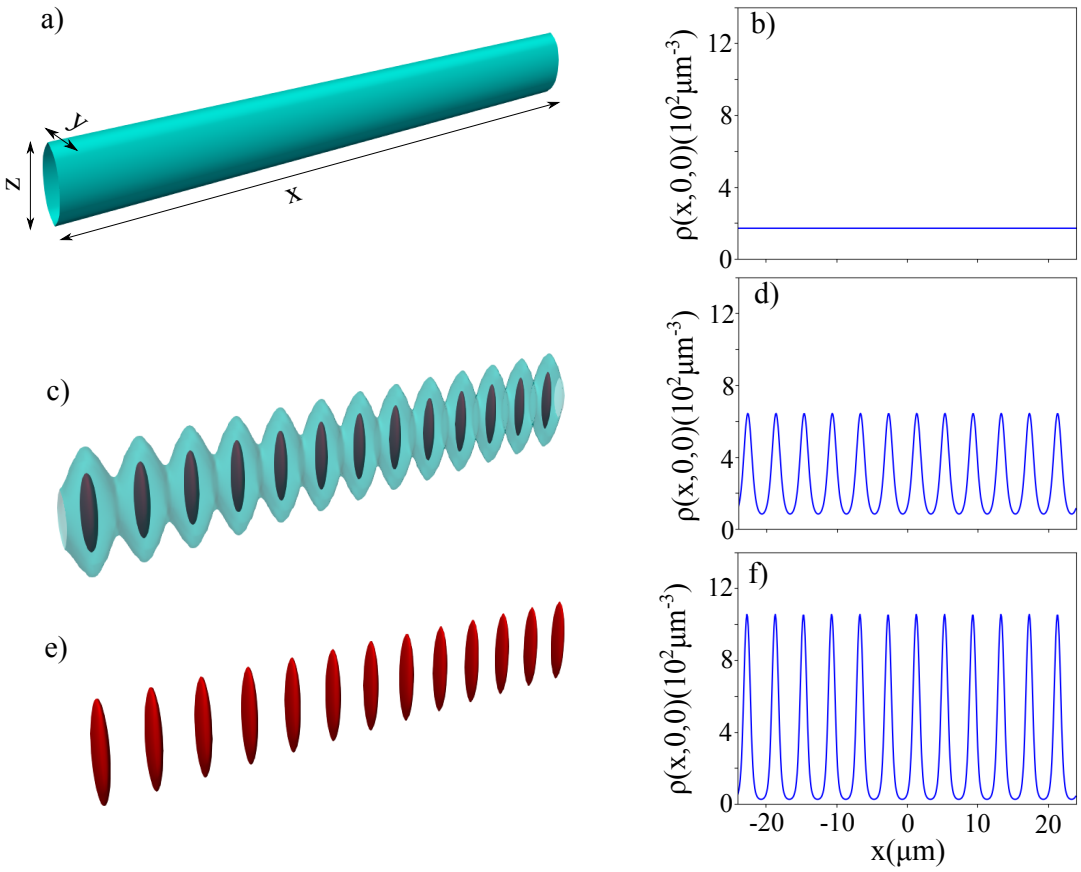


Figure 3.3: a,c,e) Iso-density contours of the ground state density profiles of a dipolar BEC of $N = 80000$ atoms of $^{164}$Dy confined by a harmonic potential of frequencies $\omega_{y,z} = 2\pi(100)Hz$ in the y-z plane, and unconfined along the x-direction. Along x, periodic boundary conditions are set at $x = \pm 24\mu m$. b,c,f) Corresponding density cuts along the x-axis.
Panels (a)-(b),(c)-(d) and (e)-(f) correspond, respectively, to $\varepsilon_{dd} = 1.2$ (homogeneous superfluid), $\varepsilon_{dd} = 1.39$ (supersolid) and 1.5 (independent droplets).

## 3.3 Non-Classical Rotational Inertia

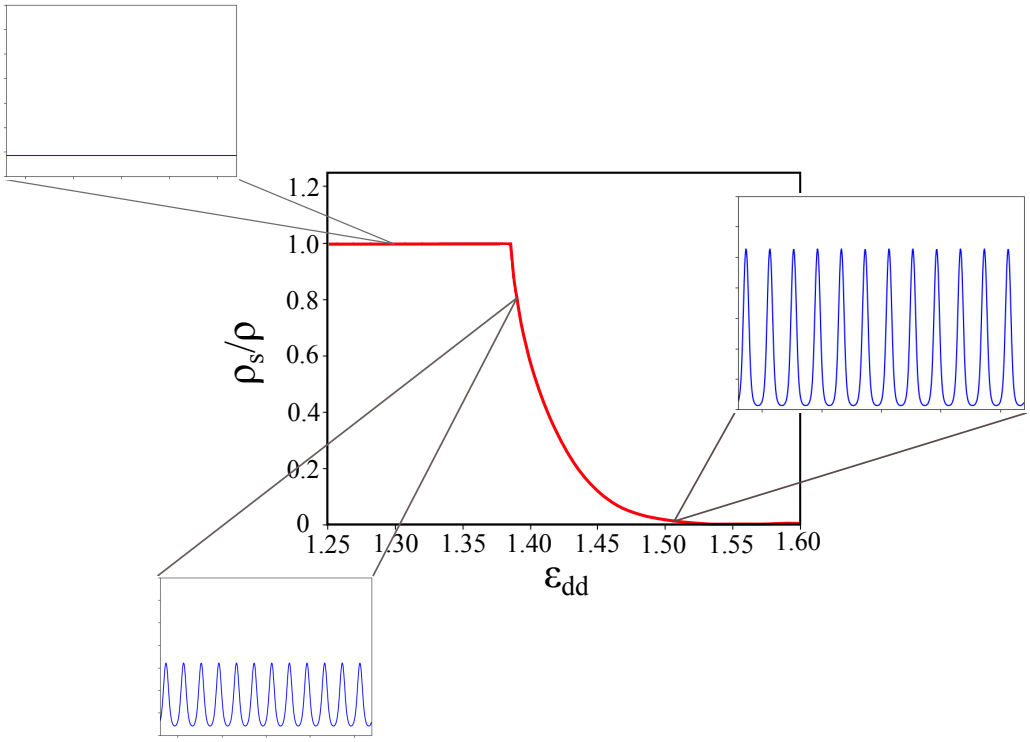


Figure 3.4: Superfluid fraction $\rho_s/\rho$, calculated according to 3.3, for a dipolar BEC of $N = 40000$ atoms of $^{164}$Dy, confined in a harmonic potential of frequencies $\omega_{y,z} = 2\pi(100)Hz$, and free in the x direction, along which periodic boundary conditions are set at $x = \pm 12\mu m$. The insets show the ground state density profiles along the x direction for different values of $\varepsilon_{dd}$ in the superfluid, supersolid and independent droplet phases.

One of the key manifestations of supersolidity is the appearance of a finite non-classical rotational inertia (NCRI). Simply speaking, the idea is that, given a system formed by two components, a superfluid and a non-superfluid one, the superfluid part is not dragged by any slow rotation of a (supposedly cylindrically symmetric) confining potential. This implies that any measurement of the moment of inertia will give a value smaller then the one of a classical system with the same mass distribution by an amount proportional to the superfluid fraction of the system. The idea of NCRI was first proposed by Leggett [14, 15] for a system of $N$ particles confined in a cylindrical annulus, slowly rotating around its axis. Minimizing the energy functional under the constraint of the single-valuedness of

the many-body wave function, Leggett found an upper bound for the superfluid fraction of the system. After "unrolling" the annulus along the x axis, fixing periodic boundary conditions, Leggett's upper bound on the superfluid fraction reads

$$\frac{\rho_s}{\rho} \leq \left\{ \int_0^L \frac{dx}{\int dydz\rho(x,y,z)} \right\}^{-1} \tag{3.1}$$

and is equal to 1 for a homogeneous system, smaller then 1 for a periodically modulated density distribution, and non-zero as long as there is some overlap between neighbouring density peaks.
The superfluid fraction associated with NCRI in a supersolid can also be estimated by starting from a Gross-Pitaevskii model with non-local interactions [24, 23]. In particular, the superfluid fraction of a system confined in a tubular geometry like the one considered here can be estimated by calculating the ground state expectation value of the momentum of the system in a frame (slowly) translating along the long axis of the tube (x-axis). Notice that, with the use of periodic boundary conditions, this is equivalent to a rotation of the ring around its axis. We thus calculate the solution of equation 2.23 with the addition of a momentum constraint

$$\mu\psi = \left( \hat{H} + i\hbar v_x \frac{\partial}{\partial x} \right) \psi \tag{3.2}$$

for a small translational velocity $v_x$, and define the superfluid fraction of the system as

$$\frac{\rho_s}{\rho} = 1 - \frac{\langle \hat{\mathbf{P}} \rangle}{N m v_x} \tag{3.3}$$

where $m$ is the atomic mass and $N$ the total number of particles. We have checked that the estimate 3.3 coincides with Leggett's estimate 3.1 in the geometry considered here, implying that Leggett's upper bound on the superfluid fraction, in this geometry, defines a rigorous equality.
The results for the superfluid fraction in the geometry considered here are shown in figure 3.4. We can see that the superfluid fraction associated with NCRI is equal to 1 for small values of $\varepsilon_{dd}$, where the ground state of the system is a superfluid homogeneous along the x-axis. As the system crosses the superfluid-supersolid phase transition, the superfluid fraction starts to rapidly decrease, and becomes null in the regime of independent droplets.

## 3.4 Excitation spectra

Another fundamental signature of supersolid behavior in $d$ space dimensions is the presence, in the excitation spectrum $\omega(k)$, of $d+1$ gapless phononic excitations,

linear in the limit of vanishing momenta. The existence of these excitations can be be seen as a consequence of Goldstone theorem, which associates one such excitation mode to each spontaneously broken continuous symmetry. In the case of a supersolid, the symmetries spontaneously broken are

1. continuous translational invariance in $d$ spatial directions, responsible for the emergence of a periodic, crystalline structure;

2. the gauge symmetry associated with Bose-Einstein condensation, responsible for superfluid phenomena.

As discussed in Chapter 1, the presence, in the excitation spectrum of a supersolid, of an additional gapless phononic excitation was originally proposed by Andreev and Lifshitz [10], in the context of a two-component model of supersolids in which a superfluid arising from Bose-Einstein condensation of defects is embedded in the crystal structure of the system. The more recent model based on a non-local Gross-Pitaevskii equation, developed Pomeau and Rica [22], also predicts the existence of the additional acoustic mode in a BEC that spontaneously breaks translational invariance.
In the case of a dipolar BEC in a ring geometry, in the supersolid phase, solving the Bogolyubov-de Gennes equations 2.16 with the LHY correction 2.25 for excitations propagating along the x-axis, we find, as expected, that the two lowest energy modes are gapless phononic excitations, as shown in figure 3.5 panels (h)-(i)-(j). Notice that, despite our system being three-dimensional, the continuous translational symmetry is broken along one spatial direction only, resulting in $1+1$ acoustic modes. Moreover, as expected for a periodic system, the excitation spectrum itself is also periodic, with a period fixed by the inverse of the lattice constant, the Brillouin wave vector being equal to the momentum $k_{rot}$ at which the roton minimum touches the zero-energy axis.

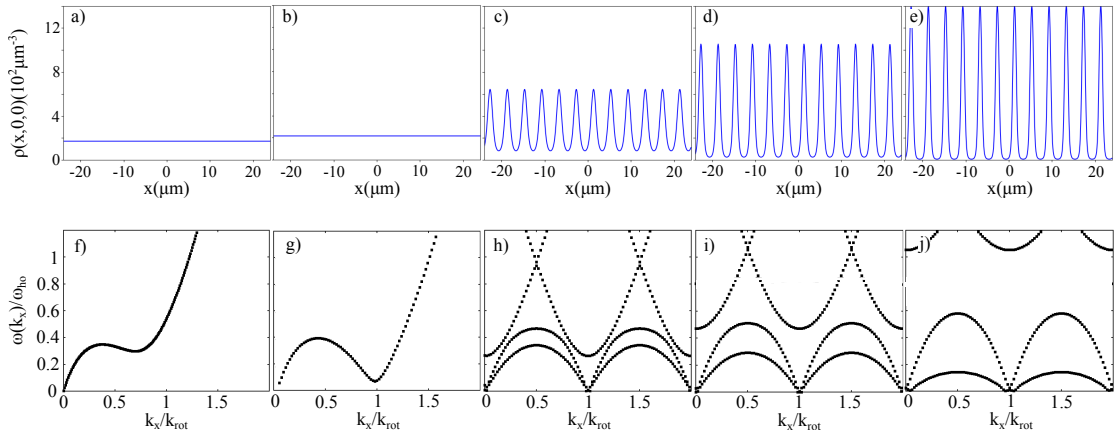


Figure 3.5: a-b) Ground state density profiles along x of a dipolar BEC of 80000 atoms of $^{164}$Dy, in the superfluid phase at $\varepsilon_{dd} = 1.2$ and $1,32$ (panels a-b), and in the supersolid phase at $\varepsilon_{dd} = 1.404$, $1.435$ and $1.466$ (panels c-d-e). The atoms are confined by a transverse harmonic trap of frequencies $\omega_{y,z} = 2\pi(100)Hz$, and free in the x-direction, where periodic boundary conditions are set at $x = \pm 24\mu m$. Panels f to h show the corresponding excitation spectra.

As we increase $\varepsilon_{dd}$ and the ground-state of the system evolves from a supersolid to an independent droplet crystal, the excitation spectrum evolves too. In fact, in the supersolid phase, for a value of $\varepsilon_{dd}$ close to the critical one for the superfluid-supersolid phase transition, the speed of sound is very similar in the two channels (figure 3.5 panel h); increasing $\varepsilon_{dd}$, instead, as the superfluid fraction decreases, the speed of sound associated with the lower energy Goldstone mode decreases too as the mode itself tends to disappears (figure 3.5 panels h-i-j). The speed of sound in the higher energy Goldstone mode tends instead to a constant value (figure 3.5 panels i-j). This is one of the key factors that support the interpretation of the lower energy Goldstone mode as the phase mode predicted in [23], and the higher energy one as an acoustic phonon of the crystal. Other evidences based on the study of the density and phase fluctuations associated with each mode (which, in the context of Bogolyubov theory, can be written respectively as $\delta\rho = (u + v^*)|\psi_0|$ and $\delta\phi = (u - v^*)/|\psi_0|$) are more difficult to interpret, since the two modes are always coupled.

## 3.5 Static and dynamic structure factor

Important insights on the excitation spectrum of the supersolid can be obtained by studying its linear response to a small density perturbation. In experiments, this procedure is also known as *Bragg scattering*. The basic idea of Bragg scattering

is to hit the system of interest with a certain probe (either neutrons in typical condensed matter applications, or photons in ultracold gases) generating a small perturbation potential, and then measure the energy and momentum transfer between sample and probe.
In the case of ultracold gases, scattering of photons generates a perturbation potential which can be written as [2]

$$\hat{H}_{Bragg} = V\left(\delta\hat{\rho}^{\dagger}_{\mathbf{k}}\mathrm{e}^{-i\omega t} + \delta\hat{\rho}_{\mathbf{k}}\mathrm{e}^{i\omega t}\right). \tag{3.4}$$

where $\delta\hat{\rho}_{\mathbf{k}} = \hat{\rho}_{\mathbf{k}} - <\hat{\rho}_{\mathbf{k}}>$, $\hat{\rho}_{\mathbf{k}}$ being the Fourier transform of the density operator at momentum $\mathbf{k}$, and $V$ is the strength of the perturbation. If this is small enough, informations on the linear response of the system are contained in the *dynamic structure factor*, which, as we have seen, at zero temperature is defined as

$$S(\mathbf{k},\omega) = \sum_{n} |\langle n|\delta\hat{\rho}^{\dagger}_{\mathbf{k}}|0\rangle|^2 \delta(\hbar\omega - \hbar\omega_n) \tag{3.5}$$

where $|n\rangle$ is an excited state of the system with energy $\hbar\omega_n$. The dynamic structure factor allows to calculate the probability that the probe transfers an energy $\hbar\omega$ and a momentum $\hbar\mathbf{k}$ to the system via the simple relation

$$P(\mathbf{k},\omega) = 2\pi|V|^2 S(\mathbf{k},\omega) \tag{3.6}$$

If the elementary excitations of the system are studied in the context of Bogolyubov theory, the dynamic structure factor can be written as

$$S(\mathbf{k},\omega) = \sum_{n} \left| \int d\mathbf{r}[u^*_n(\mathbf{r}) + v^*_n(\mathbf{r})]\psi(\mathbf{r})\mathrm{e}^{i\mathbf{k}\cdot\mathbf{r}} \right|^2 \times \delta(\omega_n - \omega) \tag{3.7}$$

Figure 3.6 shows the same excitation spectra as in figure 3.5, with each mode colored according to its contribution $|\langle n|\delta\hat{\rho}^{\dagger}_{\mathbf{k}}|0\rangle|^2$ to the dynamic structure factor.
In the superfluid phase (figure 3.6 panels a and b ), the response of the system to a density perturbation is maximal at the momentum and energy of the roton. This behavior becomes more evident as the superfluid-supersolid phase transition is approached by increasing $\varepsilon_{dd}$.

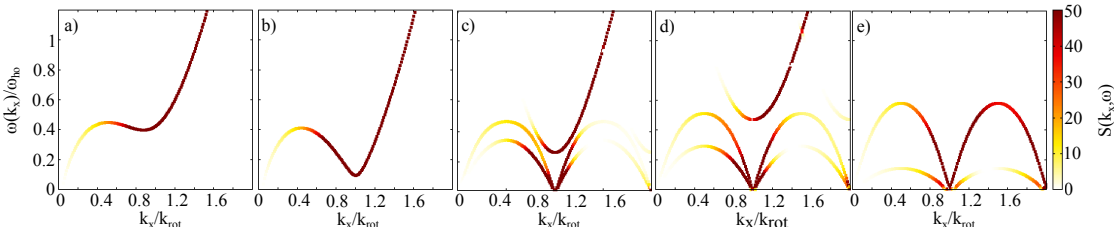


Figure 3.6: Same excitation spectra as in figure 3.5, with each mode colored according to the value of $|\langle n|\delta\hat{\rho}^\dagger_{\mathbf{k}}|0\rangle|^2$, i.e. the contribution to the dynamic structure factor.

In the supersolid phase (figure 3.6 panels c and d), different modes show up in the dynamic structure factor. The system is more sensitive to perturbations with the momentum of the Brillouin wave vector of the periodic density profile, which, close to the transition, is fixed by the roton. In these conditions, where the overlap between density peaks is large and the superfluid fraction is still close to 1, the stronger density response comes from the lower-energy Goldstone mode (figure 3.6 panel c); a strong density response is also associated with the parabolic branch above the two Goldstone modes, especially at large momenta beyond the first Brillouin zone. The situation is different when we go deeper in the supersolid regime by increasing $\varepsilon_{dd}$ (figure 3.6 panels d-e). In these conditions, in fact, the overlap between the density peaks becomes smaller, as the superfluid fraction tends to zero. The relative strength of the higher- and lower-energy Goldstone mode tends to move in favour of the former: as the superfluid fraction decreases, the response of the lower energy mode decreases, until the mode itself disappears from the spectrum. Notice also that the contribution to the dynamic structure factor coming from the parabolic branch above the two Goldstone modes tends to disappear when the system approaches the independent droplet regime.
Further insight on the excitation spectrum of the supersolid comes from the behavior of the *static structure factor*, in particular near the Brillouin wave vector. Remind that the static structure factor is defined as

$$S(\mathbf{k}) = \frac{1}{N}\sum_n |\langle n|\delta\hat{\rho}^\dagger_{\mathbf{k}}|0\rangle|^2 \tag{3.8}$$

where $N$ is the total number of particles.

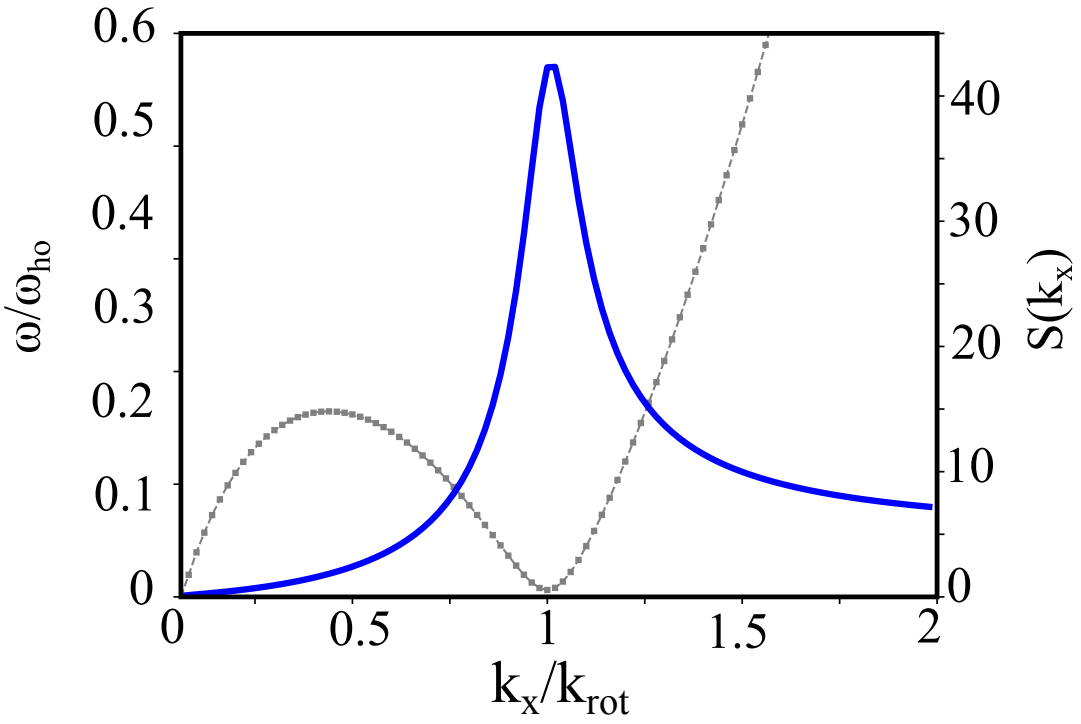


Figure 3.7: Static structure factor (blue solid line) of a dipolar BEC of 80000 atoms of $^{164}$Dy confined in a tubular geometry with periodic boundary conditions, obtained with a harmonic trap of frequencies $2\pi(100)$Hz in the y-z plane and setting periodic boundary conditions along the x-axis at $x = \pm 24\mu m$, in the homogenous phase at $\varepsilon_{dd} = 1.2$. We also report the first Bogolyubov mode (grey dashed line) and the Feynman relation $\omega(k) = \hbar^2 k^2 / 2S(k)$ (grey dots), which in this case coincides exactly.

In the superfluid phase (figure 3.7), the static structure factor is strongly peaked at the momentum of the roton. In this case, the Feynman relation 2.54 holds exactly, so that the single-mode approximation is perfectly fulfilled, and a single branch exhaust the entire density response of the system.

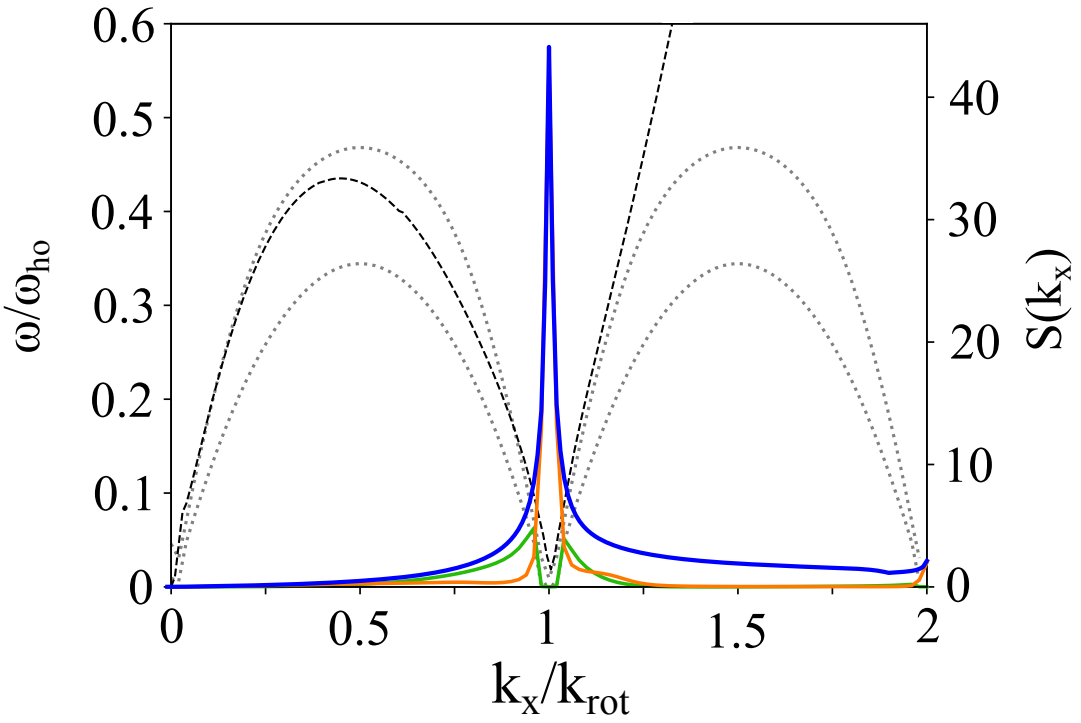


Figure 3.8: Static structure factor (blue solid line) of a dipolar BEC of 80000 atoms of $^{164}$Dy confined in a tubular geometry with periodic boundary conditions, obtained with a harmonic trap of frequencies $2\pi(100)$Hz in the y-z plane and setting periodic boundary conditions along the x-axis at $x = \pm 24\mu m$, in the supersolid phase at $\varepsilon_{dd} = 1.39$. We also report the first two Goldstone modes (grey dotted lines), their contributions to the static structure factor (respectively, green and orange solid lines), and the Feynman relation $\omega(k) = \hbar^2 k^2 / 2S(k)$ (black dashed line). Notice that this coincides with the higher energy Goldstone mode both at small momenta and close to the Brillouin wave vector.

The scenario is completely different in the supersolid phase (figure 3.8). As we have already seen, in this case different modes have an appreciable density response, as shown in the dynamic structure factor (figure 3.6 panels (b)-(c)). This can be seen better by looking at the contributions to the static structure factor from the different branches and at different momenta (figure 3.8). At small momenta, the static structure factor (blue solid line) takes contributions mainly from the lower energy Goldstone mode (green solid line). Close to the Brillouin wave vector, instead, this contribution goes to zero, while the contribution from the higher energy Goldstone mode (orange solid line) tends to diverge and determines

the static structure factor completely. Beyond the Brillouin zone, other modes contribute appreciably to the static structure factor. The divergence of the contribution to the static structure factor of the higher energy Goldstone mode is one of the strongest evidences of its crystal character, and can be rigorously proved using linear response theory and the sum-rules formalism [67].

## 3.6 Single-particle excitations

For a homogeneous system, the zero-temperature behavior of the dynamic structure factor at large momenta becomes sensitive to single-particle excitations only. In the case of a non-dipolar BEC, in this regime (which occurs above a wave number of the order of $\xi^{-1}$, where $\xi = \hbar/\sqrt{2mgn}$ is the healing length) the excitation spectrum of the system becomes parabolic, being given by the free-particle expression $\omega(\mathbf{k}) = \hbar^2 k^2/2m$, and the dynamic structure factor is determined by the momentum distribution $\tilde{n}(\mathbf{p})$ according to

$$S(\mathbf{k},\omega) \simeq \int d\mathbf{p}\tilde{n}(\mathbf{p})\delta\left(\omega - \frac{(\mathbf{p}+\hbar\mathbf{k})^2}{2m} + \frac{\mathbf{p}^2}{2m}\right) \tag{3.9}$$

This result is known as *impulse approximation* [2]. Moreover, the Bogolyubov quasi-particle amplitudes $u$ and $v$, solution of the Bogolyubov-de Gennes equations 2.16, in this regime, become approximately equal to 1 and 0 respectively.
In the case of a dipolar BEC, the distinction between collective and single-particle excitations becomes less easy, and not clearly relatable to a particular length scale of the system, especially in the supersolid phase. Following [2], we can identify the single particle modes by requiring $v \simeq 0$. For these modes, given the normalization condition 2.18, we have $||u|| = \int d\mathbf{r}|u(r)|^2 \simeq 1$. In figure 3.9 panels (a)-(b), we report the excitation spectrum of a homogeneous dipolar BEC in the ring trap, colored according to the norm of $u$. We can see that long-wavelength excitations have always a collective character, while the roton tend to assume a collective character only when the roton gap is close to zero (figure 3.9 panel b). Moreover, we find that the transition from the collective to the single particle character in the dipolar case occurs at momenta much smaller then the inverse healing length. In the supersolid phase, the excitation spectrum is more structured, as we have seen in figure 3.5. In fact, the spectrum is periodic, with a period fixed by the Brillouin wave vector, and at low energy is characterized by the occurrence of the two Goldstone modes, which, as shown in figure 3.9 panels (c)-(d)-(e), have (mainly) a collective character. Instead, the parabolic branches above the two Goldstone modes, which as we have seen give important contributions to the dynamic structure factor especially beyond the first Brillouin zone, have a clear single-particle character, and reminds the excitation branches of free particles in a periodic lattice.

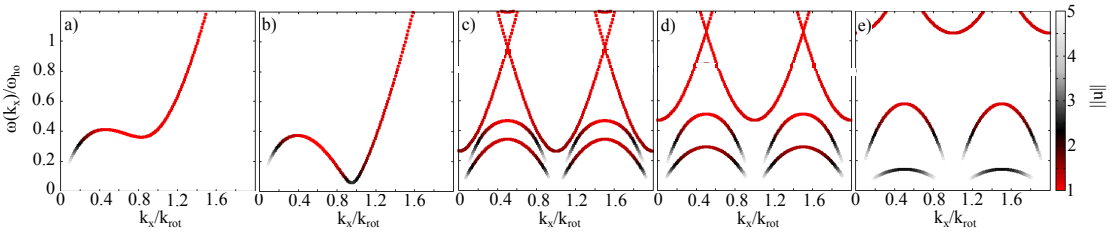


Figure 3.9: Same excitation spectra as in figure 3.5, with each mode colored according to the value of $||u||$. Modes colored in red have a prominently single-particle character, while the others have a more collective character.

Along the free particle branches, the dynamic structure factor is sensitive to the momentum distribution of the system also in the supersolid phase [68]. First experimental measurements [69] have shown that, in this regime, the presence of density modulations in the supersolid phase, as well as the loss of phase coherence among the density peaks in the independent droplet regime, produce a strong suppression of the dynamic structure factor. This suppression is faster in the experiment compared to the theory, suggesting that out-of-equilibrium phase dynamics affects the response of the system to external perturbations.

# Chapter 4

# Compressional oscillations and scissors mode

In the previous chapter, we have studied several aspects related to the supersolid behavior of a dipolar Bose gas confined in a tubular trap with periodic boundary conditions, resembling the geometry of a ring. In current experiments, however, the realization of ring-shaped harmonic traps is not trivial, and of course periodic boundary conditions cannot be set in the real world. For these reasons, most of the experimental studies on the supersolid behavior of a dipolar Bose gas have been done in a three-dimensional, strongly elongated, cigar-shaped harmonic trap, with the long axis orthogonal to the polarization direction of the dipoles. Nonethless, evidences of supersolid-like behavior have been observed in this configuration. This chapter describes such evidences with a particular focus on comparisons between theory and experiments.

## 4.1 Ground-state density profiles

Soon after the first proposal of the possible existence of a supersolid phase in a dipolar BEC confined in a ring geometry [65], evidences of supersolid behavior have been revealed in three different experiments, respectively in Pisa [31], Innsbruck [33] and Stuttgart [32] in a dipolar BEC confined in a cigar-shaped harmonic trap. The typical trapping configuration is shown in figure 4.1, and is characterized by a strong harmonic confinement along the polarization direction (z-axis) and one of the orthogonal directions (y-axis). Along the x-axis, since periodic boundary conditions cannot be set in a real experiment, a weak harmonic confinement is imposed.

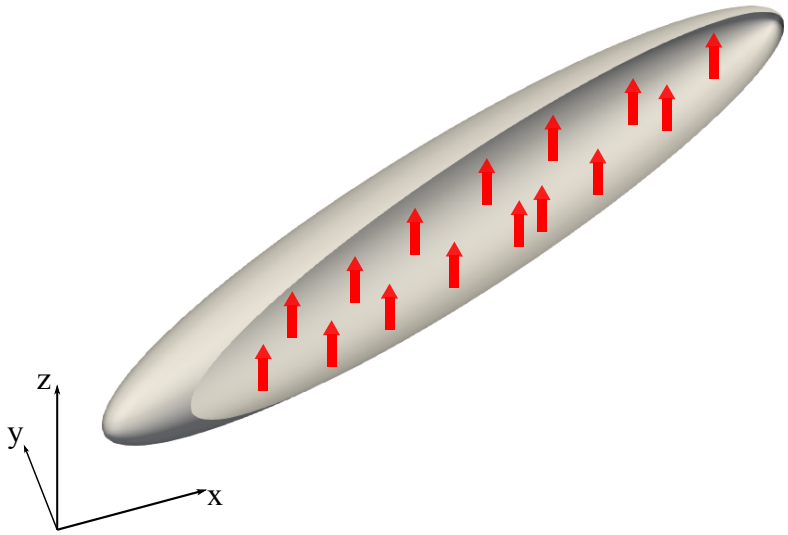


Figure 4.1: Schematic representation of a dipolar Bose gas confined in a cigar-shaped harmonic trap. The dipoles are supposed to be aligned along the z-axis by some external magnetic field. A strong harmonic potential is imposed along both the polarization direction and one of the orthogonal directions (y-axis), while a weak harmonic confinement is set along the x-axis.

Also in the case of axial harmonic trapping, the ground-state density profiles are deeply affected by the value of the parameter $\varepsilon_{dd}$. When $\varepsilon_{dd}$ is small enough, the density profiles assume, along the three axis, the characteristic shape of an inverted parabola that defines the Thomas-Fermi regime [2, 47] (figure 4.2 panel a). For increasing $\varepsilon_{dd}$, instead, the ground-state density profile along the x-axis is characterized by the emergence of equally spaced density peaks, (figure 4.2 panel b), showing a finite overlap which tends to zero as $\varepsilon_{dd}$ is increased (figure 4.2 panels c and d). We thus find that, also in the cigar-shaped harmonic trap, we can distinguish three phases, analogously to what we have seen in the ring trap: a *superfluid* phase, characterized by a Thomas-Fermi density profile along the x-axis, a *supersolid* phase, characterized by partially overlapping density peaks along the x-axis, and an *independent droplet* phase, in which the density peaks are well separated.

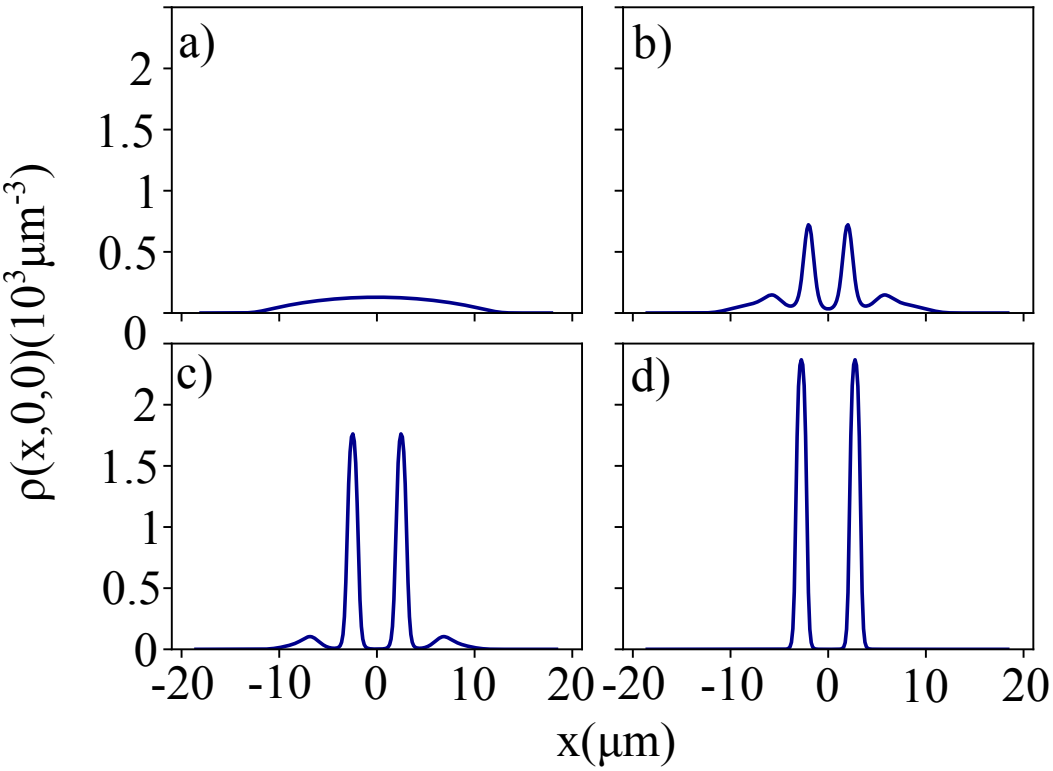


Figure 4.2: Density profiles along the x-axis of a dipolar BEC of 35000 atoms of $^{164}$Dy, confined in a harmonic trap of frequencies $\omega_{x,y,z} = 2\pi(18.5, 53, 81)Hz$ and different values of $\varepsilon_{dd}$. a) Superfluid phase, $\varepsilon_{dd} = 1.32$. b) Supersolid phase, $\varepsilon_{dd} = 1.40$. c) Supersolid phase, $\varepsilon_{dd} = 1.5$. d) Independent droplet phase, $\varepsilon_{dd} = 1.55$.

Some care must be taken when using these analogies, in particular for what concern the "supersolid" and the "droplet crystal" phases. In fact, in current experiments it is possible to create supersolid samples with only a few lattice sites (typically between two and five, and, at the time of writing, always less then ten), far from the thermodynamic limit in which theories are typically developed. Experimentally, the supersolid phase in this context is defined as a phase which spontaneously develops a density modulation along the x-axis, but also *keeps global phase coherence*. What experiments have shown, in fact, is that these two features appears only in a small interval of $\varepsilon_{dd}$, identifying the supersolid phase. In the superfluid (small values of $\varepsilon_{dd}$), phase coherence can be detected, but no evidences of density modulations are present, while the opposite is true in the independent droplet regime (high values of $\varepsilon_{dd}$), with the appearance of localized density peaks and the loss of global phase coherence. Moreover, the (relatively) high densities

reached by the density peaks enhance inelastic three-body losses, reducing the lifetime of the experimentally available samples to (currently) few hundreds of milliseconds.
The coexistence of density modulations and global phase coherence is only a partially satisfactory definition of a supersolid: we miss, in fact, the two fundamental signatures of supersolid behavior, namely the appearance of coupled excitation modes for the superfluid and the lattice, which in the tubular geometry with periodic boundary conditions shows up in the two Goldstone modes, and evidences of non-classical rotational inertia. We will now discuss how such evidences can be found in a trapped configuration.

## 4.2 Bifurcation of compressional oscillations

As stated previously, one of the fundamental signatures of supersolid behavior is the appearance of two separate sound modes, associated respectively with a lattice mode (crystal phonon) and a phase mode (superfluid phonon). Unfortunately, the supersolid samples confined in cigar-shaped harmonic traps currently available in experiments are much smaller then the typical inverse wavelength of the system phonons. This is particularly evident for the crystal phonon, which cannot even be defined in presence of just two or three lattice sites. However, we can still learn something on the supersolid properties of this system by looking at the behavior of its low-energy *compressional oscillations* [70].
We study the compressional oscillations along the x-axis of our dipolar BEC confined in a cigar-shaped trap, using mainly numerical simulations based on the solution of equations 2.23 and 2.24. We consider a system formed by 35000 atoms of $^{164}$Dy confined in a harmonic trap of frequencies $\omega_{x,y,z} = 2\pi(18.5, 53, 81)$Hz. We excite axial compressional oscillations by first calculating the ground-state configuration of the system, solving equation 2.23, in presence of a small perturbation of the form $\hat{H}_{pert} = -\lambda\hat{x}^2$, and then evolving the system in real time using equation 2.24 after switching off the perturbation. This is equivalent to slightly compressing the system along the x-axis and then let it oscillate freely (see figure 4.3 panel a). We monitor the time-evolution of the second moment $\langle\hat{x}^2\rangle = \int d\mathbf{r}x^2|\psi(\mathbf{r},t)|^2$ of the in-trap density distribution, whose typical behavior is reported in figure 4.3.

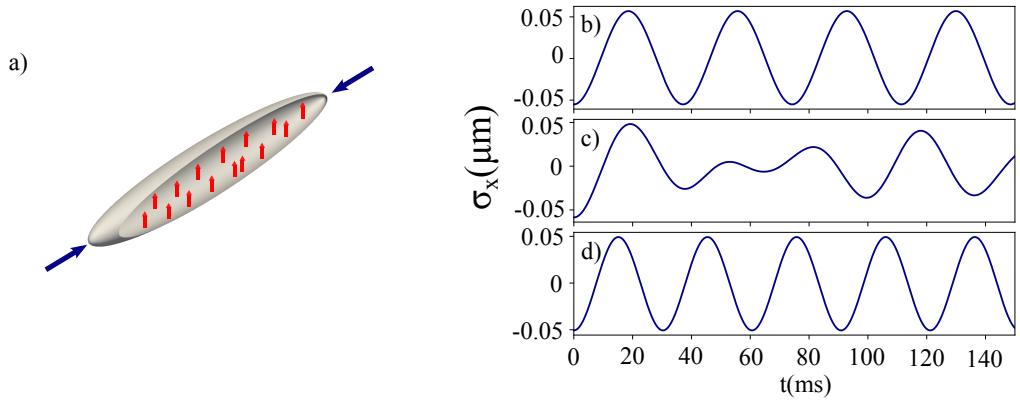


Figure 4.3: a) Schematics of the excitation procedure of the axial compressional oscillation: imposing the perturbation $\hat{x}^2$ is equivalent to a slight compression of the system along the x-axis. b,c,d) Time dependence of $\sigma_x = f(t) - \bar{f}(t)$, where $\bar{f}(t)$ is the temporal average of the signal $f(t) = \sqrt{\langle \hat{x}^2(t) \rangle}$, and $\langle \hat{x}^2(t) \rangle = \int d\mathbf{r} x^2 |\psi(\mathbf{r}, t)|^2$, in the superfluid (panel b, $\varepsilon_{dd} = 1.30$), supersolid (panel c, $\varepsilon_{dd} = 1.38$) and independent droplet regimes (panel d, $\varepsilon_{dd} = 1.52$). Here, $\psi(\mathbf{r}, t)$ is the condensate wave function of a dipolar BEC of 35000 atoms of $^{164}$Dy in a harmonic trap of frequencies $\omega_{x,y,z} = 2\pi(18.5, 53, 81)$Hz, obtained from the solution of equation 2.24, using as initial condition the ground state of the system in presence of a small perturbation of the form $\hat{H}_{pert} = -\lambda \hat{x}^2$.

In the superfluid phase (figure 4.3 panel b), the time-dependence of the observable $\langle \hat{x}^2 \rangle$ is characterized by a simple harmonic oscillation with a clearly identifiable frequency. In absence of dipolar interaction, this frequency can be calculated analytically at the mean-field level, by solving the hydrodynamic equations of superfluids [71], yielding the interaction-independent result $\omega = \sqrt{5/2}\omega_x$, in excellent agreement with experimental observations [72]. In presence of dipole-dipole interactions, instead, the frequency of this mode is predicted to slowly decrease with $\varepsilon_{dd}$ [47] as the mean-field unstable region is approached. This result actually extends also in the mean-field unstable region of the superfluid phase, where the system is stabilized by quantum fluctuations. In both these cases, a simple estimate of the frequency of the axial compressional oscillation can be obtained by a sum-rule approach, considering the ratio between the energy weighted $m_1 = \int d\omega \omega S(\hat{x}^2, \omega)$ and the inverse energy weighted moment $m_{-1} = \int d\omega \omega^{-1} S(\hat{x}^2, \omega)$ of the dynamic structure factor $S(\hat{x}^2, \omega) = \sum_n |\langle n|\hat{x}^2|0\rangle|^2 \delta(\omega - \omega_n)$ relative to the perturbation operator $\hat{x}^2$. This ratio provides in fact a rigorous upper bound on the frequency of the lowest energy mode excited by $\hat{x}^2$ [73] for any system of particles interacting through a potential depending only on the relative position of the atoms. Consider

in fact a general many-body hamiltonian of the form

$$\hat{H} = \sum_{i=1}^{N} \left( \frac{\hat{P}_i^2}{2m} + V_{ext}(\hat{\mathbf{r}}_i) \right) + \sum_{i \neq j} V(\hat{\mathbf{r}}_i - \hat{\mathbf{r}}_j) \tag{4.1}$$

where $N$ is the total number of particles in the system. Considering a perturbation operator of the form $\hat{H}_{pert} = -\lambda \hat{F}$, with $\hat{F} = \hat{x}^2$, the sum rules 2.37 allow to calculate the energy weighted moment $m_1$ as

$$m_1 = \frac{1}{2} \left[ \hat{x}^2, \left[ \hat{H}, \hat{x}^2 \right] \right] = \frac{2N\hbar^2}{m} \langle \hat{x}^2 \rangle \tag{4.2}$$

The inverse energy-weighted moment $m_{-1}$ is instead related to the static response function $\chi$ via the relation $m_{-1} = \frac{1}{2}\chi$. In turn, the static response function can be calculated by considering the fluctuation induced on the operator $\hat{x}^2$ by the perturbation considered via $\chi = -\frac{N}{\lambda}\delta\langle \hat{x}^2 \rangle$. Finally, noticing that, in case of harmonic trapping, the perturbation $\lambda \hat{x}^2$ is equivalent to a shift in the harmonic confinement along x equal to $\delta\omega_x = -\frac{\lambda}{m\omega_x}$, we find the following upper bound on the frequency of the axial compressional oscillation

$$\hbar^2\omega^2 = \frac{m_1}{m_{-1}} = -2\hbar^2 \frac{\langle \hat{x}^2 \rangle}{\frac{d\langle \hat{x}^2 \rangle}{d\omega_x^2}} \tag{4.3}$$

Notice that here, $\langle \hat{x}^2 \rangle$ is the *equilibrium* expectation value of $\hat{x}^2$. As shown in figure 4.4 (green stars), this estimate matches well the results obtained via real-time simulations in the superfluid regime.

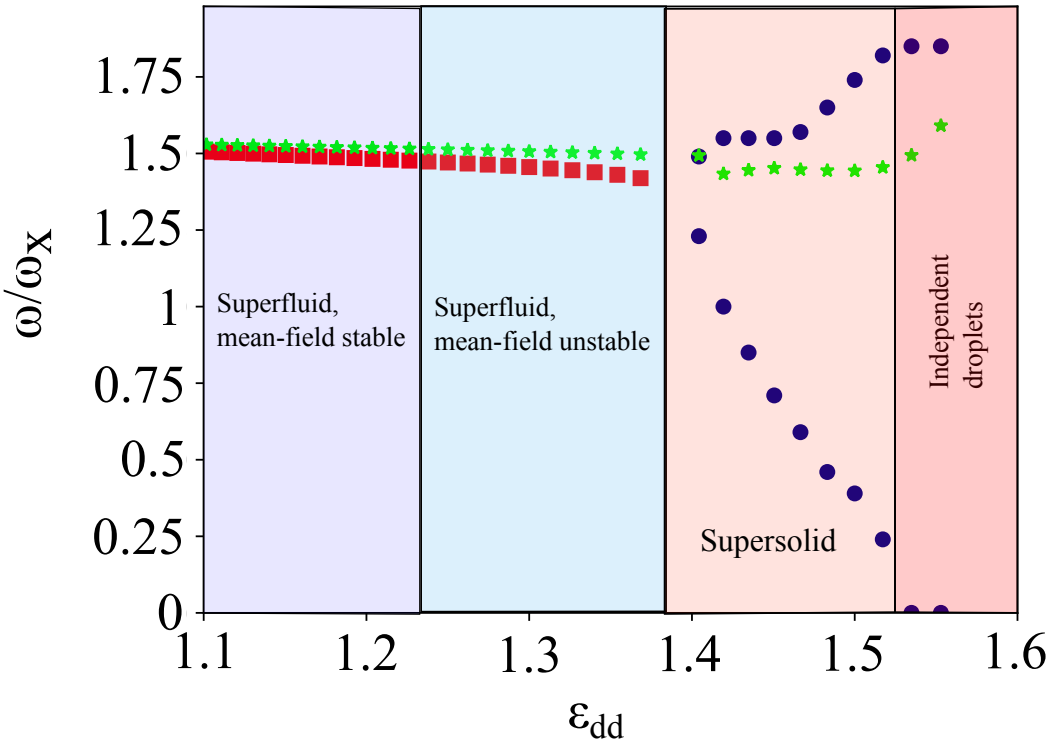


Figure 4.4: Frequencies of the axial compressional oscillations as function of $\varepsilon_{dd}$, in the superfluid (red squares), supersolid and independent droplet phases (blue circles). Green stars represent the sum-rule estimate 4.3.

At a certain critical value of $\varepsilon_{dd}$, the system develops a density modulation along the x-axis, entering in the supersolid phase (figure 4.2 panel b). The temporal evolution of the observable $\langle \hat{x}^2 \rangle$ is now characterized by the beating of modes with different frequencies (see figure 4.3 panel c). A simple Fourier analysis of the signal shows that the main contributions to the beating come from two modes only. This allows to fit the signal using a double sine function of the form $A_1 \sin(\omega_1 t + \phi_1) + A_2 \sin(\omega_2 t + \phi_2)$, and to extract the frequencies $\omega_1$ and $\omega_2$ of the two modes as function of $\varepsilon_{dd}$. The result of this procedure is shown in figure 4.4. We can see that the axial compressional oscillation bifurcates into two modes of different frequency at the superfluid-supersolid phase transition. The frequency associated with the lower energy mode tends to decrease until vanishing when moving from the supersolid to the independent droplet regime, while the frequency associated with the higher energy mode tends to increase until it reaches an approximately constant value. This behavior is specular to the one of the two

Goldstone modes in the ring geometry, where, as we have seen, the lower energy mode tends to disappear at supersolid-independent droplet transition, while the higher energy mode tends to become a phononic mode with a fixed speed of sound. We are thus led to identify the lower energy mode as a "phase" mode, associated with the global phase coherence of the system, that can exist only as long as the density peaks show some finite overlap and atoms can tunnel between them, while the higher energy mode, which survives also in the independent droplet regime, is interpreted as a lattice mode. Notice that, in this regime, the sum-rule estimate 4.3 gives a value in between the two frequencies, implying that the single-mode approximation is no longer valid.
In the independent droplet phase, the time dependence of $\langle \hat{x}^2 \rangle$ is again characterized by a simple harmonic oscillation (figure 4.3 panel d), as only the higher energy compressional oscillation survives (figure 4.4). The axial mode excited by the perturbation operator $\hat{x}^2$ is now just an out-of-phase harmonic oscillation of the two droplets around their equilibrium positions, without any significant deformation of their density profile. The frequency of this oscillation can be estimated using classical arguments, treating the two droplets as classical distributions of dipoles. More specifically, neglecting the internal structure of the droplets, we can write an energy functional for the system as

$$E[n_1, n_2] = E_{dd}[n_1, n_2] + E_{trap}[n_1] + E_{trap}[n_2] \tag{4.4}$$

where $n_1(\mathbf{r})$ and $n_2(\mathbf{r})$ are the ground-state density profiles of the two droplets obtained by numerical solutions of equation 2.23, while

$$E_{dd}[n_1, n_2] = \int d\mathbf{r}_1 d\mathbf{r}_2 V_{dd}(\mathbf{r}_1 - \mathbf{r}_2) n_1(\mathbf{r}_1) n_2(\mathbf{r}_2) \tag{4.5}$$

is the dipole-dipole interaction energy of the two droplets, and

$$E_{trap}[n] = \int d\mathbf{r} V_{trap}(\mathbf{r}) n(\mathbf{r}) \tag{4.6}$$

is the energy term due to the trapping potential. Considering the variation of the energy functional for a small displacement along the x-axis of the center-of-mass of the two droplets, one finds that the frequency of the out-of-phase oscillation is given by [74]

$$\omega = \omega_x \sqrt{1 - \frac{2}{N m \omega_x^2} \int d\mathbf{r}_1 d\mathbf{r}_2 V_{dd}(\mathbf{r}_1 - \mathbf{r}_2) \frac{\partial n_1(\mathbf{r}_1)}{\partial x_1} \frac{\partial n_2(\mathbf{r}_2)}{\partial x_2}} \tag{4.7}$$

Finally, evaluating this integral numerically for $\varepsilon_{dd} = 1.52$, deeply in the independent droplet regime (see figures 4.3 and 4.4), we find the value $\omega = 1.95\omega_x$, very close to the value $\omega \simeq 1.85\omega_x$ found by our real-time simulations based on the full solution of equation 2.24.

### 4.2.1 Comparison with experiments

The results presented in the previous section have been compared with experiments performed in Pisa [70]. The excitation protocol used in the experiments was different from the one studied theoretically in the previous section. Moreover, since in-situ images were not available in that experiment, all observations have been done on the momentum distribution, and the fundamental time-dependent observable was the squared average momentum along the x-axis $\langle k_x^2 \rangle$. Nonetheless, evidences of the bifurcation of compressional oscillations at the superfluid-supersolid phase transition have been found.

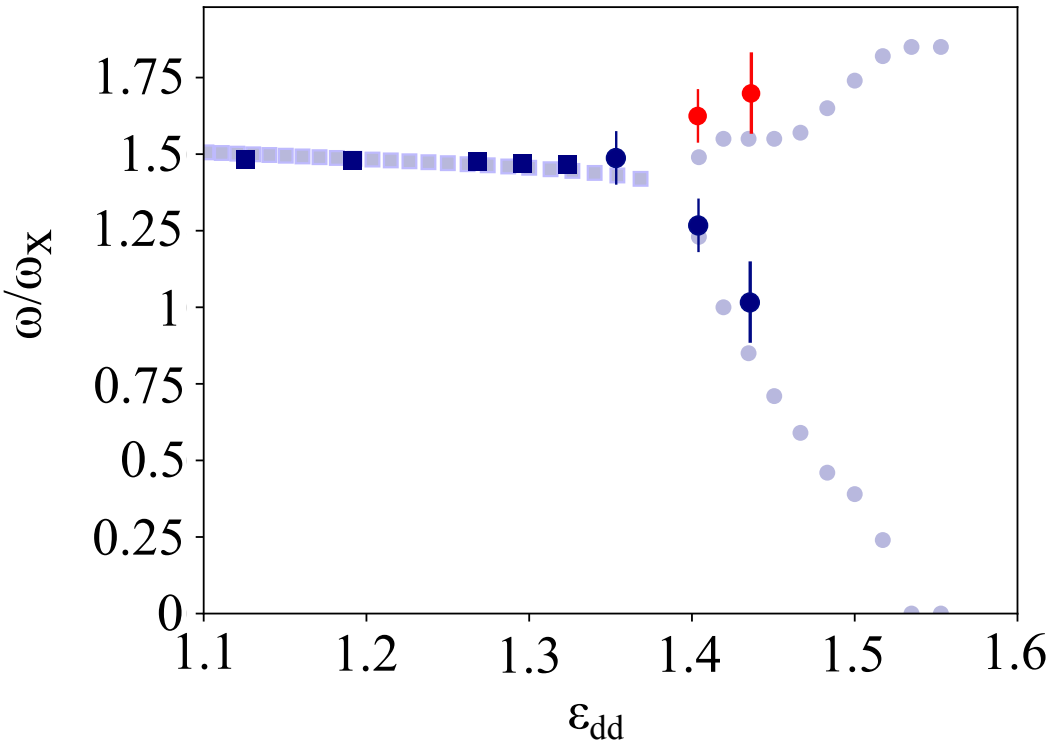


Figure 4.5: Bifurcation of the axial compressional oscillation as seen in the experiment [70]. Blue squares represents the data relative to the superfluid phase. Circles represents data relative to the supersolid phase: blue ones are those associated with the lattice depth (phase modes), while red ones are those associated with lattice spacing (crystal modes). The light blue squares and circles are the theoretical data reported in figure 4.4.

In particular, in the experiments, the initial state of the system was the super-

fluid phase, from which the supersolid regime is reached by increasing $\varepsilon_{dd}$, which, in the experiment, can be done by changing the scattering length $a_s$ through a Feschbach resonance. In the superfluid regime, the axial compressional oscillation is excited with a controlled amplitude by changing suddenly $\varepsilon_{dd}$. The transition to the supersolid regime is signaled by the appearance of side peaks in the momentum distribution, reflecting the in-trap lattice spacing. Even an adiabatic crossing of the transition results in an excitation of the axial compressional oscillation, which can thus be observed without changing the trapping frequencies. Because of rapid three-body losses, the observation time has been limited to just a few lattice periods.
While in the superfluid regime, the theory-experiment agreement is remarkable (see figure 4.5), in the supersolid regime, the time evolution of $\langle k_x^2 \rangle$ did not show any beating. However, monitoring two observables directly related to the two modes found in the theory, namely the position of the side peaks in the momentum distribution (related to the lattice period) and its amplitude (related to the lattice depth), it has been demonstrated that these two observables oscillate with different frequencies: the higher frequency one is associated with the lattice spacing, i.e. with the "crystal" mode; the lower frequency one is instead associated with the lattice depth, i.e. with the "phase" mode. The agreement in these regime is more qualitative. Finally, it has not been possible to explore the independent droplet regime because of rapid three-body losses caused by a rapid increase of the density in the peaks.

## 4.3 Moment of Inertia and scissors modes

As discussed in previous chapters, fundamental properties of supersolids show up in their rotational behavior, in particular in connection to their partial superfluid character [14, 15]. Evidences of supersolid behavior in solid helium were in fact searched through deviations of the moment of inertia of the system, measured using a torsional pendulum [17], from the rigid body value. Unfortunately, these experiments were shown to be inconclusive in demonstrating that supersolidity actually occurs in solid helium [21].
In this section, we apply a similar idea to our dipolar BEC confined in a cigar-shaped harmonic trap [75]. In this case, the equivalent of a torsional pendulum experiment can be performed by suddenly rotating the confining harmonic potential, and studying the successive rotational oscillation. Such oscillation, called the *scissors mode*, can be directly related to the superfluid character of the system, as its frequency is dictated by the value of the moment of inertia.
The scissors mode has been extensively studied in nuclear physics [76, 77, 78], where it consists of a relative rotational oscillation of protons and neutrons in

deformed nuclei. It has also been predicted [79] and measured [80] in ordinary (non-dipolar) BECs confined in anisotropic harmonic potentials, confirming the irrotational behavior of the velocity field associated with superfluidity.
The frequency of the scissors mode can be estimated once again using a sum-rule argument, under the single-mode approximation. Consider in particular a rotational oscillation around the polarization axis of the dipoles (z-axis). In this case, the perturbation operator that excites rotational oscillations around the z-axis is the projection $\hat{L}_z$ of the angular momentum operator along the polarization axis. An upper bound on the frequency of the scissors mode can then be obtained by considering the ratio between the energy weighted $m_1 = \int d\omega\omega S(\hat{L}_z, \omega)$ and the inverse energy weighted moment $m_{-1} = \int d\omega\omega^{-1} S(\hat{L}_z, \omega)$ of the dynamic structure factor $S(\hat{L}_z, \omega) = \sum_n |\langle n|\hat{L}_z|0\rangle|^2 \delta(\omega - \omega_n)$ relative to the angular momentum operator $\hat{L}_z$. The $m_1$ moment can be estimated using the sum-rules 2.37, finding

$$m_1 = \frac{1}{2}\left[\hat{L}_z, \left[\hat{H}, \hat{L}_z\right]\right] = \frac{N\hbar^2 m(\omega_y^2 - \omega_x^2)}{2\langle x^2 - y^2\rangle} \tag{4.8}$$

Notice that this result is valid in general for any interaction potential commuting with $\hat{L}_z$, as is the case of the dipole-dipole interaction for atomic dipoles polarized along the z-axis. Moreover, in this case, the static response function is equal to the moment of inertia (per particle) $\Theta$. Hence, the inverse energy weighted moment $m_{-1}$ results in $m_{-1} = \frac{1}{2}N\Theta$. Putting these two results together, we find the following upper bound on the frequency of the scissors mode

$$\omega_{scissor} = \sqrt{\frac{m_1}{m_{-1}}} = \sqrt{\frac{m(\omega_y^2 - \omega_x^2)\langle x^2 - y^2\rangle}{\Theta}} \tag{4.9}$$

Using equation 4.9, we can extract the value of the moment of inertia $\Theta$ of the system by a direct measurement of the frequency $\omega_{scissor}$ of the scissors mode. We thus perform numerical simulations in which the scissors mode is studied by solving equation 2.24, using as initial condition the ground state of the system in a slightly tilted harmonic trap, calculated as usual using equation 2.23. We consider in particular a dipolar BEC of $N = 40000$ atoms of $^{164}$Dy, confined in a harmonic trap of frequencies $\omega_{x,y,z} = 2\pi(20, 40, 80)Hz$, and an initial tilt of $1^\circ$ around the z-axis. The time-dependent observable of interest is the average value $\langle xy\rangle$. An independent estimate of the frequency of the scissors mode can be obtained again using equation 4.9, but calculating the moment of inertia $\Theta$ independently, using its definition

$$\Theta = \lim_{\Omega\to 0} \frac{\langle \hat{L}_z\rangle}{\Omega} \tag{4.10}$$

where the average $\langle \hat{L}_z\rangle$ is calculated in the stationary state of the system in presence of the small perturbation $\hat{H}_{pert} = -\Omega\hat{L}_z$ (i.e., imposing an angular momentum

constraint).
The choice of the trapping frequencies is of great importance, since the deformation of the trap affects the interpretation we give to the observed value of $\Theta$. Consider in fact an ordinary BEC confined in a harmonic trap, and assume that the velocity field is fully irrotational. Plugging then the ansatz $\vec{v} = \alpha\nabla(xy)$ into the hydrodynamic equations of superfluids, and using $\alpha$ as a variational parameter, one finds that an upper bound to the moment of inertia is given by [81]

$$\Theta_{irr} \leq \frac{\langle x^2 - y^2\rangle}{\langle x^2 + y^2\rangle}\Theta_{rig} \tag{4.11}$$

where $\Theta_{rig} = N\langle x^2 + y^2\rangle$ is the moment of inertia of a rigid body with the same density distribution as the system. Hence, for a very elongated system with $\langle x^2\rangle \gg \langle y^2\rangle$, the moment of inertia is the same as the one of a rigid body even if the velocity field is fully irrotational, as in superfluids. Notice also that if $\langle x^2\rangle = \langle y^2\rangle$, i.e. if the system is isotropic in a plane orthogonal to the rotation axis, the irrotational value of the moment of inertia vanishes identically, hence the system does not react to any small rotational perturbation. In order to spot the irrotational behavior of the velocity field of the system, and thus find evidences of superfluidity, it is better to work with moderately deformed traps in the plane orthogonal to the rotation axis (from which our choice of an aspect ratio $\omega_y/\omega_x = 2$).
The results of our calculations are reported in figure 4.6. The calculated values of the moment of inertia are reported in panel a, in units of the rigid value $\Theta_{rig}$. Red circles show the results of ground-state calculations based on solutions of equation 2.23 in presence of an angular momentum constraint, from which we extract $\Theta$ through the definition 4.10. Black squares represent instead the variational estimate $\Theta_{irr}/\Theta_{rig} = \langle x^2 - y^2\rangle/\langle x^2 + y^2\rangle$. We can see that the transition between the superfluid and the supersolid phase is characterized by a visible jump that reflects its first order nature. In the supersolid phase, the ratio $\Theta/\Theta_{rig}$ significantly increases as a consequence of the presence of the density peaks which provides a solid-like contribution to $\Theta$. By further increasing $\varepsilon_{dd}$, the moment of inertia approaches the rigid value, as the system tends to behave as a "crystal" of independent droplets.

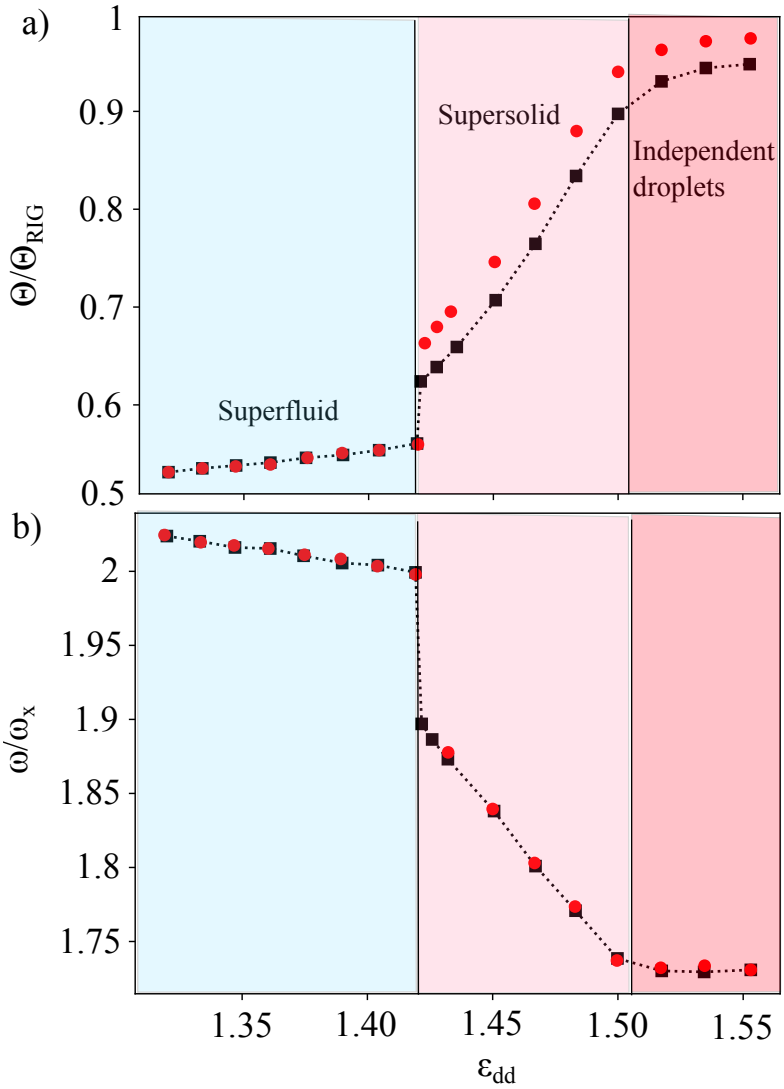


Figure 4.6: a) Moment of inertia of a dipolar BEC of $N = 40000$ atoms of $^{164}$Dy, confined in a harmonic trap of frequencies $\omega_{x,y,z} = 2\pi(20, 40, 80)Hz$, as function of $\varepsilon_{dd}$. Red circles show the results of the ground-state calculations carried out using expression 4.10, by solving equation2.23 in presence of the perturbation $\hat{H}_{pert} = -\Omega\hat{L}_z$, while black squares show the irrotational estimate given by equation 4.11. b) Frequency of the scissor mode as function of $\varepsilon_{dd}$. Black squares correspond to the sum rule estimate 4.9, inserting the value of the moment of inertia extracted from 4.10. Red circles correspond to the frequency of the time-dependent signal $\langle xy \rangle$ obtained from real-time simulations based on equation 2.24.

Notice that, differently from the superfluid phase, in the supersolid and independent droplet phases, the moment of inertia calculated using equation 4.10,

i.e. imposing an angular momentum constrain on the ground-state of the system, does not coincide with the irrotational estimate 4.11. This is due to the fact that the velocity field of the supersolid in proximity of the density peaks behaves approximately like the rotational field that characterizes rigid rotations (see also next Chapter). Thus, the velocity field, in this case, is not fully captured by the simple variational ansatz $\nabla(xy)$, which instead describes well the velocity field in a superfluid. The deviation between the moment of inertia of the supersolid and the irrotational value is an important signature of the partial superfluid nature of the supersolid.
The value of the moment of inertia can be used to estimate the frequency of the scissors mode using the sum-rule estimate 4.9. The result is reported in figure 4.6 panel b (black squares), together with results obtained from the time-dependence of the signal $\langle xy \rangle$, extracted from numerical solutions of equation 2.24 (red circles). We can see that in this case, the agreement between the two estimates is remarkable, implying that the single-mode approximation is well satisfied in all the three regimes. This also implies that an experimental measurement of the scissors mode frequency would provide a direct estimate of the moment of inertia of the system, whose eventual deviation from the irrotational value 4.11 would be a proof of the only partial superfluid character of the system. First experimental investigations of these aspects have already been performed [82], showing reasonable agreement with our theoretical predictions.

# Chapter 5

# Quantized vortices

Up to now, we have considered configurations in which the dipolar BEC breaks translational invariance along one direction only, resulting in a quasi one-dimensional supersolid or independent droplet crystal. We have also seen that the quasi one-dimensional setup, despite its simplicity, allows to study the fundamental manifestations of supersolidity, and to have the first comparisons between theory and experiments. We have seen in particular that this configuration allows to find evidences of the existence of the two Goldstone modes predicted for a system in a ring trap, and to prove superfluid effects, for example the occurrence of a non-classical rotational inertia.
Another fundamental manifestation of superfluidity in a general many-body system is the occurrence of *quantized vortices*, vortex lines characterized by a quantization of the circulation of the velocity field around the vortex core. This interesting manifestation of superfluidity can be better studied, in our dipolar BEC, considering a trapping configuration which is isotropic in a plane orthogonal to the polarization direction.
In this chapter, we will thus consider a dipolar BEC confined in a so-called "pancake-shaped" harmonic trap, obtained by confining the dipoles along the polarization direction (z-axis) with a strong harmonic confinement, while imposing an isotropic in-plane harmonic trap with $\omega_x = \omega_y = \omega_\perp$. We will show that this configuration can host vortices, and will study both their static properties and their dynamical nucleation mechanism.

## 5.1 Ground-state density profiles

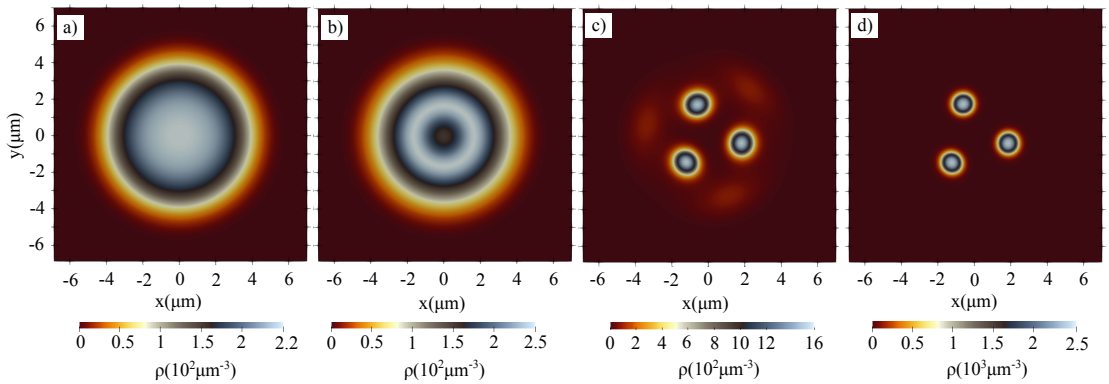


Figure 5.1: In-situ density profiles in the $z = 0$ plane of a dipolar BEC of 40000 atoms of $^{164}$Dy confined in a harmonic trap of frequencies $\omega_{x,y,z} = 2\pi(60, 60, 120)Hz$. a) Superfluid phase at $\varepsilon_{dd} = 1.31$; b) Superfluid phase at $\varepsilon_{dd} = 1.393$ with a "red-blood cell" shape, characterized by a density depletion at the center of the trap, and the maximum density along a ring with a radius of $\simeq 2\mu m$; c) Supersolid phase at $\varepsilon_{dd} = 1.394$; d) Independent droplet phase, at $\varepsilon_{dd} = 1.5$.

We consider configurations in which the dipolar BEC is confined in a harmonic trap *isotropic* in the x-y plane, orthogonal to the polarization direction z. Specifically, we start with a simple setup, namely a system of $N = 4 \times 10^4$ atoms of $^{164}$Dy confined in a harmonic trap of frequencies $\omega_{x,y,z} = 2\pi(60, 60, 120)$Hz. The ground-state density profiles can be obtained from solutions of equation 2.23, and are shown in figure 5.1. We can see that, as in the quasi one-dimensional case studied in previous chapters, they are deeply affected by the value of $\varepsilon_{dd}$, and allow to distinguish three phases: a superfluid phase (with our choice of the parameter, for $\varepsilon_{dd} < 1.393$), characterized by symmetry for continuous rotations around the z-axis (figure 5.1 panels (a)-(b)), a supersolid phase ($1.394 \leq \varepsilon_{dd} < 1.5$), characterized by partially overlapping density peaks, spontaneously self-arranging in a *triangular* lattice (figure 5.1 panel (c)), and an independent droplet crystal ($\varepsilon_{dd} \geq 1.5$), in which the density peaks are well separated (figure 5.1 panel (d)). Under certain circumstances, the ground-state density profile in the superfluid phase can exhibit a biconcave ("red-blood cell") shape (here, $1.31 < \varepsilon_{dd} < 1.393$, see figure 5.1 panel (b)), characterized by a density depletion at the center of the trap and the maximum density along a "ring" in the x-y plane [83].

## 5.2 Single vortex line

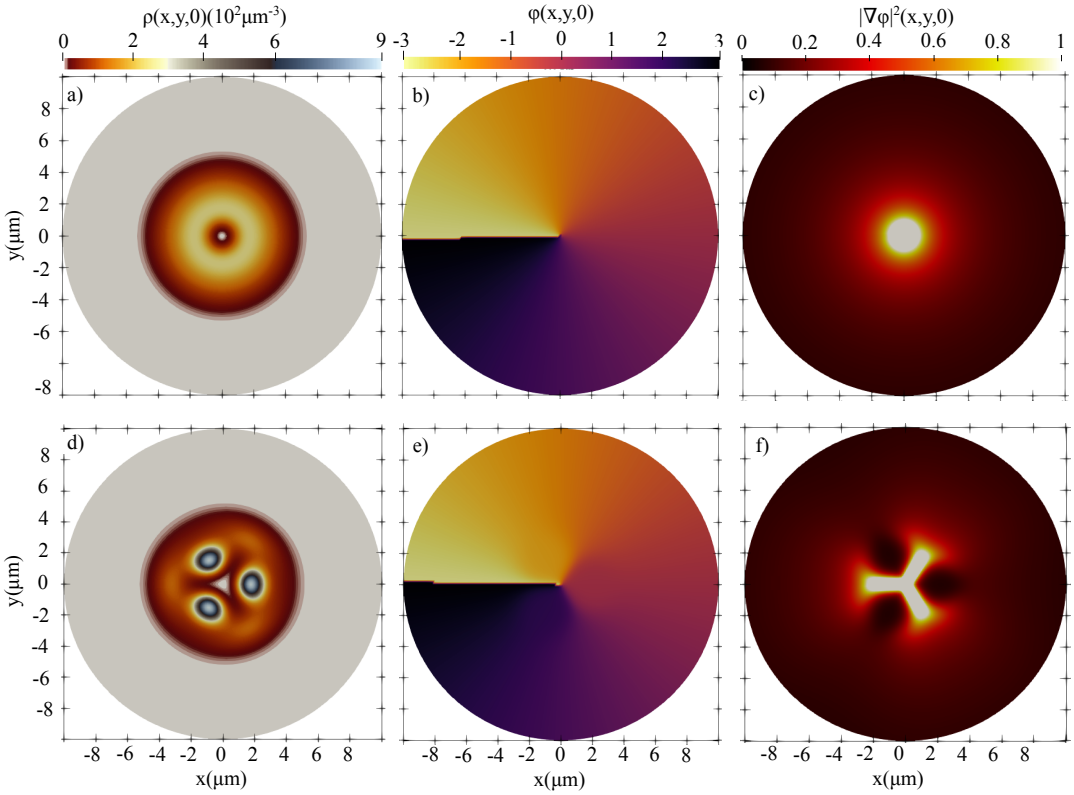


Figure 5.2: In presence of a vortex line parallel to the polarization direction (z-axis) at the center of the trap, in situ density profiles (a,d), phase (b,e) and amplitude of the velocity field (c,f) in the $z = 0$ plane for a dipolar BEC of 40000 atoms of $^{164}$Dy in a harmonic trap of frequencies $\omega_{x,y,z} = 2\pi(60, 60, 120)Hz$, in the superfluid phase (a,b,c) at $\varepsilon_{dd} = 1.31$, and the supersolid phase (d,e,f) at $\varepsilon_{dd} = 1.40$. The plots refer to the ground state of the system in presence of an angular momentum constraint, and are obtained from solutions of equation 2.23 with the addition of the rotating perturbation $\hat{H}_{pert} = -\Omega\hat{L}_z$ for $\Omega = 2\pi(15)Hz$. The magnitude of the velocity field (c,f), proportional to the square modulus of the gradient of the phase of the condensate wave function, is reported in arbitrary units.

The physics of quantized vortices in dipolar BECs has been studied in detail in absence of the Lee-Huang-Yang correction [84, 85, 86] in the mean-field stable region of the superfluid phase. Here, we consider instead the mean-field unstable region of the phase diagram, focusing in particular on the supersolid phase. We show that the superfluid and supersolid ground-state configurations described in

the previous section can host a vortex line oriented along the polarization direction of the dipoles (z-axis), and located at the center of the trap, in presence of a sufficiently strong angular momentum constrain.
We study ground-state configurations of the system obtained from solutions of equation 2.23, in presence of the perturbation $\hat{H}_{pert} = -\Omega \hat{L}_z$. These solutions are characterized by the occurrence of a vortex line at the center of the trap, oriented along the z-axis (see figure 5.2) for an angular velocity $\Omega$ larger then a certain critical value $\Omega_{crit}$. This is the angular velocity at which the energy in the rotating frame is smaller if the system hosts a vortex line [2].
It is particularly interesting to consider the vortex line hosted at the center of the triangular cell of the supersolid, shown in figure 5.2 panel (d). The size of the vortex core is in fact comparable with the inter-droplet distance (here, around $2\mu m$), and even the shape of the vortex core, being clearly triangular, reflects the shape of the lattice cell. This is clearly different from the case of a vortex line in the superfluid phase (figure 5.2 panel a), where the vortex shows obviously the usual cylindrical symmetry. Moreover, the velocity field of the system, related to the phase $\phi$ of the condensate wave function by $\vec{v} = \frac{\hbar}{m}\nabla\phi$, is null at the position of the density peaks in the rotating frame (figure 5.2 panel (f), where we report $|\nabla\phi|^2$, proportional to the magnitude of the velocity field, and figure 5.3 panel b, where we report $\nabla\phi$), while it is maximum at the vortex core in the center of the trap and in the valleys between the density peaks. This behavior is radically different from that of the velocity field in the supersolid phase in absence of a vortex (see figure 5.3 panel (a)), i.e. when the rotational frequency $\Omega$ is smaller then the critical value $\Omega_{crit}$. In this case, in fact, the droplets rotate around the center of the trap similarly to a rigid body (i.e., with an approximately rotational velocity field) [75]. This implies that the nucleation of a vortex line involves only the superfluid fraction of the supersolid: when the rotation frequency is high enough, in fact, the system prefers to nucleate a vortex in the valley between the density peaks, while the lattice, in the rotating frame, remains at rest.

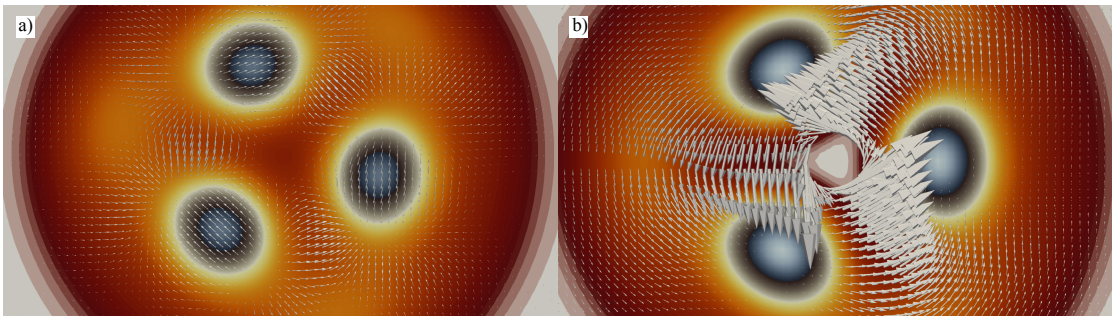


Figure 5.3: Velocity field $\vec{v} = \frac{\hbar}{m}\nabla\phi$, where $\phi$ is the phase of the condensate wave function, in absence (a) and in presence (b) of a vortex line along the z-axis at the center of the trap, for a dipolar BEC of 40000 atoms of $^{164}$Dy confined in a harmonic trap of frequencies $\omega_{x,y,z} = 2\pi(60, 60, 120)Hz$, in the supersolid phase at $\varepsilon_{dd} = 1.394$. The plots correspond to the ground state of the system in presence of an angular momentum constraint, and are obtained from solutions of equation 2.23 with the addition of the rotating perturbation $\hat{H}_{pert} = -\Omega\hat{L}_z$. In panel (a), $\Omega$ is smaller then the critical value $\Omega_{crit}$ at which hosting a vortex becomes energetically favorable. In panel (b), instead, $\Omega$ is larger then $\Omega_{crit}$. The velocity field in this case is plotted around the vortex core, but not inside, where the velocity tends to diverge.

The size of the vortex core in the superfluid phase increases rapidly with $\varepsilon_{dd}$ (see figure 5.4), as the superfluid-supersolid phase transition is approached [87]. In the non-dipolar case, the size of the vortex core is fixed by the *healing length* $\xi = \hbar/\sqrt{2mgn}$, which is also reported for comparison in figure 5.4 (black dots). Notice that in the dipolar case, the size of the vortex core is much larger then the non-dipolar case, making these vortices potentially observable, in experiments, even in-situ. In the supersolid phase, instead, we can see that the size of the vortex core remains approximately constant, being determined only by the distance between the density peaks.

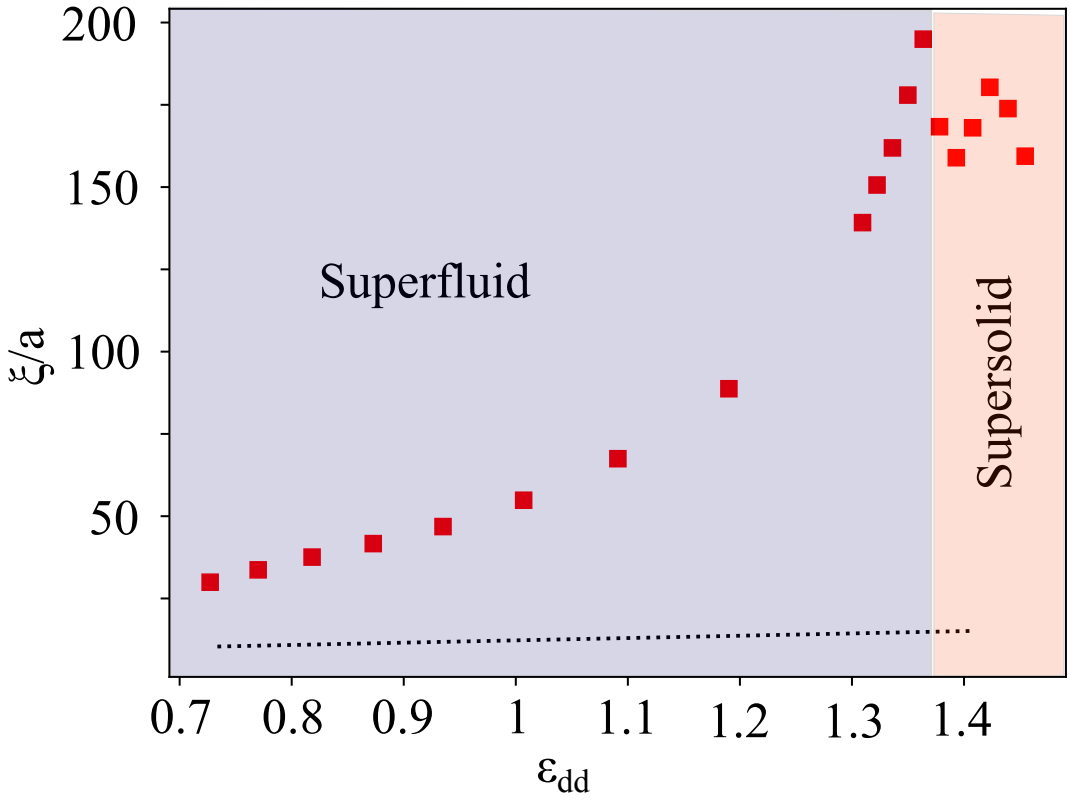


Figure 5.4: Vortex core size $\xi$ (in units of the scattering length $a$), defined as the half width at half maximum of the condensate wave function at the vortex position, as a function of $\varepsilon_{dd}$, both in the non-dipolar (black dotted line) and dipolar (red squares) case. The values are taken from solutions of equation 2.23 in presence of the rotating perturbation $\hat{H}_{pert} = -\Omega\hat{L}_z$, for a dipolar BEC of 40000 atoms of $^{164}$Dy, in a harmonic trap of frequencies $\omega_{x,y,z} = 2\pi(60, 60, 120)Hz$, and $\Omega = 2\pi(12.7)Hz$.

Another interesting result concerns the angular momentum per particle carried by the vortex line in the supersolid phase. This can be evaluated by considering the jump $\Delta$ in the angular momentum per particle at $\Omega = \Omega_{crit}$. In a fully superfluid system, this value is equal to $\hbar$, while in a system which shows only a partially superfluid character, this value is expected to be smaller. The dependence of $\Delta$ (in units of $\hbar$) on $\varepsilon_{dd}$ is illustrated in figure 5.5 panel (a) (red squares). We can see that, while in the superfluid regime, the value of $\Delta/\hbar$ is exactly 1, in the supersolid regime assumes a value smaller then 1, which keeps decreasing until vanishing in the independent droplet regime. This jump can be compared with an estimate of

the superfluid fraction based on the moment of inertia:

$$f_{NCRI} = 1 - \frac{\Theta}{\Theta_{rig}} \tag{5.1}$$

where $\Theta$ is the moment of inertia of the system and $\Theta_{rig}$ is the rigid body value. Expression 5.1 coincides exactly with the superfluid fraction in a ring geometry [14, 15, 24], while gives a reasonable estimate in other geometries.

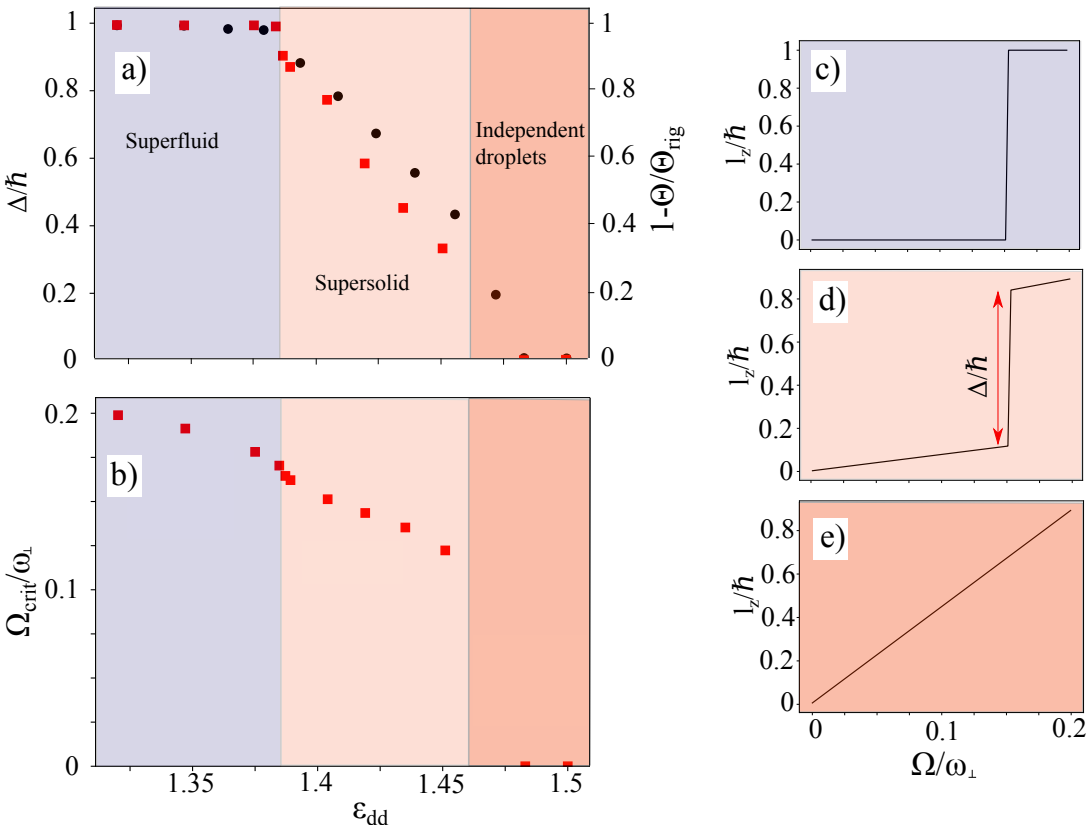


Figure 5.5: a) Jump $\Delta$ (red squares) in the angular momentum per particle at the critical rotation frequency $\Omega_{crit}$ at which hosting the vortex becomes energetically favorable, and fraction of non-classical rotational inertia $f_{NCRI}$ (black circles) as defined in equation 5.1, as function of $\varepsilon_{dd}$. b) Critical rotation frequency $\Omega_{crit}$ as a function of $\varepsilon_{dd}$. c,d,e) Angular momentum per particle as a function of the rotation frequency $\Omega$ for $\varepsilon_{dd} = 1.31$ (superfluid), $\varepsilon_{dd} = 1.41$ (supersolid) $\varepsilon_{dd} = 1.5$ (independent droplets). The values are taken from solutions of equation 2.23 in presence of the rotating perturbation $\hat{H}_{pert} = -\Omega \hat{L}_z$, for a dipolar BEC of 40000 atoms of $^{164}$Dy, in a harmonic trap of frequencies $\omega_{x,y,z} = 2\pi(60, 60, 120)Hz$.

In figure 5.5 panel (a), we compare $\Delta$ (red squares) and $f_{NCRI}$ (black circles).

In the superfluid phase, both quantities are equal to 1, since the system is fully superfluid. In the supersolid phase, instead, the two quantities are smaller then 1, but slightly different, with, in particular, $f_{NCRI} > \Delta$. Moreover, in the independent droplet phase, while $\Delta$ vanishes, $f_{NCRI}$ remains finite, since each droplet is itself superfluid. On the other hand, $\Delta$ only accounts for the superfluid component participating to the vortex circulation, providing thus a more accurate estimate of the superfluid fraction of the system.
The critical frequency $\Omega_{crit}$ at which the nucleation of the vortex is energetically favorable is also deeply affected by the value of $\varepsilon_{dd}$. In references [84, 85, 86] it is shown that $\Omega_{crit}$ increases with $\varepsilon_{dd}$ in the mean-field stable region of the superfluid, reaching a maximum at $\varepsilon_{dd} \simeq 1$, and then decreasing as the mean-field unstable region of the superfluid is approached. As shown in figure 5.5 panel (b), this result extends also in the mean-field unstable region, where $\Omega_{crit}$ keeps on decreasing, showing a small jump at the superfluid-supersolid phase transition, and still decreasing in the supersolid region until the independent droplet phase is reached. Here, in absence of any overlap between the droplets, the ground state of the system does not host vortices, even at high values of angular velocity [87].

## 5.3 Quadrupole instability and vortex nucleation

We have seen in the previous section that the nucleation of a vortex line becomes energetically favorable in a frame rotating with a frequency higher then a certain critical frequency $\Omega_{crit}$. The actual nucleation mechanism of vortices in a rotating harmonic trap is however non-trivial, and has been extensively studied in non-dipolar BECs [88, 89, 90, 91]. In this case, in fact, vortex nucleation can be induced by introducing a quadrupolar rotating deformation of the trap, characterized by a rotation frequency $\Omega$ and deformation parameter

$$\epsilon = \frac{(\omega_x^2 - \omega_y^2)}{(\omega_x^2 + \omega_y^2)} \tag{5.2}$$

Also in this case, there exist a critical frequency $\Omega_{NV}$ for the nucleation of a vortex [92, 93], which turns out be significantly larger then the frequency $\Omega_{crit}$ at which the nucleation of the vortex is energetically favorable. This is due to the presence of an energetic barrier [2] for the vortex to enter in the system, due to the need of creating a density depletion at the vortex position. The nucleation of a vortex can thus be triggered by a dynamical instability, which can be due to collective modes acquiring a negative frequency in the rotating frame for a certain critical value of the rotation frequency $\Omega$. In the case of a rotating quadrupolar deformation in an ordinary BEC confined in a pancake-shaped trap, this happens at the resonance frequency $\Omega_{NV} = \omega_q/2$ [81], where $\omega_q = \sqrt{2}\omega_\perp$ is the frequency

of the quadrupole mode [71]. The dynamical instability of the quadrupole mode leads to a spontaneous breaking of the cylindrical symmetry of the cloud, creating the conditions for vortices to be nucleated.

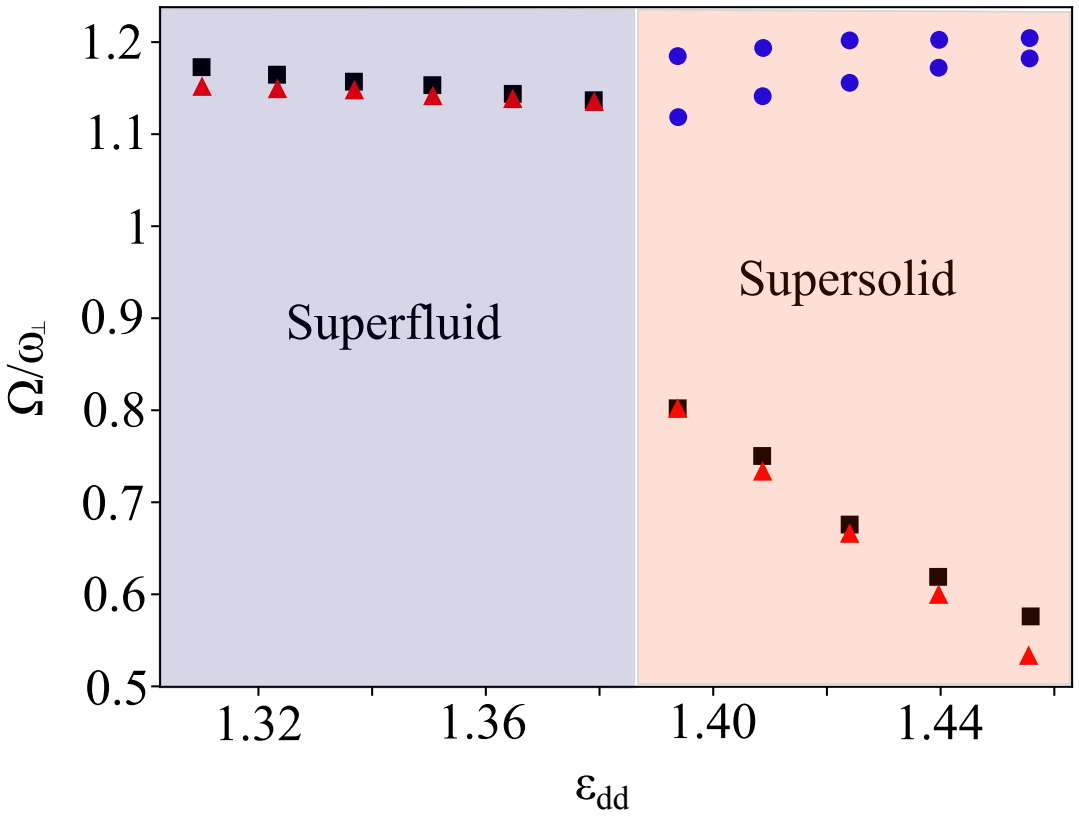


Figure 5.6: Twice the critical frequency for vortex nucleation via the introduction of a rotating quadrupolar deformation (red triangles), and frequencies of quadrupolar compressional modes (black squares and blue circles), as function of $\varepsilon_{dd}$. While in the superfluid phase one finds a single mode excited by a sudden quadrupolar deformation (black squares), in the supersolid phase one finds three modes, two of which are associated with lattice excitations (blue circles) and one with superfluid oscillations (black squares), reflecting the presence of three Goldstone modes in an infinite system. The relation $\Omega_{NV} = \omega_q/2$, expected for a superfluid (see text), remains valid also in the supersolid.

The same resonance condition $\Omega_{NV} = \omega_q/2$ has been shown to work with vortex nucleation in dipolar BECs, in the mean-field stable region of the phase diagram [94]. Notice however, that, in the dipolar case, the quadrupole frequency is not given simply by $\sqrt{2}\omega_\perp$, but rather depends in a non-trivial manner on the interaction strength and the trapping parameters [47].

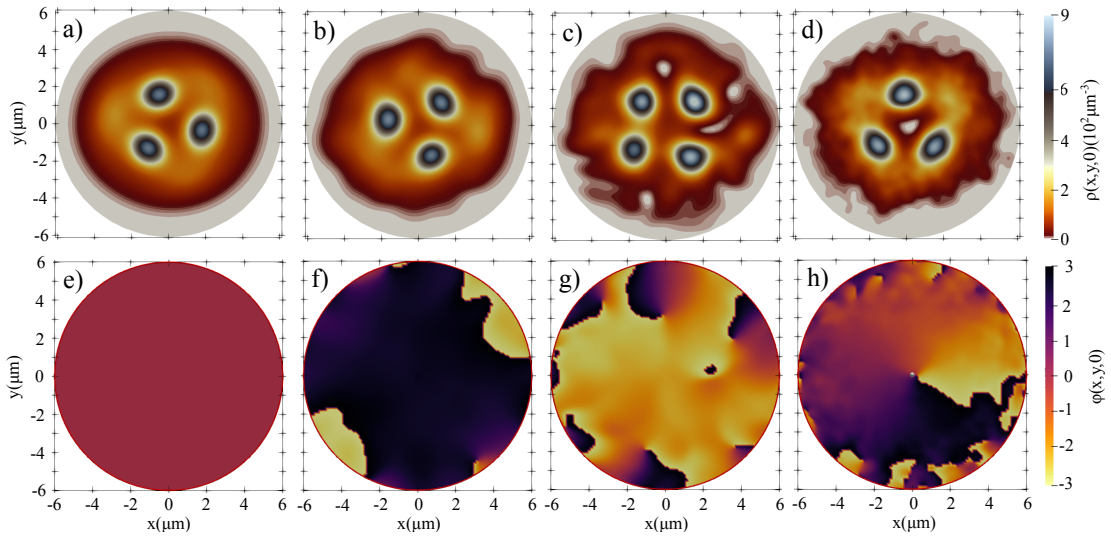


Figure 5.7: In-situ density profiles (a-d), and corresponding phase of the condensate wave function (e-h), in the $z = 0$ plane, showing the nucleation of a vortex in a gas of $N = 40000$ atoms of $^{164}$Dy, in a slightly deformed trap, of frequencies $\omega_{x,y,z} = 2\pi(59.9, 60.1, 120)Hz$ and $\varepsilon_{dd} = 1.4$. a,e) Initial preparation of the gas in the supersolid ground state. b,f) The system is put in rotation by the adiabatic introduction of an angular momentum constraint, until the angular velocity of $2\pi(23)Hz$ is reached. The system shows a slight quadrupolar deformation in the $z = 0$ plane. Several vortices forms at the surface of the system. c,g) The vortices try to penetrate the lattice through the interstitial regions between the droplets in order to lower the energy. d,h) A single vortex finally settles at the center of the trap.

Solving equation 2.24 in a frame rotating with angular velocity $\Omega$, we have shown that the same resonance condition holds also in the mean-field unstable region of the superfluid phase, and, quite remarkably, also in the supersolid phase [87], as shown in figure 5.6. In the supersolid phase, the quadruple oscillation frequencies can be studied similarly to the axial compressional frequencies studied in Chapter 4 of this thesis. In particular, we do this by evolving equation 2.24 in real time, using, as initial condition, the ground state of the system in presence of a slight quadrupolar deformation of the trap of the form 5.2. We find that a sudden quadrupolar perturbation in the supersolid phase excites three modes that can be associated with the three Goldstone modes expected for an infinite, quasi-2D supersolid [27]: one Goldstone mode associated with the spontaneous breaking of the U(1) symmetry responsible for superfluidity and two associated with the spontaneous breaking of translational invariance along two directions. The results for the quadrupole frequencies are reported in figure 5.6 (black squares

and blue circles). The frequency of the lower energy mode decreases with an increase of $\varepsilon_{dd}$ in the supersolid phase (figure 5.6, black squares), until vanishing in the independent droplet regime, while the frequencies of the higher two (figure 5.6 blue circles) tend to increase until reaching an approximately constant value. Comparing the lower frequency with the critical one for vortex nucleation $\Omega_{NV}$, obtained by directly evolving equation 2.24 in a frame rotating with frequency $\Omega$ (adding also a slight quadrupolar deformation of the form 5.2 to the trap), we find that the resonance condition $\Omega_{NV} = \omega_q/2$ is satisfied (figure 5.6 red triangles) with good approximation, considering just the lower frequency quadrupole mode. Moreover, similarly to what happens in the superfluid regime, also in the supersolid regime the nucleation follows a strong deformation of the cloud, as shown in the snapshots reported in figure 5.7. Our simulation predicts rather long times (of the order of 1 second) for the vortex nucleation. However, in real experiments, noise and thermal effects are expected to trigger the instability on a much faster time scale. Larger trap deformations also help in speeding up the nucleation process.

## 5.4 Vortex lattices

If the frequency $\Omega$ of the rotating perturbation is high enough, a superfluid can host many vortex lines, which spontaneously arrange in a triangular lattice in the x-y plane [95]. We have checked that this is true also for our dipolar BEC in the whole superfluid regime, both in the mean-field stable region of the phase diagram as well as in the Lee-Huang-Yang dominated regime, till the supersolid phase transition. Moreover, as shown in figure 5.8, the larger size of the vortex in the dipolar case compared to the non-dipolar one, implies that the total number of vortices hosted by the system in the latter case is smaller then in the former.

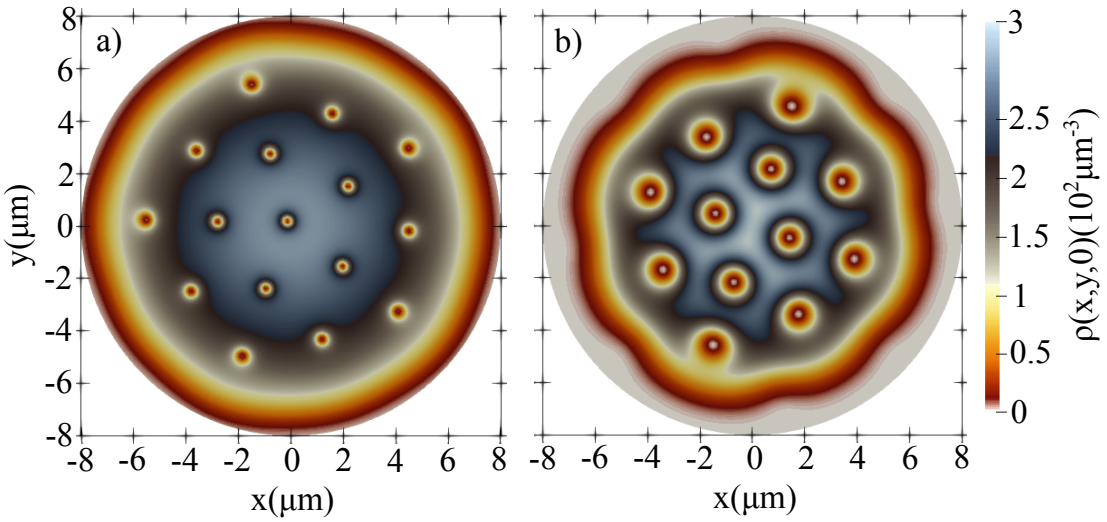


Figure 5.8: Vortex lattice in the superfluid phase, for a non-dipolar (panel a) and for a dipolar BEC (panel b). Panel (b) refers to a dipolar BEC of 40000 atoms of $^{164}$Dy confined in a harmonic trap of frequencies $\omega_{x,y,z} = 2\pi(60, 60, 120)Hz$, rotating around the z-axis at a frequency $\Omega = 2\pi(30)Hz$. Panel (a) refers to the same conditions, but switching off both the dipole-dipole interaction and the Lee-Huang-Yang term in equation 2.23.

In the supersolid phase, it is convenient to consider a system with a larger number of lattice sites, in order to study the coexistence of the density modulation of the supersolid and the vortex lattice. For this reason, we consider the same configuration as in the previous section, but with a larger number of atoms, equal to 110000. In these conditions, we find that, for $\varepsilon_{dd} = 1.41$, the system is in the supersolid phase, characterized by 7 density peaks arranged in a triangular lattice, as shown in figure 5.9 panel (a).

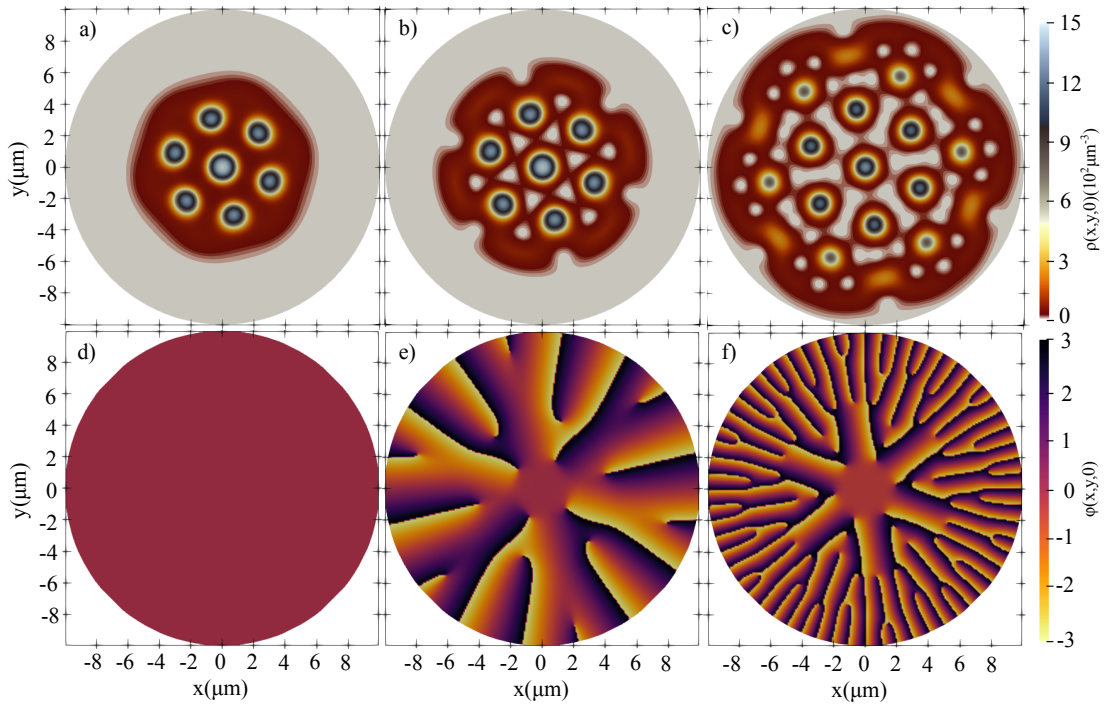


Figure 5.9: In-situ density profiles (a-c) and phase of the condensate wave function (d-f) in the $z = 0$ plane, for a dipolar BEC of 110000 atoms of $^{164}$Dy in the supersolid phase at $\varepsilon_{dd} = 1.41$, confined in an harmonic trap of frequencies $\Omega_{x,y,z} = 2\pi(60, 60, 120)Hz$. a,d) Non-rotating gas at $\Omega = 0$ b,e) $\Omega = 2/3\omega_x$. c,f) $\Omega = 5/6\omega_x$.

Introducing a rotational perturbation characterized by a large enough value of the angular velocity, the ground state of the system is characterized by the appearance of several vortex lines, again parallel to the z-axis. The natural tendency of the vortices to arrange in a triangular lattice is here hindered by the presence of the density modulation of the supersolid, which also forms a triangular lattice. The result is that the position of the vortices is pinned at the density minima of the supersolid lattice. In figure 5.9 panels (b)-(c), we show the typical density profiles, obtained from solutions of equation 2.23 in presence of a rotating perturbation $\hat{H}_{pert} = -\Omega\hat{L}_z$ at large $\Omega$. We find that the vortices are pinned at the minima of the supersolid density modulations, forming, for the chosen value $\Omega = 2/3\omega_x$, a honeycomb lattice (figure 5.9 panel (b)). The pinning of vortex lattices in Bose gases has been already addressed in the non-dipolar case, considering an underlying (square or triangular) rotating optical lattice [96, 97, 98, 99], demonstrating, experimentally, the transition from the natural vortex lattice to the pinned vortex lattice [100]. However, in our case, the structure of the density modulation is not imposed by an external potential, but is due to the spontaneous breaking of translational symmetry, yielding the supersolid phase. The pinned honeycomb

lattice persists as long as $\Omega$ is not too large for the inter-vortex distance to become smaller than the period of the supersolid lattice. By further increasing $\Omega$ we find that the vortices are still hosted in the low density regions surrounding the droplets, tending to merge in large and highly deformed vortices, as shown in the panel (c) of figure 5.9 for $\Omega = 5/6\omega_x$.

## 5.5 Expansion

The previously reported results considered the possibility of addressing the system in-situ. Here we briefly discuss the effect of letting the cloud to expand, i.e., after switching off the trap in the transverse ($z = 0$) plane, in order to image the system with a better space resolution. We consider both the single and the many-vortex case.
Figure 5.10 shows the density profiles of a dipolar supersolid with and without a vortex line at different times after the removal of the in-plane trap. The ratio between the peak density and the central density, in the absence of the vortex, is less than 10 and it further decreases during the expansion, the minimum of the density remaining of the same order as that of an ordinary superfluid. Thus, with our choice of parameters, a good imaging system could easily identify the presence of the vortex in the center of the trap.

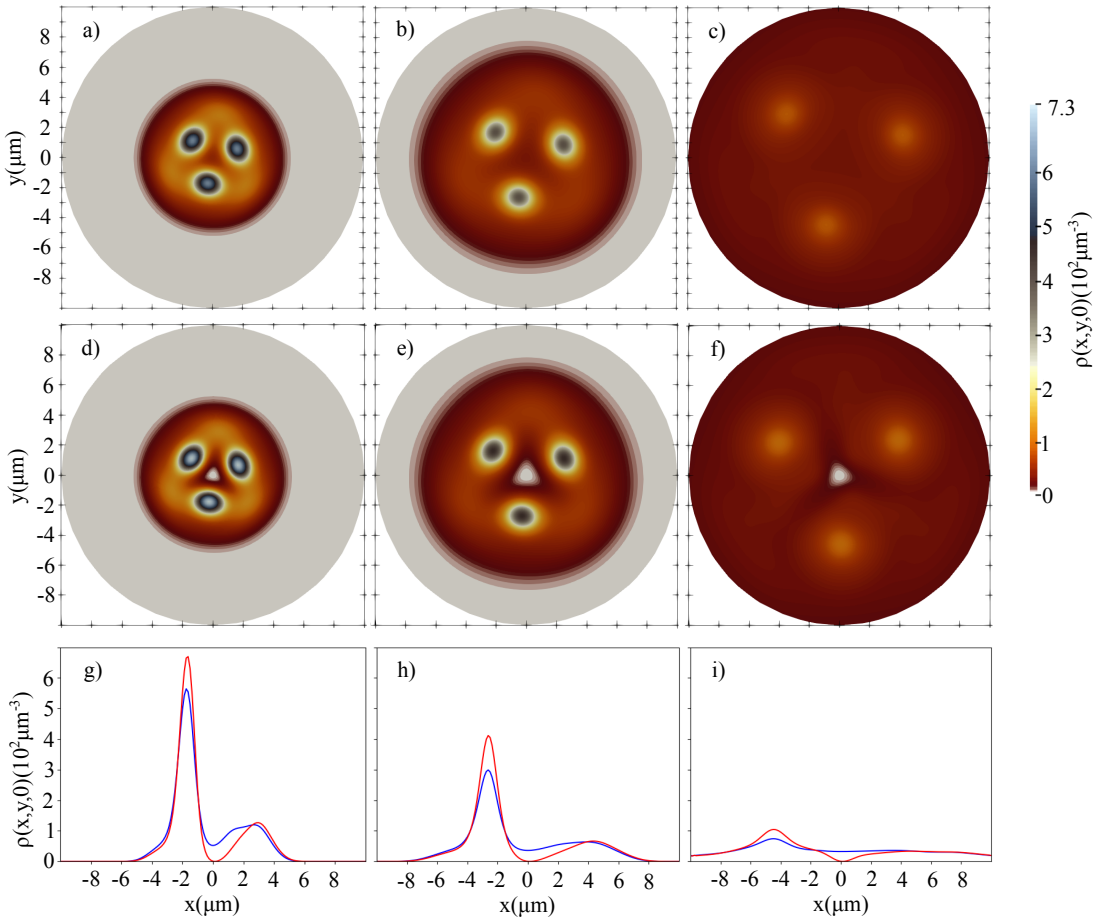


Figure 5.10: In-situ density profiles along the $z = 0$ plane (a-f), and cuts along the x-axis (panels (g-i)) of an expanding dipolar supersolid in the absence (a-c) and in presence (d-f) of a vortex. The initially prepared ground state in presence (d) of a vortex has been obtained for $\Omega = 2\pi(23)Hz$. Panel (g) shows the corresponding density cut along the x-axis. The red (blue) line corresponds to the case with (without) vortex. Panels (h) and (i) show corresponding cuts along the x-axis. The other parameters are the same as in figure 5.1. Snapshots are taken at the initial configuration (a,d,g), and respectively 3 (b,e,h) and 6 ms (c,f,i) after the in-plane confinement has been switched off.

For the high angular frequency case, when many vortices appear, we consider the most interesting case, when the vortices form a honeycomb lattice, as in figure 5.9 panel (b). The expansion at two different times after switching off the transverse confinement is reported in figure 5.11. In particular, we notice that the geometry of the two lattices remains unchanged during the expansion, paving the way for the possible direct observation of the frustration of the vortex lattice.

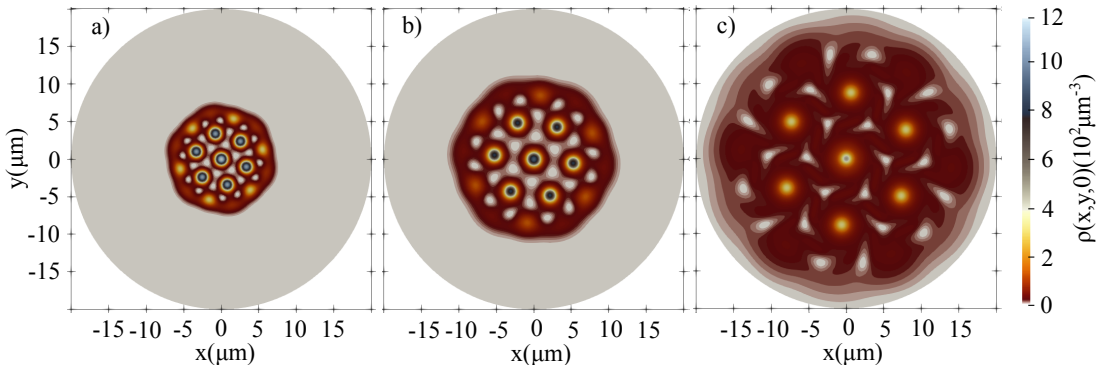


Figure 5.11: Expansion of a dipolar supersolid in presence of the vortex lattice reported in figure 5.9 panel (b). a) Initially prepared state, same as in figure 5.9 panel (b). b,c) In-situ density profiles in the $z = 0$ plane respectively 3 and 6 ms after the in-plane confinement has been switched off.

# Chapter 6

# Dipolar Bose-Einstein condensates in a box

In previous chapters, we have considered a dipolar BEC confined either in a transverse harmonic trap, with periodic boundary conditions along the unconfined direction, or a fully trapped system, confined in a harmonic potential along the three spatial directions. Although harmonic trapping allows the study of relevant properties of ultracold atomic systems, other important properties, for example sound propagation or critical behaviors, can be better studied in uniform systems. For these reasons, Bose-Einstein condensation in box potentials has been an emerging topic of research in recent years, leading to the realization of uniform BECs in gases of alkali atoms and first important measurements in both 3D and 2D configurations [101, 102, 103, 104, 105, 106, 107, 108]. The natural question which arises is therefore how a dipolar gas behaves in a box potential, and to what extent its configurations mimic their thermodynamic counterparts. First theoretical investigations carried out in the deep superfluid phase [109] have pointed out the peculiar phenomenon of accumulation of the density distribution near the boundary, as a consequence of the repulsive behavior of the aligned dipoles. This effect is strongly reduced in presence of transverse harmonic trapping because of the high energetic cost for dipoles to move away from the center of the trap.
In this chapter, we consider the behavior of a dipolar BEC confined in a box potential, with a particular focus on the ground-sate density profiles in the mean-field unstable regime of the phase diagram. We will show that in quasi-two-dimensional geometries, the accumulation along the border is enhanced in the regimes where the Lee-Huang-Yang correction is relevant, creating edges well separated from the bulk. For a relatively small number of atoms, the bulk remains in a low density superfluid phase, while the edges can show typical supersolid or droplet crystal structures. Increasing the atom density leads to a supersolid bulk region, while the edges can be found to be in a high-density superfluid phase. Moreover, we

will show that the lattice emerging in the bulk has not in general a triangular (or honeycomb) pattern, as expected for an infinite system [110], but its structure is dictated by the shape of the confining box potential even for relatively large systems.

## 6.1 A closed wave guide

We first consider a quasi-one-dimensional configuration, similar to the one considered in Chapter 3 of this thesis. However, instead of imposing periodic boundary conditions along the unconfined direction, we "close" the tubular confinement with a hard wall potential at the borders of the simulation cell along the x-axis, realizing, instead of a ring, a closed wave-guide. More specifically, we determine, solving equation 2.23, the ground-state density profiles of $N = 40000$ atoms of $^{164}$Dy confined in a trapping potential of the form

$$V_{ext} = \frac{1}{2}m(\omega_y^2 y^2 + \omega_z^2 z^2) + V_{box}(x, L) \tag{6.1}$$

with $\omega_{y,z} = 2\pi(100)Hz$, $V_{box}(x, L) = V_0$ for $|x| \geq L$ and 0 otherwise, $V_0 = 100\omega_z$ and $L = 12\mu m$. Typical density profiles for different values of $\varepsilon_{dd}$ are reported in figure 6.1 panels (a), (b) and (c). In the figure we also report the density profiles calculated in a quasi-one-dimensional configuration, imposing periodic boundary conditions at $x = \pm L$ (panels (d), (e), (f) ) as well as the corresponding excitation spectra (insets (g), (h)) calculated in the uniform phase by solving the Bogolyubov-de Gennes (BdG) equations 2.16 with the beyond-mean-field correction 2.25. The configurations reported in figure 6.1 panel (d) and (e) correspond to a uniform superfluid characterized by a pronounced roton minimum, precursor of the instability to a periodically modulated density (supersolid phase) for larger values of $\varepsilon_{dd}$ (panel f). In presence of the box, atoms accumulate close to the walls even for small values of $\varepsilon_{dd}$ (weakly interacting dipolar case, panels a, d and inset g), when the excitation spectrum of the uniform phase does not show a roton minimum. Due to the long range and anisotropic nature of the dipolar force, even in this case the density profile deeply differs from the results holding for a one dimensional BEC interacting with a short range potential. In the latter case the density profile, near a hard wall located at $x = 0$, is fixed by the healing length $\xi = \sqrt{\hbar/2mgn}$ according to $n(x) = \tanh^2(x/\sqrt{2}\xi)$ where $n$ is the bulk density away from the edge of the box [2]. The concept of healing length is not easily applicable to the case of a dipolar gas, whose different behavior is due to the long-range nature of the force, the repulsive effect felt by the aligned dipoles, which tend to accumulate near the border, the presence, for large values of $\varepsilon_{dd}$, of rotonic oscillations and, of course, the emergence of spontaneous density modulations characterizing the supersolid

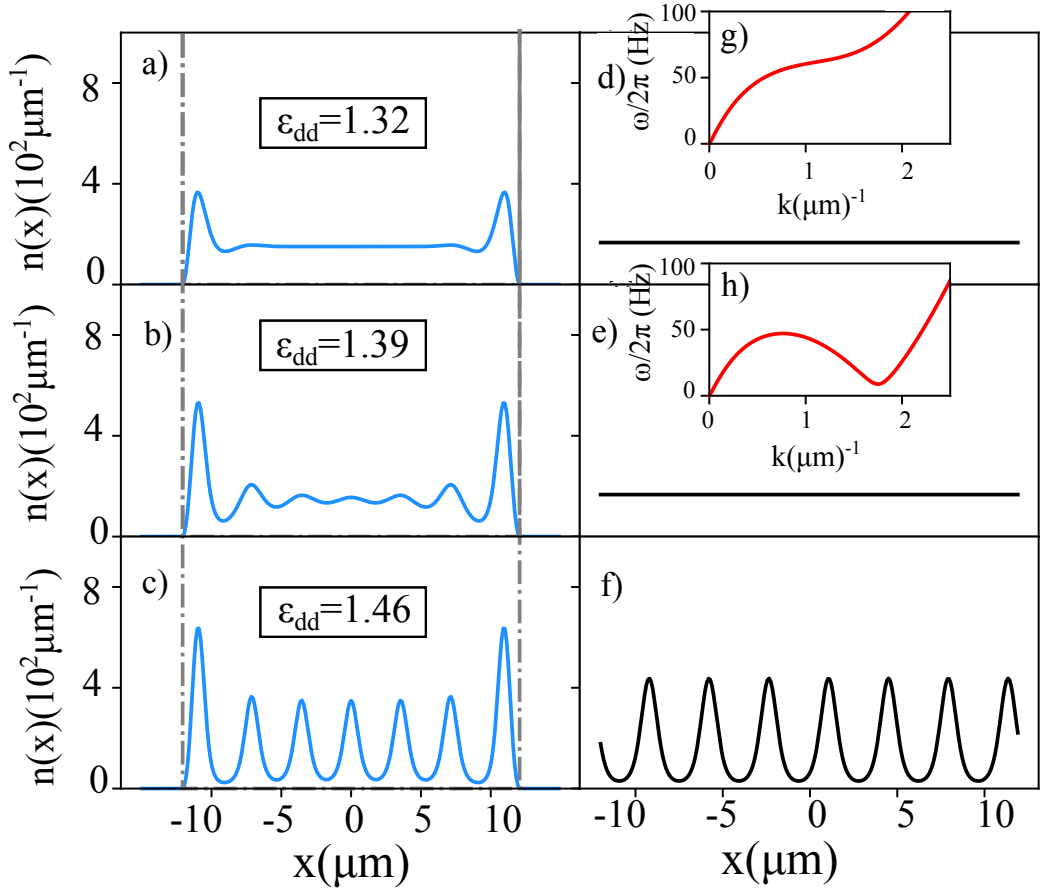


Figure 6.1: Ground state integrated density profiles $n(x) = \int dydz|\Psi(x,y,z)|^2$ of $N = 40000$ atoms of $^{164}$Dy in a transverse harmonic confinement of frequencies $\omega_y = \omega_z = 2\pi(100)Hz$, confined by a box potential of height $V_0 = 100\omega_z$ at positions $x = \pm 12\mu m$ (panels a,b,c) or with periodic boundary conditions at $x = \pm 12\mu m$ (panels d,e,f). Insets g and h show the excitation spectrum calculated by solving the Bogolyubov-de Gennes equations for the configurations of panels d,e. The profiles reported in panels a,d (respectively, b,e and c,f) are calculated by fixing $\varepsilon_{dd} = 1.32$ (respectively, 1.39 and 1.46)

and the independent droplet phases. The emergence of the rotonic oscillations is reminiscent of a similar effect characterizing the density profile in the vicinity of a quantized vortex [84]. This effect, originally theoretically investigated for quantized vortices in superfluid helium, is a direct consequence of the presence of the roton in the excitation spectrum [111, 112, 113].

## 6.2 Edge supersolidity

We now consider the case of a quasi 2-dimensional dipolar BEC, obtained by imposing a harmonic confinement only in the polarization direction (z-axis). We will consider solutions of equation 2.23, in presence of an external trapping potential which, beside being harmonic along the z-axis, will have the shape of a box in the x-y plane. In the absence of confinement in the transverse direction, theory predicts that for a certain value of the density and of $\varepsilon_{dd}$, a phase transition between a uniform superfluid and a supersolid occurs. In the thermodynamic limit, the supersolid lattice is predicted to be triangular or honeycomb [110]. The occurrence of such lattice symmetry has been also predicted for the case of transverse, radially symmetric, harmonic trapping [87, 75]. Very recently, the possible existence of other exotic configurations in harmonic traps has been proposed [114, 115].

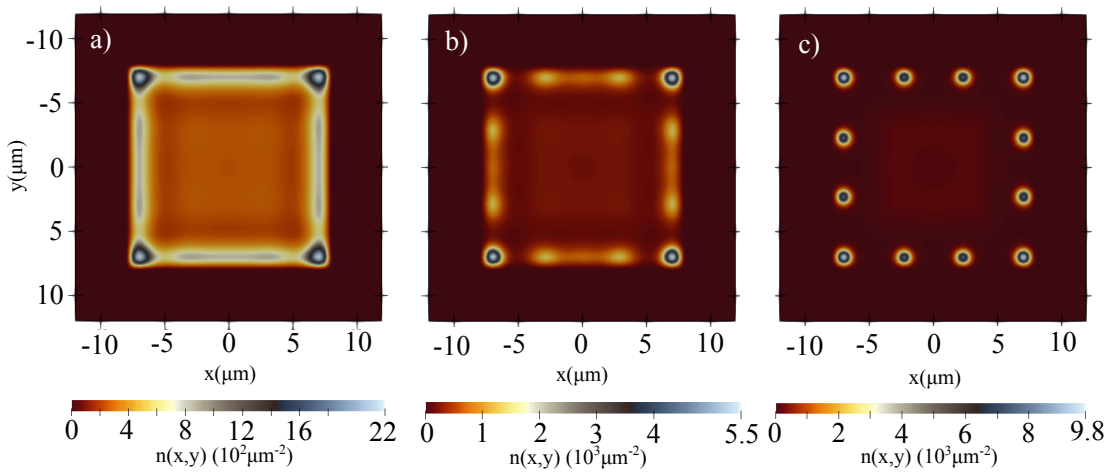


Figure 6.2: Ground state integrated density profiles $n(x,y) = \int dz |\Psi(x,y,z)|^2$ for a gas of $10^5$ atoms of $^{164}$Dy confined in the polarization direction by a harmonic potential of frequency $\omega_z = 2\pi(100)Hz$, and by a box potential in the x-y plane, with the shape of a square of side $L = 16\mu m$. The value of $\varepsilon_{dd}$ for panels a), b) and c) is, respectively, 1.32, 1.404 and 1.467. The height of the box is fixed to $V_0 = 100\omega_z$.

We first consider the more common case of a square box. This case was considered in [109] in the mean-field stable superfluid phase, in absence of beyond-mean-field effects. Here, we instead consider also regimes where the mean field approach would yield instability and the Lee-Huang-Yang correction allows for the emergence of the supersolid and independent droplet phases. More specifically, we determine, solving equation 2.23, the ground-state density profiles of $N = 100000$ atoms of $^{164}$Dy confined in a trapping potential of the form

$$V_{ext} = \frac{1}{2}m(\omega_z^2 z^2) + V_{box}(x, y, L) \tag{6.2}$$

with $\omega_z = 2\pi(100)Hz$, $V_{box}(x, y, L) = V_0$ for $|x|, |y| \geq L$ and 0 otherwise, $V_0 = 100\omega_z$ and $L = 16\mu m$. Typical density profiles for different values of $\varepsilon_{dd}$ are reported in figure 6.2, and reveal the same mechanism of accumulation of density near the boundary already discussed for the quasi-one-dimensional case. In particular, the vertices of the square box become points of strong accumulation of dipoles, causing density modulations along the sides of the square, even for small values of $\varepsilon_{dd}$ (see figure 6.2 panel a), when the system is in the superfluid phase. The behavior of the density along each edge of the square configuration shares interesting analogies with the behavior exhibited by a quasi one-dimensional gas confined by a box potential studied in the previous section. However, as we have seen, the presence of rotonic oscillations caused by the presence of vertices makes the identification of the superfluid-supersolid phase transition a rather involved task. For these reason, in order to avoid the accumulation effect caused by the presence of vertices, we now consider a box potential with a *circular* shape, obtained by confining the atoms in an external potential of the form

$$V_{ext} = \frac{1}{2}m(\omega_z^2 z^2) + V_{circ}(x, y, L) \tag{6.3}$$

with $\omega_z = 2\pi(100)Hz$, $V_{box}(x, y, L) = V_0$ for $\sqrt{x^2 + y^2} \geq R$ and 0 otherwise, $V_0 = 100\omega_z$ and $R = 10.185\mu m$. Similar configurations have been already experimentally realized to trap alkali atoms [104, 105, 106]. Once again, as shown in figure 6.3, most of the atoms accumulate at the edge of the confining potential, forming a quasi-one-dimensional ring structure well separated from the atoms in the bulk. For small values of $\varepsilon_{dd}$ both the edge and the bulk remain in a uniform superfluid phase (figure 6.3 panel a), while increasing $\varepsilon_{dd}$ (i.e. increasing the effect of the dipolar force), the edge region undergoes a phase transition to the supersolid phase (figure 6.3 panel b), where the density peaks near the boundary of the box exhibit a finite overlap, ensuring global phase coherence. The overlap between the density peaks disappears for even larger values of $\varepsilon_{dd}$, the system forming a sort of one dimensional ring crystal (figure 6.3 panel c).

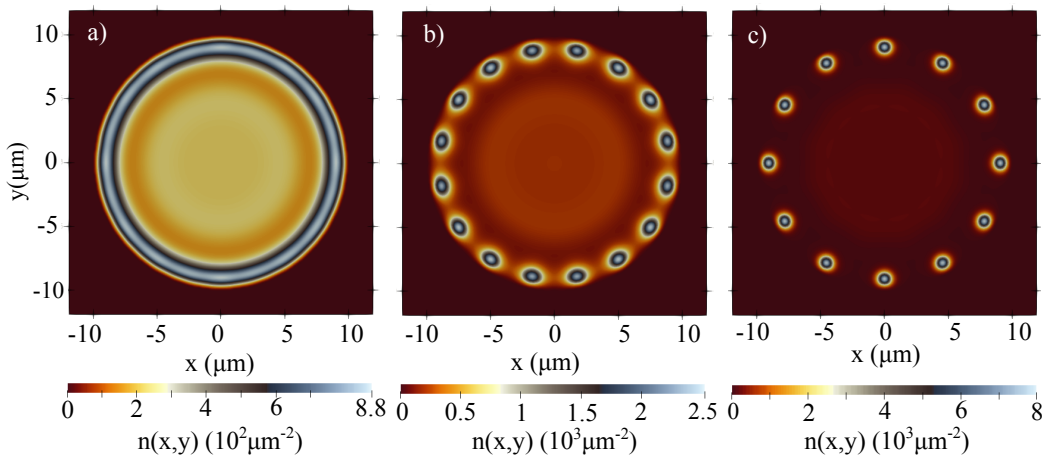


Figure 6.3: Ground state integrated density profiles $n(x,y) = \int dz |\Psi(x,y,z)|^2$ for a gas of $10^5$ atoms of $^{164}$Dy confined in the polarization direction by a harmonic potential of frequency $\omega_z = 2\pi(100)Hz$, and by a box potential in the x-y plane, with the shape of a circle of radius $R = 10.185\mu m$. The value of $\varepsilon_{dd}$ for panels a), b) and c) is, respectively, 1.32, 1.404 and 1.467. The height of the box is fixed to $V_0 = 100\omega_z$.

The emergent edge ring geometry allows to estimate the superfluid density along the edge in terms of the Leggett variational expression [14, 15, 24]. To this purpose we write the ground-state density in cylindrical coordinates $\rho(r,\theta,z)$, so that the Leggett's estimate for the superfluid density can be written as

$$\frac{n_S}{n} = \frac{2\pi}{n}\left(\int \frac{d\theta}{\int dr dz \rho(r,\theta,z)}\right)^{-1} \tag{6.4}$$

where the integration over the radial coordinate is performed only in the edge region, identified by the density minima that appears both at the border of the box (where the density goes to zero), and at the interface between the edge and the bulk. As already discussed in Chapter 3, the estimate 6.4 for the superfluid density coincides with the result obtained by letting the walls of the container to rotate slowly around the z-axis.

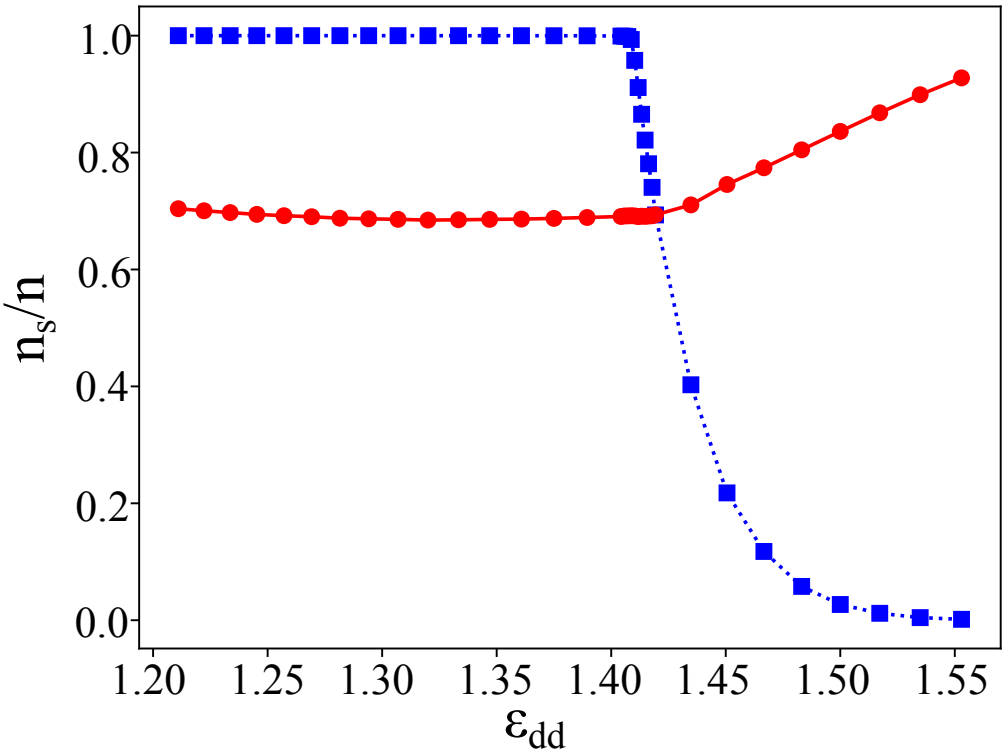


Figure 6.4: Estimate of the superfluid fraction of the edge region as function of $\varepsilon_{dd}$, based on Leggett's variational formula 6.4 (blue squares), applied to the configuration described in figure 6.3. Red circles represent the ratio between the number of atoms that settle on the edge and the total number of atoms in the system.

The estimate 6.4, reported in figure 6.4 (blue squares), reveals a critical dependence on $\varepsilon_{dd}$, emphasizing the emergence of a phase transition between the superfluid and the supersolid phase at $\varepsilon_{dd} = 1.4$ and a transition between the supersolid and the crystal phase, characterized by the vanishing of $n_S$, at $\varepsilon_{dd} = 1.55$. These values are very close to the critical values calculated for one dimensional tubular configurations imposing periodic boundary conditions [65], after taking into account that in the edge configuration discussed here the number of atoms occupying the ring increases with $\varepsilon_{dd}$, as shown in the same figure (red circles). Such an increase is actually particularly important in the supersolid phase as a consequence of the reduced value of the chemical potential, which favors the accumulation of dipoles on the density peaks, where the inter-atomic dipolar interaction is mainly attractive. The novel configuration emerging in the box of circular shape

discussed above is particularly attractive because in this case the boundary does not depend on the azimuthal coordinate and takes the form of a ring, where the dipolar particles form a one-dimensional structure, well separated from the atoms in the bulk. This provides the interesting possibility of exploring superfluid and supersolid features in uniform one dimensional like configurations with periodic boundary conditions, without the need of actually implementing a ring trap.

## 6.3 Bulk supersolidity

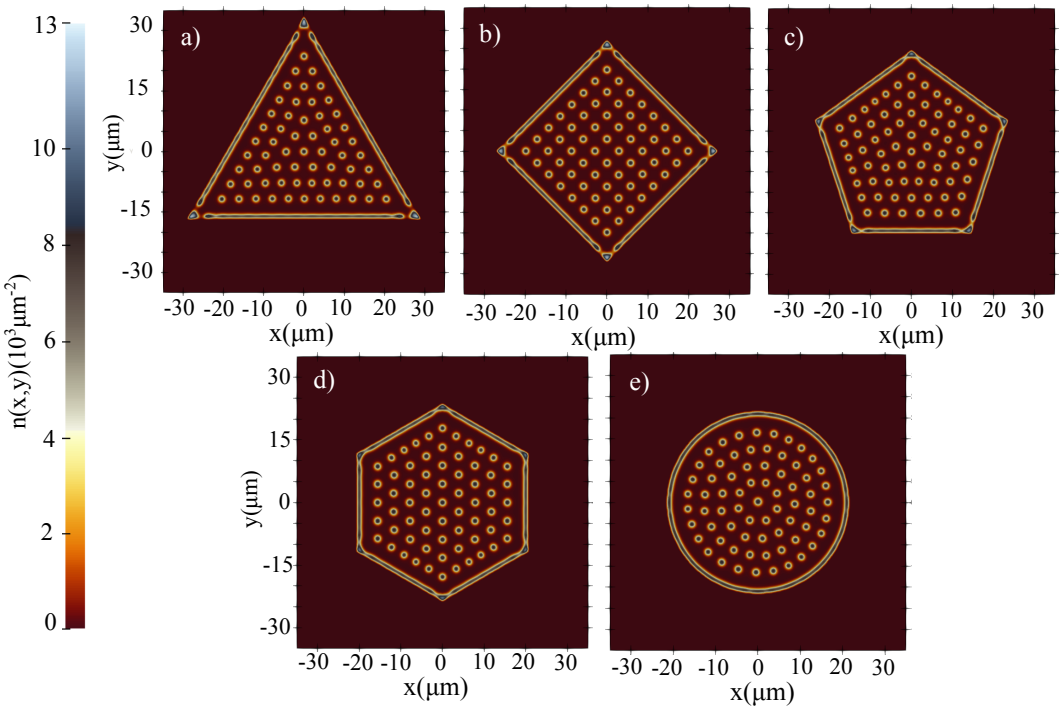


Figure 6.5: Integrated density profiles $n(x,y) = \int dz |\Psi(x,y,z)|^2$ for a gas of $2\times10^6$ atoms of $^{164}$Dy confined in the polarization direction by a harmonic potential of frequency $\omega_z = 2\pi(100)Hz$, and by a box potential in the x-y plane, with the shape of a triangle of side $L = 58.58\mu m$ (panel a), a square of side $L = 45.84\mu m$ (panel b), a pentagon of side $L = 38.33\mu m$ (panel c), an hexagon of side $L = 33.82\mu m$ (panel d), and a circle of radius $R = 21.75\mu m$ (panel e). The value of $\varepsilon_{dd} = 1.36$ is the same for all the configurations, which also have the same area.

The configurations discussed so far do not reveal the emergence of supersolid effects in the bulk region, because of the small value of the bulk density caused

by the accumulation of dipoles near the boundary. In order to observe the bulk supersolidity one consequently needs to increase significantly the atom density, in such a way that the density in the central region remains large enough to ensure the appearance of a crystal quantum phase. In figure 6.5, we have considered configurations containing $N = 2 \times 10^6$ atoms of $^{164}$Dy confined by a box potential in the transverse direction, with the shape of regular polygons (panels a-d) or circular (panel e), all with the same area (and hence the same number of atoms per unit surface). For the same value of $\varepsilon_{dd} = 1.36$, these configurations exhibit a supersolid structure in the bulk, characterized by the typical overlap between neighbouring density peaks, well separated from the edge region by a density dip. Despite the number of atoms and system size considered, resulting in a large number of droplets ($\simeq 60$), the symmetry of the supersolid lattice reflects the one of the confining potential, implying that surface effects hinder the possibility of reaching the thermodynamic limit, where the lattice is expected to be triangular or honeycomb [110]. This can be qualitatively understood as a consequence of the long-range nature of the dipolar force and the formation of the edge. In fact, since the dipoles are in a mainly repulsive configuration, they tend to expand towards the edge, where they acquire a density profile with the same shape of the confining potential; the droplets that form in the bulk also tend to repel each other, but their expansion is stopped by the repulsion of the edge, so that they are forced to arrange in lines parallel to the sides of the edge. This behavior is suppressed in an infinite system or in a harmonic trap, where the expansion of the gas is energetically unfavorable. It is worth noticing that the supersolid and crystal structures at the edge of the boundary, which are well visible in the configurations of figures 6.3 and 6.2, have disappeared in figure 6.5 as a consequence of the high density acquired by the system near the boundary, caused by the large value of N. As pointed out in [66], the density dependence of the critical value of the interaction parameter $\varepsilon_{dd}$, which separates the superfluid from the supersolid phase, actually exhibits a characteristic non monotonic dependence, as discussed in this thesis in Chapter 3 and as shown in figure 3.2 panel (b). This implies that, for a properly fixed value of $\varepsilon_{dd}$, if one increases the density starting from small values, the system undergoes first a phase transition from the superfluid to the supersolid (and eventually to the independent droplet) phase characterized by typical density oscillations, to come back again to the uniform superfluid phase at larger densities. Notice that this effect can also be observed with a smaller number of atoms, by confining them in properly designed box potentials of smaller dimension. In fact, such density, although relatively high ($\simeq 10^{15} cm^{-3}$ for the edge configurations shown in figure 6.5), is still compatible with the usual stability conditions imposed by three-body recombination, suggesting the possibility of observing this effect in actual experiments. We have finally checked that the results presented

in this chapter do not qualitatively change for different choices of the parameters. In particular we have considered different values of the transverse confinement in the interval $2\pi(50)Hz < \omega_{y,z} < 2\pi(150)Hz$, as well as different system sizes and number of atoms. The actual choice of $\omega_{y,z}$ can however affect the value of the density in the central region, the critical value of $\varepsilon_{dd}$ for the superfluid-supersolid phase transition, as well as the number of droplets which form in the supersolid phase, their relative distance being sensitive to the value of $\omega_z$ [61].

# Conclusions

In this thesis, we have studied theoretically some relevant properties of Bose-Einstein condensates of magnetic atoms, pointing out novel features occurring both in the ground-state and in the dynamics of these systems. Some of our results have already been confirmed by recent experiments.
We have first considered the case of a dipolar Bose gas confined in a ring geometry, obtained numerically by confining the system in a transverse harmonic confinement with periodic boundary conditions along the unconfined direction. The excitation spectrum and the ground-state density profiles are deeply affected by the interaction parameters, that can be tuned in current experiments. When the strength of the contact repulsion is comparable with that of the (partially attractive) dipolar interaction, the ground state of the system is a uniform superfluid, whose excitation spectrum is characterized by the occurrence of a roton minimum. The softening of the roton mode, that can be obtained by reducing the strength of the contact repulsion, thus increasing the relative weight of the dipolar interaction, triggers a phase transition towards a *supersolid* state which, while keeping superfluid properties, spontaneously breaks the symmetry for continuous spatial translations in favour of a discrete one, showing thus a periodic modulation in its density profile. This state shows, paradoxically, properties of both solids and superfluids. We have demonstrated that this system shows the two fundamental hallmarks of supersolidity, namely a non-classical rotational inertia due to a finite superfluid fraction, and an additional Goldstone mode in its excitation spectrum. We have also studied the linear response of the system to density perturbations, studying the contribution of the various excitation modes of the system to observable quantities such as the static and the dynamic structure factor.
We have then considered the case of a dipolar BEC confined in a cigar-shaped harmonic trap, with the main axis orthogonal to the polarization direction, focusing of configurations relevant for current experiments. We have shown that also this trapping configuration allows to study the superfluid-supersolid phase transition, and that the two hallmarks of supersolid behavior manifests in the harmonically trapped system in the behavior of its collective oscillations. In particular, we have shown that non-classical inertia can be studied via the frequency of the scissors

mode, while the presence of the two Goldstone modes manifests in a bifurcation of the compressional oscillations of the system.
We have then considered another fundamental manifestation of superfluidity in a dipolar supersolid, namely the possibility for the system to host quantized vortices. We have shown a trapped dipolar supersolid in an in-plane isotropic harmonic trap, can host vortex lines in the interstitial regions between the density peaks of the supersolid. The size and the shape of the vortex core is completely determined by the presence of the surrounding density peaks, and the angular momentum carried by the vortex line is affected by the only partial superfluid character of the system. Moreover, we have shown that vortex lattices are characterized by a pinning of the vortex position at the density dips of the supersolid, and that all these features are readily observable in expansion experiments.
Finally, we have considered the behavior of a dipolar Bose gas in a box potential. While in the case of an ordinary (non-dipolar) BEC, such trapping configuration allows the realization of a uniform system, and thus paves the way to the study of the properties of these systems in the thermodynamic limit, in the case of a dipolar gas, we show that the long range and anisotropic nature of the dipolar force produce a strong depletion of atoms from the center of the trap. The atomic dipoles tend to accumulate near the borders of the box potential, allowing the realization of peculiar edge supersolid configurations. For a very high number of atoms, we show that also the system bulk can show supersolidity, but the resulting geometry reflects the one of the boundary instead of assuming the shape expected in the thermodynamic limit.

# Appendix A

# Details on the calculation of the Lee-Huang-Yang correction

Here, we give a brief overview on how the Lee-Huang-Yang first order beyond mean field correction to the ground state energy can be calculated for a homogeneous system of magnetic bosonic atoms in the Bose-Condensed phase.
Consider the general case of a weakly interacting Bose gas of atoms interacting via a general pseudo-potential $V(\mathbf{r})$, whose Fourier transform is $V_{\mathbf{k}}$. In the case of a uniform system ($V_{ext} = 0$), a good quantum number is the wave number $\mathbf{k}$, and the field operators $\hat{\Psi}$ and $\hat{\Psi}^\dagger$ can be expanded as

$$\begin{aligned}\hat{\Psi}(\mathbf{r}) &= \sum_{\mathbf{k}} \hat{a}_{\mathbf{k}} \mathrm{e}^{-i\mathbf{k}\cdot\mathbf{r}} \\ \hat{\Psi}^\dagger(\mathbf{r}) &= \sum_{\mathbf{k}} \hat{a}^\dagger_{\mathbf{k}} \mathrm{e}^{i\mathbf{k}\cdot\mathbf{r}}\end{aligned} \tag{A.1}$$

where $\hat{a}^\dagger_{\mathbf{k}}$ and $\hat{a}_{\mathbf{k}}$ are respectively a creation and a destruction operators for an excitation with momentum $\hbar\mathbf{k}$. Inserting this expansion in the hamiltonian 2.4, one obtains

$$\hat{H} = \sum_{\mathbf{k}} \frac{\hbar^2 k^2}{2m} \hat{a}^\dagger_{\mathbf{k}} \hat{a}_{\mathbf{k}} + \frac{1}{2V} \sum_{\mathbf{k},\mathbf{p},\mathbf{q}} V_{\mathbf{q}} \hat{a}^\dagger_{\mathbf{k}+\mathbf{q}} \hat{a}^\dagger_{\mathbf{p}-\mathbf{q}} \hat{a}_{\mathbf{p}} \hat{a}_{\mathbf{k}} \tag{A.2}$$

where $V$ is the total volume occupied by the gas. In order to calculate the ground state energy of the system, following for example [2, 116], we introduce the Bogolyubov approximation and substitute the ground state (zero momentum) cre-

ation and destruction operators by *c-numbers*, according to

$$\hat{a}_0 \to \sqrt{N_0} \tag{A.3}$$

$$\hat{a}_0^\dagger \to \sqrt{N_0} \tag{A.4}$$

where $N_0$ is the number of particles in the condensate, supposed to be much larger then one. Then, we separate, in the Hamiltonian A.2, the various terms that contains powers of $N_0$ and keep only terms which are, at least, linear in $N_0$, obtaining

$$\hat{H} = \sum_{\mathbf{k}} \left( \frac{\hbar^2 k^2}{2m} + \frac{N_0(V_0 + V_{\mathbf{k}})}{V} \right) \hat{a}_{\mathbf{k}}^\dagger \hat{a}_{\mathbf{k}} + \frac{1}{2} N_0^2 V_0 + \frac{N_0}{2V} {\sum_{\mathbf{k}}}' V_{\mathbf{k}} (\hat{a}_{\mathbf{k}}^\dagger \hat{a}_{-\mathbf{k}}^\dagger + \hat{a}_{\mathbf{k}} \hat{a}_{-\mathbf{k}}) \tag{A.5}$$

where the prime symbol means that the term with $\mathbf{k} = 0$ is excluded from the sum. Writing the total number of atoms as

$$N = N_0 + {\sum_{\mathbf{k}}}' \hat{a}_{\mathbf{k}}^\dagger \hat{a}_{\mathbf{k}} \tag{A.6}$$

and introducing the Bogolyubov transformation

$$\hat{a}_{\mathbf{k}} = u_{\mathbf{k}} \hat{\alpha}_{\mathbf{k}} - v_{\mathbf{k}} \hat{\alpha}_{-\mathbf{k}}^\dagger \tag{A.7}$$

one obtains a diagonal Hamiltonian if the functions $u_{\mathbf{k}}$ and $v_{\mathbf{k}}$ are given by

$$u_{\mathbf{k}}, v_{\mathbf{k}} = \frac{1}{2} \left[ \frac{\frac{\hbar^2 k^2}{2m} + \frac{N V_{\mathbf{k}}}{V}}{\epsilon_{\mathbf{k}}} \pm 1 \right] \tag{A.8}$$

where

$$\epsilon_{\mathbf{k}} = \sqrt{\frac{\hbar^2 k^2}{2m} \left[ \frac{\hbar^2 k^2}{2m} + 2 n V_{\mathbf{k}} \right]} \tag{A.9}$$

is the spectrum of the elementary excitations of the system, and $n = N/V$ is the density. Requiring the operators $\hat{\alpha}_{\mathbf{k}}$ and $\hat{\alpha}_{\mathbf{k}}^\dagger$ to satisfy bosonic commutation relations impose the following normalization condition on $u_{\mathbf{k}}$ and $v_{\mathbf{k}}$

$$|u_{\mathbf{k}}|^2 - |v_{\mathbf{k}}|^2 = 1 \tag{A.10}$$

The final diagonal hamiltonian is then given by

$$\hat{H} = \frac{1}{2V} N^2 V_0 + \frac{1}{2} {\sum_{\mathbf{k}}}' \left( E_{\mathbf{k}} - \frac{\hbar^2 k^2}{2m} - \frac{N V_{\mathbf{k}}}{V} \right) + {\sum_{\mathbf{k}}}' E_{\mathbf{k}} \hat{\alpha}_{\mathbf{k}}^\dagger \hat{\alpha}_{\mathbf{k}} \tag{A.11}$$

The ground state energy of the system can then be calculated from A.11 neglecting the last term, which account for the energy contribution coming from the elementary excitations. Thus, we find

$$\frac{E_0}{V} = \frac{1}{2V}N^2 V_0 + \frac{1}{2}{\sum_{\mathbf{k}}}' \left( \epsilon_{\mathbf{k}} - \frac{\hbar^2 k^2}{2m} - \frac{N V_{\mathbf{k}}}{V} \right) \tag{A.12}$$

The first term of this expression correspond to the mean-field ground-state energy of the system, so that the second term accounts for the first order beyond mean field correction. To give an estimate of this correction, it is now necessary to consider a definite model for the inter-atomic interaction potential $V(\mathbf{r})$. Using, for example, the contact pseudo-potential 2.5, we obtain

$$\frac{E_0}{V} = \frac{1}{2}gn^2 + \frac{1}{2}{\sum_{\mathbf{k}}}' \left( \epsilon_{\mathbf{k}} - \frac{\hbar^2 k^2}{2m} - gn \right) \tag{A.13}$$

where now

$$\epsilon_{\mathbf{k}} = \sqrt{\frac{\hbar^2 k^2}{2m}\left[\frac{\hbar^2 k^2}{2m} + 2gn\right]} \tag{A.14}$$

The second term in A.13 is ultraviolet divergent, and needs to be regularized. The typical procedure is to consider the expression of the scattering length beyond the first Born approximation, which reads [2, 116]

$$\frac{4\pi a \hbar^2}{m} = V_0 - \frac{m}{\hbar^2}\int \frac{d\mathbf{q}}{(2\pi)^3}\frac{V(\mathbf{q})V(-\mathbf{q})}{q^2} \tag{A.15}$$

Plugging this into A.13 one finally finds the famous Lee-Huang-Yang (LHY) expression for the ground state energy of a system of weakly interacting, hard-sphere bosons [117]

$$\frac{E_0}{V} = \frac{1}{2}gn^2\left[1 + \frac{128}{15\sqrt{\pi}}\sqrt{na^3}\right] \tag{A.16}$$

The same procedure has been applied in [43, 44] to a homogeneous dipolar Bose gas, in which atoms interact via the pseudo-potential 2.6. Using the Fourier transform of the dipole-dipole interaction potential 2.2, given by [35]

$$V_{dd}(\mathbf{k}) = \frac{C_{dd}}{3}(3\cos^2\alpha - 1) \tag{A.17}$$

where $\alpha$ is the angle between $\mathbf{k}$ and the polarization direction, one finds that the Bogolyubov spectrum of the elementary excitations is given by

$$\epsilon_{\mathbf{k}} = \sqrt{\frac{\hbar^2 k^2}{2m}\left\{\frac{\hbar^2 k^2}{2m} + 2gn[1 + \epsilon_{dd}(3\cos^2\alpha - 1)]\right\}} \tag{A.18}$$

where $\epsilon_{dd} = a_{dd}/a$ is a parameter measuring the relative strength of the contact and dipole-dipole interaction. The dependency of the excitation energy A.18 on the angle $\alpha$ implies that, for $\epsilon_{dd} > 1$, phononic excitations ($\mathbf{k} \to 0$) may acquire imaginary frequencies, in particular when travelling orthogonally to the polarization direction ($\alpha = \pi/2$). A three-dimensional homogeneous dipolar BEC is thus unstable for $\epsilon_{dd} > 1$. Moreover, the first-order beyond mean-filed result for the ground state energy becomes

$$\frac{E_0}{V} = \frac{1}{2} g n^2 \left[ 1 + \frac{128}{15\sqrt{\pi}} \sqrt{n a^3} F(\epsilon_{dd}) \right] \tag{A.19}$$

where

$$F(\epsilon_{dd}) = \frac{1}{2} \int_0^\pi d\theta \sin\theta [1 + \epsilon_{dd}(3\cos^2\theta - 1)]^{\frac{5}{2}} \tag{A.20}$$

The function $F(\epsilon_{dd})$ is real and positive for $0 < \epsilon_{dd} < 1$, and in particular increases monotonically from 1 to $\simeq 2.6$. For $\epsilon_{dd} > 1$, this correction acquires a small imaginary part, indicating the presence of an energetic instability in the system. Notice also that, for $\epsilon_{dd} = 0$, expression 2.19 reduces exactly to A.16.

# Appendix B

# Fourier transform of the dipolar potential

A very useful result we used thoroughly in the numerical simulations in this thesis is that the Fourier transform of the dipole-dipole interaction 2.2 reads

$$\tilde{V_k} = \epsilon_{dd}(3cos^2\alpha - 1) \tag{B.1}$$

where $\alpha$ is the angle between the vector $\mathbf{k}$ and the z-axis. Here, we sketch the calculation that leads to this result.
Consider the form of the dipole-dipole potential

$$V_{dd}(\mathbf{r}) = \frac{C_{dd}}{4\pi}\frac{1 - 3cos^2\theta}{r^3} \tag{B.2}$$

where $\theta$ is the angle between $\mathbf{r}$ and the z-axis. Let us define the Fourier transform as

$$\tilde{V}_{dd}(\mathbf{k}) = \int d\mathbf{r} V_{dd}(\mathbf{r}) e^{-i\mathbf{k}\cdot\mathbf{r}} \tag{B.3}$$

and use spherical coordinates, with the z-axis axis along $\mathbf{k}$, the dipole moment $\mathbf{d}$ in the $y = 0$ plane, and let $\alpha$ be the angle between $\mathbf{k}$ and the polarization direction We clearly have

$$\mathbf{d} = d(\sin\alpha, \cos\alpha) \tag{B.4}$$

so that

$$\begin{aligned}\tilde{V}_{dd}(\mathbf{k}) = &\int d\mathbf{r} V_{dd}(\mathbf{r}) e^{-i\mathbf{k}\cdot\mathbf{r}} \\ &\int_0^{2\pi} d\phi \int_0^{\pi} d\theta \sin\theta \int_b^{\infty} dr r^2 \frac{C_{dd}}{4\pi}\frac{1 - cos^2\beta}{r^3} e^{-ikrcos\theta}\end{aligned} \tag{B.5}$$

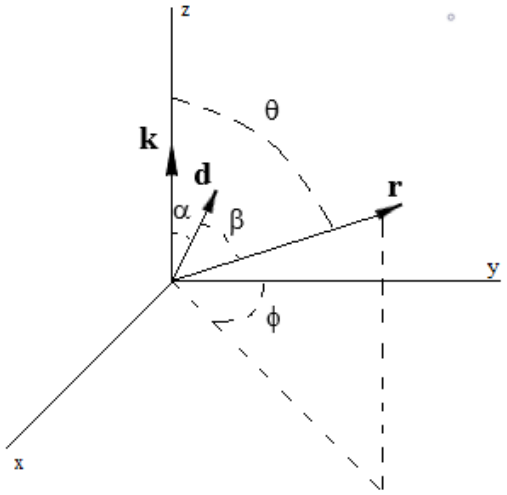


where $b$ is a small radius cut-off, introduced temporarily to avoid any divergence. We can also write

$$\cos\beta = \frac{\mathbf{d}\cdot\mathbf{r}}{dr} = \frac{x\sin\alpha + z\cos\alpha}{r} = \sin\theta\cos\phi\sin\alpha + \cos\alpha\cos\theta \tag{B.6}$$

so that the integral over the angle $\phi$ gives

$$\int_0^{2\pi} d\phi \left[1 - 3(\sin\theta\cos\phi\sin\alpha + \cos\alpha\cos\theta)^2\right] = 2\pi - 3\pi\sin^2\theta\sin^2\alpha - 6\pi\cos^2\alpha\cos^2\theta \tag{B.7}$$

We plug this expression into B.5 and integrate over $\theta$. Fixing $x = \cos\theta$ and $u = kr$ we obtain

$$\begin{aligned}
&\int_0^{\pi} d\theta \sin\theta e^{-ikr\cos\theta}\left[2\pi - 3\pi\sin^2\theta\sin^2\alpha - 6\pi\cos^2\alpha\cos^2\theta\right] = \\
&\int_{-1}^{1} dx e^{-iux}[2\pi - 3\pi(1-x^2)\sin^2\alpha - 6\pi\cos^2\alpha x^2] \\
&\pi(3\cos^2\alpha - 1)\int_{-1}^{1} dx e^{-iux}(1-3x^2) \\
&4\pi(1-3\cos^2\theta)\left[\frac{\sin u}{u} + 3\frac{\cos u}{u^2} - 3\frac{\sin u}{u^3}\right]
\end{aligned} \tag{B.8}$$

Final integration over $u = kr$ then gives

$$\tilde{V}_{dd}(\mathbf{k}) = C_{dd}(1 - 3\cos^2\alpha)\left[\frac{\cos(kb)}{(kb)^2} - \frac{sin(kb)}{(kb)^3}\right] \tag{B.9}$$

and taking the final limit $kb \to 0$ we obtain

$$\tilde{V}_{dd}(\mathbf{k}) = \frac{C_{dd}}{3}(3\cos^2\alpha - 1) \tag{B.10}$$

# List of publications


[1] Santo Maria Roccuzzo and Francesco Ancilotto. Supersolid behavior of a dipolar bose-einstein condensate confined in a tube. *Phys. Rev. A*, 99:041601, Apr 2019.

[2] L. Tanzi, S. M. Roccuzzo, E. Lucioni, F. Famà, A. Fioretti, C. Gabbanini, G. Modugno, A. Recati, and S. Stringari. Supersolid symmetry breaking from compressional oscillations in a dipolar quantum gas. *Nature*, 574(7778):382–385, Oct 2019.

[3] S. M. Roccuzzo, A. Gallemí, A. Recati, and S. Stringari. Rotating a supersolid dipolar gas. *Phys. Rev. Lett.*, 124:045702, Jan 2020.

[4] A. Gallemí, S. M. Roccuzzo, S. Stringari, and A. Recati. Quantized vortices in dipolar supersolid bose-einstein-condensed gases. *Phys. Rev. A*, 102:023322, Aug 2020.

[5] D. Petter, A. Patscheider, G. Natale, M. J. Mark, M. A. Baranov, R. van Bijnen, S. M. Roccuzzo, A. Recati, B. Blakie, D. Baillie, L. Chomaz, and F. Ferlaino. Bragg scattering of an ultracold dipolar gas across the phase transition from bose-einstein condensate to supersolid in the free-particle regime. *Phys. Rev. A*, 104:L011302, Jul 2021.

[6] S. M. Roccuzzo, S. Stringari, and Alessio Recati. Supersolid edge and bulk phases of a dipolar quantum gas in a box. 2021.

# Bibliography


[1] Kerson Huang and C. N. Yang. Quantum-mechanical many-body problem with hard-sphere interaction. *Phys. Rev.*, 105:767–775, Feb 1957.

[2] Lev Pitaevskii and Sandro Stringari. *Bose-Einstein condensation and superfluidity*. Oxford University Press, 2016.

[3] Axel Griesmaier, Jörg Werner, Sven Hensler, Jürgen Stuhler, and Tilman Pfau. Bose-einstein condensation of chromium. *Phys. Rev. Lett.*, 94:160401, Apr 2005.

[4] Mingwu Lu, Nathaniel Q. Burdick, Seo Ho Youn, and Benjamin L. Lev. Strongly dipolar bose-einstein condensate of dysprosium. *Phys. Rev. Lett.*, 107:190401, Oct 2011.

[5] K. Aikawa, A. Frisch, M. Mark, S. Baier, A. Rietzler, R. Grimm, and F. Ferlaino. Bose-einstein condensation of erbium. *Phys. Rev. Lett.*, 108:210401, May 2012.

[6] Holger Kadau, Matthias Schmitt, Matthias Wenzel, Clarissa Wink, Thomas Maier, Igor Ferrier-Barbut, and Tilman Pfau. Observing the rosensweig instability of a quantum ferrofluid. *Nature*, 530(7589):194–197, Feb 2016.

[7] F. Wächtler and L. Santos. Quantum filaments in dipolar bose-einstein condensates. *Phys. Rev. A*, 93:061603, Jun 2016.

[8] Massimo Boninsegni and Nikolay V. Prokof'ev. Colloquium: Supersolids: What and where are they? *Rev. Mod. Phys.*, 84:759–776, May 2012.

[9] Oliver Penrose and Lars Onsager. Bose-einstein condensation and liquid helium. *Phys. Rev.*, 104:576–584, Nov 1956.

[10] A. F. Andreev and I. M. Lifshitz. Quantum theory of defects in crytals. *Sov. Phys. JETP*, 29(6), 1969.

[11] Gustavo During, Christophe Josserand, Yves Pomeau, and Sergio Rica. Theory of real supersolids, 2011.

[12] G. Bonfait and B. Godfrin, H.and Castaing. Solid 4he : search for superfluidity. *J. Phys. France*, 50(15), 1989.

[13] D. S. Greywall. Search for superfluidity in solid $^4$He. *Phys. Rev. B*, 16:1291–1292, Aug 1977.

[14] A. J. Leggett. Can a solid be "superfluid"? *Phys. Rev. Lett.*, 25:1543–1546, Nov 1970.

[15] A. J. Leggett. On the superfluid fraction of an arbitrary many-body system at t=0. *Journal of Statistical Physics*, 93(3):927–941, Nov 1998.

[16] D. J. Bishop, M. A. Paalanen, and J. D. Reppy. Search for superfluidity in hcp $^4$He. *Phys. Rev. B*, 24:2844–2845, Sep 1981.

[17] M. H. W. Kim, E.and Chan. Probable observation of a supersolid helium phase. *Nature*, 427(6971):225–227, Jan 2004.

[18] E. Kim and M. H. W. Chan. Observation of superflow in solid helium. *Science*, 305(5692):1941–1944, 2004.

[19] E. Kim and M. H. W. Chan. Supersolid helium at high pressure. *Phys. Rev. Lett.*, 97:115302, Sep 2006.

[20] A. C. Clark, J. T. West, and M. H. W. Chan. Nonclassical rotational inertia in helium crystals. *Phys. Rev. Lett.*, 99:135302, Sep 2007.

[21] Duk Y. Kim and Moses H. W. Chan. Absence of supersolidity in solid helium in porous vycor glass. *Phys. Rev. Lett.*, 109:155301, Oct 2012.

[22] Yves Pomeau and Sergio Rica. Dynamics of a model of supersolid. *Phys. Rev. Lett.*, 72:2426–2429, Apr 1994.

[23] Christophe Josserand, Yves Pomeau, and Sergio Rica. Coexistence of ordinary elasticity and superfluidity in a model of a defect-free supersolid. *Phys. Rev. Lett.*, 98:195301, May 2007.

[24] N. Sepulveda, C. Josserand, and S. Rica. Nonclassical rotational inertia fraction in a one-dimensional model of a supersolid. *Phys. Rev. B*, 77:054513, Feb 2008.

[25] F. Cinti, P. Jain, M. Boninsegni, A. Micheli, P. Zoller, and G. Pupillo. Supersolid droplet crystal in a dipole-blockaded gas. *Phys. Rev. Lett.*, 105:135301, Sep 2010.

[26] N. Henkel, R. Nath, and T. Pohl. Three-dimensional roton excitations and supersolid formation in rydberg-excited bose-einstein condensates. *Phys. Rev. Lett.*, 104:195302, May 2010.

[27] T. Macrì, F. Maucher, F. Cinti, and T. Pohl. Elementary excitations of ultracold soft-core bosons across the superfluid-supersolid phase transition. *Phys. Rev. A*, 87:061602, Jun 2013.

[28] Francesco Ancilotto, Maurizio Rossi, and Flavio Toigo. Supersolid structure and excitation spectrum of soft-core bosons in three dimensions. *Phys. Rev. A*, 88:033618, Sep 2013.

[29] Jun-Ru Li, Jeongwon Lee, Wujie Huang, Sean Burchesky, Boris Shteynas, Furkan Top, Alan O. Jamison, and Wolfgang Ketterle. A stripe phase with supersolid properties in spin–orbit-coupled bose–einstein condensates. *Nature*, 543(7643):91–94, Mar 2017.

[30] Julian Leonard, Andrea Morales, Philip Zupancic, Tilman Esslinger, and Tobias Donner. Supersolid formation in a quantum gas breaking a continuous translational symmetry. *Nature*, 543(7643):87–90, Mar 2017.

[31] L. Tanzi, E. Lucioni, F. Famà, J. Catani, A. Fioretti, C. Gabbanini, R. N. Bisset, L. Santos, and G. Modugno. Observation of a dipolar quantum gas with metastable supersolid properties. *Phys. Rev. Lett.*, 122:130405, Apr 2019.

[32] Fabian Böttcher, Jan-Niklas Schmidt, Matthias Wenzel, Jens Hertkorn, Mingyang Guo, Tim Langen, and Tilman Pfau. Transient supersolid properties in an array of dipolar quantum droplets. *Phys. Rev. X*, 9:011051, Mar 2019.

[33] L. Chomaz, D. Petter, P. Ilzhöfer, G. Natale, A. Trautmann, C. Politi, G. Durastante, R. M. W. van Bijnen, A. Patscheider, M. Sohmen, M. J. Mark, and F. Ferlaino. Long-lived and transient supersolid behaviors in dipolar quantum gases. *Phys. Rev. X*, 9:021012, Apr 2019.

[34] John David Jackson. *Classical electrodynamics; 2nd ed.* Wiley, New York, NY, 1975.

[35] T Lahaye, C Menotti, L Santos, M Lewenstein, and T Pfau. The physics of dipolar bosonic quantum gases. *Reports on Progress in Physics*, 72(12):126401, 2009.

[36] Luigi De Marco, Giacomo Valtolina, Kyle Matsuda, William G. Tobias, Jacob P. Covey, and Jun Ye. A degenerate fermi gas of polar molecules. *Science*, 363(6429):853–856, 2019.

[37] Lev Davydovic Landau and Evgenij Lifsic. *Quantum mechanics: non-relativistic theory*. Butterworth-Heinemann, 2010.

[38] S. Yi and L. You. Trapped atomic condensates with anisotropic interactions. *Phys. Rev. A*, 61:041604, Mar 2000.

[39] T. Koch, T. Lahaye, J. Metz, B. Fröhlich, A. Griesmaier, and T. Pfau. Stabilization of a purely dipolar quantum gas against collapse. *Nature Physics*, 4(3):218–222, Mar 2008.

[40] T. Lahaye, J. Metz, B. Fröhlich, T. Koch, M. Meister, A. Griesmaier, T. Pfau, H. Saito, Y. Kawaguchi, and M. Ueda. *d*-wave collapse and explosion of a dipolar bose-einstein condensate. *Phys. Rev. Lett.*, 101:080401, Aug 2008.

[41] Igor Ferrier-Barbut, Holger Kadau, Matthias Schmitt, Matthias Wenzel, and Tilman Pfau. Observation of quantum droplets in a strongly dipolar bose gas. *Phys. Rev. Lett.*, 116:215301, May 2016.

[42] D. S. Petrov. Quantum mechanical stabilization of a collapsing bose-bose mixture. *Phys. Rev. Lett.*, 115:155302, Oct 2015.

[43] Aristeu R. P. Lima and Axel Pelster. Quantum fluctuations in dipolar bose gases. *Phys. Rev. A*, 84:041604, Oct 2011.

[44] A. R. P. Lima and A. Pelster. Beyond mean-field low-lying excitations of dipolar bose gases. *Phys. Rev. A*, 86:063609, Dec 2012.

[45] Hiroki Saito. Path-integral monte carlo study on a droplet of a dipolar boseeinstein condensate stabilized by quantum fluctuation. *Journal of the Physical Society of Japan*, 85(5):053001, 2016.

[46] Fabian Böttcher, Matthias Wenzel, Jan-Niklas Schmidt, Mingyang Guo, Tim Langen, Igor Ferrier-Barbut, Tilman Pfau, Raúl Bombín, Joan Sánchez-Baena, Jordi Boronat, and Ferran Mazzanti. Dilute dipolar quantum droplets beyond the extended gross-pitaevskii equation. *Phys. Rev. Research*, 1:033088, Nov 2019.

[47] Duncan H. J. O'Dell, Stefano Giovanazzi, and Claudia Eberlein. Exact hydrodynamics of a trapped dipolar bose-einstein condensate. *Phys. Rev. Lett.*, 92:250401, Jun 2004.

[48] J. Nocedal and J. S. Wright. *Numerical Optimization*. Springer, 2017.

[49] Boris Polyak. Some methods of speeding up the convergence of iteration methods. *Ussr Computational Mathematics and Mathematical Physics*, 4:1–17, 12 1964.

[50] H. Attouch, X. Goudou, and P. Redont. The heavy ball with friction method, i. the continuous dynamical system: gloabal exploration of the local minima of a real valued function by asymptotic analysis of a dissipative dynamical system. *Communications in Contemporary Mathematics*, 02(01):1–34, 2000.

[51] N. W. Ashcroft and N. D. Mermin. *Solid state physics*. Saunder College Publishing, 1976.

[52] J. W. Demmel. *Applied Numerical Linear Algebra*. Society for Industrial and Applied Mathematics, 1997.

[53] E. Anderson, Z. Bai, C. Bischof, S. Blackford, J. Demmel, J. Dongarra, J. Du Croz, A. Greenbaum, S. Hammarling, A. McKenney, and D. Sorensen. *LAPACK Users' Guide*. Society for Industrial and Applied Mathematics, Philadelphia, PA, third edition, 1999.

[54] S. Koonin and D.C. Meredith. *Computational Physics*. Westview Press, 1990.

[55] M. Frigo and S.G. Johnson. The design and implementation of fftw3. *Proceedings of the IEEE*, 93(2):216–231, 2005.

[56] cufft. `https://docs.nvidia.com/cuda/cufft/index.html`.

[57] L. Landau. Theory of the superfluidity of helium ii. *Phys. Rev.*, 60:356–358, Aug 1941.

[58] D. G. Henshaw and A. D. B. Woods. Modes of atomic motions in liquid helium by inelastic scattering of neutrons. *Phys. Rev.*, 121:1266–1274, Mar 1961.

[59] P. Nozieres. More about rotons in superfluid helium 4. *Journal of Low Temperature Physics*, 142(1):91–99, Jan 2006.

[60] P. Nozieres. Is the roton in superfluid 4he the ghost of a bragg spot? *Journal of Low Temperature Physics*, 137(1):45–67, Oct 2004.

[61] L. Santos, G. V. Shlyapnikov, and M. Lewenstein. Roton-maxon spectrum and stability of trapped dipolar bose-einstein condensates. *Phys. Rev. Lett.*, 90:250403, Jun 2003.

[62] D. H. J. O'Dell, S. Giovanazzi, and G. Kurizki. Rotons in gaseous bose-einstein condensates irradiated by a laser. *Phys. Rev. Lett.*, 90:110402, Mar 2003.

[63] R. Mottl, F. Brennecke, K. Baumann, R. Landig, T. Donner, and T. Esslinger. Roton-type mode softening in a quantum gas with cavity-mediated long-range interactions. *Science*, 336(6088):1570–1573, 2012.

[64] L. Chomaz, R. M. W. van Bijnen, D. Petter, G. Faraoni, S. Baier, J. H. Becher, M. J. Mark, F. Wächtler, L. Santos, and F. Ferlaino. Observation of roton mode population in a dipolar quantum gas. *Nature Physics*, 14(5):442–446, May 2018.

[65] Santo Maria Roccuzzo and Francesco Ancilotto. Supersolid behavior of a dipolar bose-einstein condensate confined in a tube. *Phys. Rev. A*, 99:041601, Apr 2019.

[66] P. B. Blakie, D. Baillie, L. Chomaz, and F. Ferlaino. Supersolidity in an elongated dipolar condensate. *Phys. Rev. Research*, 2:043318, Dec 2020.

[67] Yun Li, Giovanni I. Martone, Lev P. Pitaevskii, and Sandro Stringari. Superstripes and the excitation spectrum of a spin-orbit-coupled bose-einstein condensate. *Phys. Rev. Lett.*, 110:235302, Jun 2013.

[68] L. Chomaz. Probing the supersolid order via high-energy scattering: Analytical relations among the response, density modulation, and superfluid fraction. *Phys. Rev. A*, 102:023333, Aug 2020.

[69] D. Petter, A. Patscheider, G. Natale, M. J. Mark, M. A. Baranov, R. van Bijnen, S. M. Roccuzzo, A. Recati, B. Blakie, D. Baillie, L. Chomaz, and F. Ferlaino. Bragg scattering of an ultracold dipolar gas across the phase transition from bose-einstein condensate to supersolid in the free-particle regime. *Phys. Rev. A*, 104:L011302, Jul 2021.

[70] L. Tanzi, S. M. Roccuzzo, E. Lucioni, F. Famà, A. Fioretti, C. Gabbanini, G. Modugno, A. Recati, and S. Stringari. Supersolid symmetry breaking from compressional oscillations in a dipolar quantum gas. *Nature*, 574(7778):382–385, Oct 2019.

[71] S. Stringari. Collective excitations of a trapped bose-condensed gas. *Phys. Rev. Lett.*, 77:2360–2363, Sep 1996.

[72] M.-O. Mewes, M. R. Andrews, N. J. van Druten, D. M. Kurn, D. S. Durfee, C. G. Townsend, and W. Ketterle. Collective excitations of a bose-einstein condensate in a magnetic trap. *Phys. Rev. Lett.*, 77:988–991, Aug 1996.

[73] Chiara Menotti and Sandro Stringari. Collective oscillations of a one-dimensional trapped bose-einstein gas. *Phys. Rev. A*, 66:043610, Oct 2002.

[74] N. Matveeva, A. Recati, and S. Stringari. Dipolar drag in bilayer harmonically trapped gases. *Eur. Phys. J. D*, 65(1-2):219–222, 2011.

[75] S. M. Roccuzzo, A. Gallemí, A. Recati, and S. Stringari. Rotating a supersolid dipolar gas. *Phys. Rev. Lett.*, 124:045702, Jan 2020.

[76] N. Lo Iudice and F. Palumbo. New isovector collective modes in deformed nuclei. *Phys. Rev. Lett.*, 41:1532–1534, Nov 1978.

[77] E. Lipparini and S. Stringari. Isovector m1 rotational states in deformed nuclei. *Physics Letters B*, 130(3):139–143, 1983.

[78] D. Bohle, A. Richter, W. Steffen, A.E.L. Dieperink, N. Lo Iudice, F. Palumbo, and O. Scholten. New magnetic dipole excitation mode studied in the heavy deformed nucleus 156gd by inelastic electron scattering. *Physics Letters B*, 137(1):27–31, 1984.

[79] D. Guéry-Odelin and S. Stringari. Scissors mode and superfluidity of a trapped bose-einstein condensed gas. *Phys. Rev. Lett.*, 83:4452–4455, Nov 1999.

[80] O. M. Maragò, S. A. Hopkins, J. Arlt, E. Hodby, G. Hechenblaikner, and C. J. Foot. Observation of the scissors mode and evidence for superfluidity of a trapped bose-einstein condensed gas. *Phys. Rev. Lett.*, 84:2056–2059, Mar 2000.

[81] A. Recati, F. Zambelli, and S. Stringari. Overcritical rotation of a trapped bose-einstein condensate. *Phys. Rev. Lett.*, 86:377–380, Jan 2001.

[82] L. Tanzi, J. G. Maloberti, G. Biagioni, A. Fioretti, C. Gabbanini, and G. Modugno. Evidence of superfluidity in a dipolar supersolid from nonclassical rotational inertia. *Science*, 371(6534):1162–1165, 2021.

[83] Shai Ronen, Daniele C. E. Bortolotti, and John L. Bohn. Radial and angular rotons in trapped dipolar gases. *Phys. Rev. Lett.*, 98:030406, Jan 2007.

[84] M. Abad, M. Guilleumas, R. Mayol, M. Pi, and D. M. Jezek. Vortices in bose-einstein condensates with dominant dipolar interactions. *Phys. Rev. A*, 79:063622, Jun 2009.

[85] D. H. J. O'Dell and C. Eberlein. Vortex in a trapped bose-einstein condensate with dipole-dipole interactions. *Phys. Rev. A*, 75:013604, Jan 2007.

[86] Yongyong Cai, Yongjun Yuan, Matthias Rosenkranz, Han Pu, and Weizhu Bao. Vortex patterns and the critical rotational frequency in rotating dipolar bose-einstein condensates. *Phys. Rev. A*, 98:023610, Aug 2018.

[87] A. Gallemí, S. M. Roccuzzo, S. Stringari, and A. Recati. Quantized vortices in dipolar supersolid bose-einstein-condensed gases. *Phys. Rev. A*, 102:023322, Aug 2020.

[88] Subhasis Sinha and Yvan Castin. Dynamic instability of a rotating bose-einstein condensate. *Phys. Rev. Lett.*, 87:190402, Oct 2001.

[89] David L. Feder, Anatoly A. Svidzinsky, Alexander L. Fetter, and Charles W. Clark. Anomalous modes drive vortex dynamics in confined bose-einstein condensates. *Phys. Rev. Lett.*, 86:564–567, Jan 2001.

[90] Carlos Lobo, Alice Sinatra, and Yvan Castin. Vortex lattice formation in bose-einstein condensates. *Phys. Rev. Lett.*, 92:020403, Jan 2004.

[91] N. G. Parker and C. S. Adams. Emergence and decay of turbulence in stirred atomic bose-einstein condensates. *Phys. Rev. Lett.*, 95:145301, Sep 2005.

[92] K. W. Madison, F. Chevy, W. Wohlleben, and J. Dalibard. Vortex formation in a stirred bose-einstein condensate. *Phys. Rev. Lett.*, 84:806–809, Jan 2000.

[93] K. W. Madison, F. Chevy, V. Bretin, and J. Dalibard. Stationary states of a rotating bose-einstein condensate: Routes to vortex nucleation. *Phys. Rev. Lett.*, 86:4443–4446, May 2001.

[94] R. M. W. van Bijnen, D. H. J. O'Dell, N. G. Parker, and A. M. Martin. Dynamical instability of a rotating dipolar bose-einstein condensate. *Phys. Rev. Lett.*, 98:150401, Apr 2007.

[95] J. R. Abo-Shaeer, C. Raman, J. M. Vogels, and W. Ketterle. Observation of vortex lattices in bose-einstein condensates. *Science*, 292(5516):476–479, 2001.

[96] H. Pu, L. O. Baksmaty, S. Yi, and N. P. Bigelow. Structural phase transitions of vortex matter in an optical lattice. *Phys. Rev. Lett.*, 94:190401, May 2005.

[97] J. W. Reijnders and R. A. Duine. Pinning and collective modes of a vortex lattice in a bose-einstein condensate. *Phys. Rev. A*, 71:063607, Jun 2005.

[98] T. Sato, T. Ishiyama, and T. Nikuni. Vortex lattice structures of a bose-einstein condensate in a rotating triangular lattice potential. *Phys. Rev. A*, 76:053628, Nov 2007.

[99] Daniel S. Goldbaum and Erich J. Mueller. Commensurability and hysteretic evolution of vortex configurations in rotating optical lattices. *Phys. Rev. A*, 79:063625, Jun 2009.

[100] S. Tung, V. Schweikhard, and E. A. Cornell. Observation of vortex pinning in bose-einstein condensates. *Phys. Rev. Lett.*, 97:240402, Dec 2006.

[101] T. P. Meyrath, F. Schreck, J. L. Hanssen, C.-S. Chuu, and M. G. Raizen. Bose-einstein condensate in a box. *Phys. Rev. A*, 71:041604, Apr 2005.

[102] Alexander L. Gaunt, Tobias F. Schmidutz, Igor Gotlibovych, Robert P. Smith, and Zoran Hadzibabic. Bose-einstein condensation of atoms in a uniform potential. *Phys. Rev. Lett.*, 110:200406, May 2013.

[103] S. Gupta, K. W. Murch, K. L. Moore, T. P. Purdy, and D. M. Stamper-Kurn. Bose-einstein condensation in a circular waveguide. *Phys. Rev. Lett.*, 95:143201, Sep 2005.

[104] N. Navon, A. L. Gaunt, R. P. Smith, and Z. Hadzibabic. Critical dynamics of spontaneous symmetry breaking in a homogeneous bose gas. *Science*, 347(6218):167170, 2015.

[105] Lauriane Chomaz, Laura Corman, Tom Bienaime, Remi Desbuquois, Christof Weitenberg, Sylvain Nascimbene, Jerome Beugnon, and Jean Dalibard. Emergence of coherence via transverse condensation in a uniform quasi-two-dimensional bose gas. *Nature Communications*, 6(1):6162, Jan 2015.

[106] Nir Navon, Alexander L. Gaunt, Robert P. Smith, and Zoran Hadzibabic. Emergence of a turbulent cascade in a quantum gas. *Nature*, 539(7627):72–75, Nov 2016.

[107] J. L. Ville, T. Bienaimé, R. Saint-Jalm, L. Corman, M. Aidelsburger, L. Chomaz, K. Kleinlein, D. Perconte, S. Nascimbène, J. Dalibard, and J. Beugnon. Loading and compression of a single two-dimensional bose gas in an optical accordion. *Phys. Rev. A*, 95:013632, Jan 2017.

[108] J. L. Ville, R. Saint-Jalm, É. Le Cerf, M. Aidelsburger, S. Nascimbène, J. Dalibard, and J. Beugnon. Sound propagation in a uniform superfluid two-dimensional bose gas. *Phys. Rev. Lett.*, 121:145301, Oct 2018.

[109] H.-Y. Lu, H. Lu, J.-N. Zhang, R.-Z. Qiu, H. Pu, and S. Yi. Spatial density oscillations in trapped dipolar condensates. *Phys. Rev. A*, 82:023622, Aug 2010.

[110] Yong-Chang Zhang, Fabian Maucher, and Thomas Pohl. Supersolidity around a critical point in dipolar bose-einstein condensates. *Phys. Rev. Lett.*, 123:015301, Jul 2019.

[111] Tullio Regge. Free boundary of he ii and feynman wave functions. *Journal of Low Temperature Physics*, 9(1):123–133, Oct 1972.

[112] F. Dalfovo. Structure of vortices in helium at zero temperature. *Phys. Rev. B*, 46:5482–5488, Sep 1992.

[113] G. V. Chester, R. Metz, and L. Reatto. On the theory of quantized vortices. *Phys. Rev.*, 175:275–285, Nov 1968.

[114] J. Hertkorn, J.-N. Schmidt, M. Guo, F. Bottcher, K. S. H. Ng, S. D. Graham, P. Uerlings, T. Langen, M. Zwierlein, and T. Pfau. Pattern formation in quantum ferrofluids: From supersolids to superglasses. *Phys. Rev. Research*, 3:033125, Aug 2021.

[115] Yong-Chang Zhang, Thomas Pohl, and Fabian Maucher. Phases of supersolids in confined dipolar bose-einstein condensates. *Phys. Rev. A*, 104:013310, Jul 2021.

[116] Alexander L. Fetter and John Dirk Walecka. *Quantum theory of many-particle systems*. Dover Publications, 2003.

[117] T. D. Lee, Kerson Huang, and C. N. Yang. Eigenvalues and eigenfunctions of a bose system of hard spheres and its low-temperature properties. *Phys. Rev.*, 106:1135–1145, Jun 1957.